

Wheels of Fire IV. Star Formation and the Neutral Interstellar Medium in the Ring Galaxy AM0644-741

James L. Higdon^{1,3,4}, Sarah J. U. Higdon¹, and Richard J. Rand^{2,3}

ABSTRACT

We combine data from the Australia Telescope National Facility and the Swedish ESO Submillimeter Telescope to investigate the neutral interstellar medium (ISM) in AM0644-741, a large and robustly star-forming ring galaxy. The galaxy’s ISM is concentrated in the 42 kpc diameter starburst ring, but appears dominated by atomic gas, with a global molecular fraction (f_{mol}) of only 0.079 ± 0.005 . Apart from the starburst peak, the gas ring appears stable against the growth of gravitational instabilities ($Q_{\text{gas}} = 2 - 7$). Including the stellar component lowers Q overall, but not enough to make $Q < 1$ everywhere. The ring’s global star formation efficiency (SFE) appears somewhat elevated relative to early spirals, but varies around the ring by more than an order of magnitude, peaking where star formation is most intense. AM0644-741’s star formation law is peculiar: HI follows a Schmidt law while H_2 is uncorrelated with star formation rate density. Photodissociation models yield low volume densities in the ring, particularly in the starburst quadrant ($n \approx 2 \text{ cm}^{-3}$), implying a warm neutral medium dominated ISM. At the same time, the ring’s pressure and ambient far-ultraviolet radiation field lead to the expectation of a predominantly molecular ISM. We argue that the ring’s peculiar star formation law, n , SFE, and f_{mol} result from the ISM’s $\gtrsim 100$ Myr confinement time in the starburst ring, which amplifies the destructive effects of embedded massive stars and supernovae. As a result, the ring’s molecular ISM becomes dominated by small clouds where star formation is most intense, causing M_{H_2} to be underestimated by ^{12}CO line fluxes: in effect $X_{\text{CO}} \gg X_{\text{Gal}}$ despite the ring’s solar metallicity. The observed large HI component is primarily a low density photodissociation product, i.e., a tracer rather than a precursor of massive star formation. Such an “over-cooked” ISM may be a general characteristic of evolved starburst ring galaxies.

¹Department of Physics, Georgia Southern University, Statesboro, GA 30460-8031, USA

²Department of Physics and Astronomy, University of New Mexico, Albuquerque, NM 87131, USA

³Visiting astronomer, European Southern Observatory.

⁴Visiting astronomer, Cerro Tololo Inter-American Observatory.

Subject headings: galaxies: individual (AM0644-741) – galaxies: individual (Lindsay-Shapley Ring) – galaxies: interactions – galaxies: ISM – galaxies: starburst

1. Introduction

A large and growing body of evidence supports the key role played by gravitational interactions in the formation and evolution of galaxies. In the hierarchical structure formation framework, galaxies are assembled over cosmic time through multiple mergers (e.g., White & Rees 1978; Bell et al. 2006; Jogee et al. 2009). Evidence for this can be found in the observed asymmetric, sometimes chaotic morphologies of a significant fraction of galaxies detected in deep surveys (e.g., Williams et al. 1996; Ferguson et al. 2000; Conselice et al. 2003). Similarly, there are indications that submillimeter galaxies, thought to be the precursors of current epoch massive bulge dominated galaxies, experience star formation rates (SFR) in excess of $\approx 1000 M_{\odot} \text{ yr}^{-1}$ as a direct result of mergers (e.g., Smail et al. 1997; Richards et al. 1999; Tacconi et al. 2008). Morphological evolution is also clearly attributable to close passages and mergers (e.g., Toomre 1974; Dressler 1980; Moore et al. 1996; Hibbard et al. 2001). Interactions likewise appear involved with the funneling of material to the immediate vicinity of supermassive black holes and thus the switching on of active galactic nuclei (AGNs; e.g., Heckman et al. 1986; Ramos Almeida et al. 2011). Detailed numerical and observational studies of strongly interacting systems in the local universe are thus highly relevant, especially when the dynamical history of the encounter can be reasonably well reconstructed, allowing detailed numerical simulations capable of following the evolution of star-forming interstellar medium (ISM) that can be constrained by observations.

Ring galaxies are striking examples of the ability of collisions to transform both the morphology and star-forming activity of a spiral galaxy. Numerical studies since the mid-1970s argue persuasively that the optically prominent rings are in fact outwardly propagating zones of strong orbit crowding within the disk of a spiral induced by the near central passage of a companion galaxy (e.g., Lynds & Toomre 1976; Struck & Higdson 1993; Mapelli et al. 2008, but see Korchagin et al. 1999, 2001 for a very different formation mechanism). The expanding rings are transient but maintain their coherence for roughly one outer-disk rotation period (~ 300 Myr). $\text{H}\alpha$ emission line imaging show the rings to be nearly always sites of intense massive star formation, while star formation within the enclosed disks is greatly quenched (e.g., Higdson 1995; Marston & Appleton 1995).¹ Ring galaxies are thus of interest from the standpoint of both the triggering and suppression of star formation on galactic scales. HI interferometry of the Cartwheel ring galaxy provides insight into how star

formation is regulated in these objects (Higdon 1996). Its outer ring possesses $\approx 90\%$ of the galaxy’s total neutral atomic ISM, resulting in very high HI surface densities (Σ_{HI}), peaking at $\Sigma_{\text{HI}} = 75 M_{\odot} \text{ pc}^{-2}$ for 3 kpc linear resolution.² At the same time, the Cartwheel’s interior disk, inner ring, and nucleus are HI poor, with $\Sigma_{\text{HI}} \lesssim 2 M_{\odot} \text{ pc}^{-2}$ (3σ). Star formation triggering/suppression can be understood in terms of a local gravitational stability criterion, as parameterized by the surface density of the neutral atomic ISM. The Cartwheel’s outer HI ring exceeds the gas surface density threshold for robust star formation (Kennicutt 1989), while the enclosed gas poor disk is stable against the growth of large scale gravitational perturbations and subsequent star formation. Whether simple gravitational stability ideas can explain the distribution of star formation in other large and evolved ring galaxies remains to be seen.

Stars form in the cold molecular ISM, so HI only tells part of the story. A more complete understanding of star formation triggering and suppression in ring galaxies requires the determination of the *molecular* ISM’s properties as well. This has proven difficult since ring galaxies as a rule are not luminous in the ^{12}CO rotational transitions (e.g., Horellou et al. 1995), which are the standard tracers of H_2 in galaxies. This has been attributed to low metal abundances in the ring from the “snow-plowing” of largely unenriched gas from the outer disk as the ring propagates outward. In this paper we examine the atomic and molecular ISM of the southern ring galaxy AM0644-741 (Arp & Madore 1987), also known as the “Lindsay-Shapley Ring”, using data from the Australia Telescope Compact Array (ATCA)³ and the 15 m Swedish ESO Submillimeter Telescope (SEST)⁴ at La Silla, Chile. B -band and $\text{H}\alpha$ images are shown in Figure 1 and a summary of AM0644-741’s global properties is given in Table 1. The ring is very large ($D_{\text{ring}} = 95''$, or 42 kpc at the assumed distance), with only those of the Cartwheel and AM1724-622 (the “Sacred Mushroom”) being larger (Higdon 1995, 1996; Wallin & Struck 1994). Optical spectroscopy by Few, Madore & Arp (1982, hereafter FMA) showed the ring to be rich in giant star-forming complexes, and expanding in accord with collisional models. $\text{H}\alpha$ imaging by Higdon & Wallin (1997, hereafter HW97) showed massive star formation to be confined to a pair of (apparently) interlocking rings, with a total $\text{SFR} = 3.6 M_{\odot} \text{ yr}^{-1}$ with no extinction correction. (An unresolved nuclear source contributes $\approx 1\%$ of the total $F_{\text{H}\alpha}$.) The offset nucleus and asymmetric distribution of $\text{H}\alpha$ emission point to an off-centered collision with the elliptical $1.8'$ (49 kpc in projection) to the southeast in Figure 1. N -body/smoothed particle hydrodynamics (SPH) models of this

¹One notable exception is the “Sacred Mushroom” galaxy (AM1724-622), whose red and low surface brightness optical ring shows no evidence of recent star formation, and indeed suggests that the pre-collision galaxy was an S0 (Wallin & Struck 1994).

²HI surface density and column density are related: $1 M_{\odot} \text{ pc}^{-2} = 1.25 \times 10^{20} \text{ atoms cm}^{-2}$.

system have been presented in Antunes & Wallin (2007). Horellou et al. (1995) reported the detection of $^{12}\text{CO}(J = 1 - 0)$ emission from the galaxy’s nucleus using the SEST (though at a velocity 300 km s^{-1} smaller than v_{sys}). While nuclear ^{12}CO emission does not guarantee the detection of molecular gas in the starburst rings (e.g., Horellou et al. 1998), it motivated the work presented in this paper.

We use the ATCA HI data to trace the distribution and kinematics of AM0644-741’s neutral atomic ISM on $\approx 3 \text{ kpc}$ scales, which is sufficient to allow direct comparisons with published VLA HI observations of the Cartwheel. The radio continuum data additionally provides an obscuration free tracer of current massive star formation. The SEST is used to measure both $115 \text{ GHz } ^{12}\text{CO}(J = 1-0)$ and $230 \text{ GHz } ^{12}\text{CO}(J = 2-1)$ line emission in the ring galaxy. We take advantage of improved receiver sensitivity, particularly at 230 GHz , to reexamine the galaxy’s molecular gas content. A major advantage of 230 GHz observations is the $22''$ FWHM beam, which allows the measurement of ^{12}CO emission in the ring, disk, and nucleus separately, permitting the best census of the molecular ISM in a robustly star-forming ring galaxy in the pre-ALMA era.

We also utilize far-ultraviolet (FUV) images of AM0644-741 obtained with the Galaxy Evolution Explorer (GALEX), ground-based optical imaging obtained at the Cerro-Tololo Inter-American Observatory (CTIO)⁵, and images at 4.5 , 24 , and $70 \mu\text{m}$ from the Spitzer Space Telescope (*Spitzer*, Werner et al. 2004)⁶, as well as optical spectra of AM0644-741’s ring using ESO’s 3.6 m telescope. The combined data are used to determine basic properties of the neutral atomic and molecular ISM throughout AM0644-741’s ring, nucleus and enclosed disk for comparison with star formation activity as measured in the FUV, optical, infrared, and radio. Among the questions we wish to address is whether the ring’s neutral ISM is dominated by atomic or molecular gas, and which local property is primarily responsible for setting the molecular fraction. We also wish to know if the distribution of star formation in AM0644-741’s ring and disk can be understood in terms of simple gravitational stability arguments as is the case in the Cartwheel, and whether or not the inclusion of the molecular ISM significantly modifies the results of such an analysis. H_2 mass measurements are also necessary for estimates of star formation efficiency (SFE), which have been determined in nearby galaxies (e.g., Young et al. 1996; Rownd & Young 1999). In short, how do

³The Australia Telescope Compact Array is part of the Australia Telescope, which is funded by the Commonwealth of Australia for operations as a National Facility managed by CSIRO.

⁴The SEST is operated jointly by the European Southern Observatory (ESO) and the Swedish National Facility for Radio Astronomy, Chalmers Center for Astrophysics and Space Science.

properties of the star-forming ISM in an evolved ring galaxy compare with other systems?

This paper is organized as follows: The observations and data reduction are outlined in Section 2. The results derived using these observations are presented in Section 3, including the ring’s metallicity, the distribution and kinematics of HI, the relative proportions of molecular and atomic gas, star formation efficiency, and their variations around the ring. We also consider the ring’s gravitational stability, and whether or not star formation follows a Schmidt law. In Section 4 we consider the role played by pressure and ambient FUV radiation field in determining the ring’s molecular fraction. We also discuss our results in the context of an alternate view of ring galaxies, in which the ring represents a self-sustaining propagating starburst. Our conclusions are given in Section 5. Throughout this paper we adopt a flat Λ CDM cosmology based on the 7 year WMAP results (Komatsu et al. 2011), $\Omega_M=0.27$, $\Omega_\Lambda=0.73$, and a Hubble constant of $70.3 \text{ km s}^{-1} \text{ Mpc}^{-1}$, giving AM0644-741 a luminosity distance of 96.9 Mpc and a linear scale of $0.45 \text{ kpc arcsec}^{-1}$.

2. Observations, Data Reduction, and Analysis

2.1. GALEX Ultraviolet Imaging

GALEX provides simultaneous FUV ($\lambda_{\text{eff}} = 1516 \text{ \AA}$, $\Delta\lambda_{\text{FWHM}} = 269 \text{ \AA}$) and NUV ($\lambda_{\text{eff}} = 2267 \text{ \AA}$, $\Delta\lambda_{\text{FWHM}} = 616 \text{ \AA}$) imaging capabilities. Details on the telescope optics, instruments, calibration, and data reduction pipeline can be found in Martin et al. (2005) and Morrissey et al. (2005, 2007). Figure 2 shows an archival FUV image of AM0644-741 taken on 20 September 2003 ($t_{\text{int}} = 3562 \text{ sec}$), which was processed nominally with the *GALEX* pipeline (version 3). The angular resolution is $4.3''$ FWHM (1.9 kpc) and the point-source sensitivity is estimated to be $7.2 \times 10^{-18} \text{ erg s}^{-1} \text{ cm}^{-2} \text{ \AA}^{-1}$ (3σ).

2.2. Optical Imaging and Spectroscopy

AM0644-741 was imaged in *B*, *V*, and *I*-bands on the nights of 1991 February 18-19 using the CTIO 1.5 m telescope. The imaging array was a Tektronics 1024 CCD (TEK1) located at the f/13.6 Cassegrain focus, giving a pixel scale of $0.43 \text{ arcsec pix}^{-1}$ and a 7.4

⁵CTIO is operated by AURA, Inc., under contract with the National Science Foundation.

⁶Spitzer Space Telescope is operated by JPL, California Institute of Technology for the National Aeronautics and Space Administration.

square field. Multiple 600-second integrations were made in each filter. The nights were photometric, and *UBVRI* standards (E4 Graham 1982) were used to calibrate the data. Reduction and calibration was routine and done using *IRAF* and IDL. The seeing was mediocre ($\approx 2''$ FWHM) but adequate given the angular resolution of the other data. Zero-points in Bessel (1979) were used to convert from magnitudes to flux units.

Star-forming complexes along the western half of AM0644-741’s ring were observed with the EFOSC2 imaging spectrograph on the *ESO* 3.6 m telescope at La Silla on 2002 December 6. Spectra covering $6200 - 7800 \text{ \AA}$ were obtained in multi-object mode (MOS) using aperture masks, together with the Loral CCD (2048×2048 , $15 \text{ } \mu\text{m}$ pixels) and grism #10 (600 mm^{-1} ; $0.95 \text{ \AA pix}^{-1}$ dispersion). Three slitlet positions are shown in Figure 1. Apertures situated on blank sky regions were used for sky-subtraction. Blue spectra covering $3500 - 5500 \text{ \AA}$ were also taken for these masks using grism #3 (400 mm^{-1} ; 1.5 \AA pix^{-1} dispersion). Flat-fielding problems rendered these data unusable, however, and only the red spectra are used in the following analysis. Standard routines in *IRAF* were used to extract (*apall*) and calibrate (*identify*, *calibrate*) the red EFOSC2 spectra, which are shown in Figure 3. Emission line fluxes and uncertainties were measured using *splot*, and are discussed below.

2.3. *Spitzer* IRAC and MIPS Imaging

AM0644-741 was imaged at $4.5 \text{ } \mu\text{m}$ with IRAC on 2005 April 3 as part of our Guaranteed Time Program (PID 197). Preliminary data processing and calibration were carried out using the standard IRAC pipeline (S12.0.2), producing a set of basic calibrated data products (BCDs). Additional processing was done using the MOPEX software package (Makovoz & Marleau 2005). This consisted of “self-calibration” to improve flat-fielding and background subtraction after the deletion of defective “first scans”, and re-mosaicking. The resulting image is shown in Figure 2. At $4.5 \text{ } \mu\text{m}$ the diffraction limited angular resolution is $3.0''$ (1.3 kpc). The 1σ sensitivity of the final image is $0.003 \text{ MJy sr}^{-1}$, though it should be noted that the photometric zero-point is accurate to $\pm 5\%$.

Spitzer MIPS observations of AM0644-741 at 24 and $70 \text{ } \mu\text{m}$ were also obtained on 2005 April 3 as part of the same GT program. As with the IRAC data, preliminary data processing and calibration were carried out using the standard MIPS pipeline (version S13.2) as described in Gordon et al. (2005), with additional processing in MOPEX to improve the flat-fielding, background removal, and final mosaic. The resulting 24 and $70 \text{ } \mu\text{m}$ images are also shown in Figure 2. The diffraction limited resolution is $5.7''$ FWHM (2.5 kpc) at $24 \text{ } \mu\text{m}$ and $16.6''$ FWHM (7.3 kpc) at $70 \text{ } \mu\text{m}$. Prominent Airy diffraction rings are visible around several of the brightest point-sources in the outer ring at $24 \text{ } \mu\text{m}$. The 1σ sensitivity of the

MIPS images is 0.013 and 0.46 MJy sr^{-1} at 24 and $70 \text{ } \mu\text{m}$ respectively, or 3.1×10^{-7} and $1.1 \times 10^{-5} \text{ Jy arcsec}^{-2}$, though again, the zero-point is accurate to $\pm 5\%$ (see Engelbracht et al. 2007, for a discussion of this and other calibration issues).

2.4. ATCA HI Interferometry

AM0644-741 was observed using the ATCA between 1996 August to 1998 May with a variety of array configurations (Table 2). The baselines ranged from 30.6 m to 5.97 km with a total of 114 hr on target. The ATCA’s correlator was configured to provide a spectral line bandpass of 8 MHz subdivided into 512 channels separated by 3.3 km s^{-1} and centered on a frequency of 1390.0 MHz . Simultaneous continuum observations were made with a 128 MHz wide bandpass (32 channels) centered at 1380.0 MHz . The flux scale and bandpass shape were calibrated using observations of radio source 1934-638 ($S_{1390\text{MHz}} = 14.95 \text{ Jy}$), while drifts in the antenna gain coefficients were corrected using periodic observations of the nearby radio source 0454-801 ($S_{1390\text{MHz}} = 0.9 \text{ Jy}$).

The UV data from each observation was edited and calibrated separately using an *ATNF* implementation of *NRAO*’s Astronomical Image Processing System (AIPS) package. This included the correction for Doppler shifts during each scan since the ATCA correlator does not frequency track. Data from all configurations were concatenated into final line and continuum data sets using the AIPS task DBCON, which were separately imaged and CLEANed using the task IMAGR. The continuum was subtracted from the spectral line data set prior to imaging using a combination of the tasks UVSUB and UVLIN. HI line image cubes were made using both *natural* ($\theta_{\text{FWHM}} = 12.''2 \times 9.''4$) and *robust* ($ROBUST = -0.5$; $\theta_{\text{FWHM}} = 7.''9 \times 6.''7$) weighting. Eight successive 3.3 km s^{-1} channels were averaged together during imaging, which yielded (after discarding some data near the bandpass edges) 44 channels separated by 27.5 km s^{-1} . The rms noise in the *natural* weighted channel maps was $0.38 \text{ mJy beam}^{-1}$, while that in the *robust* weighted channel maps was $0.48 \text{ mJy beam}^{-1}$, which is close to the expected sensitivity given the low elevation of AM0644-741 ($\lesssim 40^\circ$) during a significant fraction of the observations.

Integrated HI and flux-weighted velocity images were made using the AIPS routine MOMNT and are shown in Figure 4, where they have been superposed on optical *B*-band and *H* α gray scale images. HI masses in solar units are calculated using

$$M_{\text{HI}} = 2.36 \times 10^5 \text{ D}_{\text{Mpc}}^2 \int S_\nu(v) dv, \quad (1)$$

where $S_\nu(v)$ is the flux density in Janskys for a given velocity channel and dv represents the channel separation in km s^{-1} . This equation is valid in the optically thin limit. We

measured the run of radial velocity (v_{rad}) around the ring in 10° increments using the flux-weighted velocity image shown in Figure 4. This will be used in the analysis of the ring’s kinematics in Section 3. The total HI spectrum for AM0644-741 using the *robust* weighted data is presented in Figure 11. All radial velocities reported in this paper assume the optical/barycentric definition.

A *robust* weighted 20 cm continuum image ($\theta_{\text{FWHM}} = 7.''9 \times 6.''7$) was made by averaging the 16 4-MHz continuum channels least affected by radio interference. The *rms* in the cleaned image is $20 \mu\text{Jy beam}^{-1}$, which is also near the expected sensitivity. This is shown contoured on the $\text{H}\alpha$ gray scale image in Figure 4.

2.5. SEST ^{12}CO Mapping

^{12}CO observations were carried out on the nights of 1999 July 18-22 and 2000 September 1-5 using the SEST. The telescope was operated in dual 115/230 GHz mode with SIS receivers. Both back-ends were acoustic-optical spectrometers providing total band-passes of 1300 and 1600 km s^{-1} in the redshifted $^{12}\text{CO}(1-0)$ and $^{12}\text{CO}(2-1)$ lines, with channel separations of 1.3 and 1.6 km s^{-1} respectively. The telescope FWHM beam widths at these frequencies are $43''$ (18.9 kpc) and $22''$ (9.7 kpc). Dual beam-switching mode using a focal plane chopper wheel rotating at 6 Hz ($2.5-12'$ beam throw) was used to ensure flat baselines. Pointing was checked regularly throughout the run using SiO masers, and is believed to be accurate to within $5''$. The highest quality data were obtained over the September 2000 run. System temperatures were exceptionally low on these nights, with $T_{\text{sys}} = 230-300$ K at 230 GHz.

We searched the ring for $^{12}\text{CO}(2-1)$ emission using $22''$ beam separations, switching to $11''$ spacing when line emission was detected. Altogether, we observed 14 positions in AM0644-741’s ring as well as single pointings at the optical nucleus and enclosed disk (Table 3). At each observed position, the acoustic-optical spectrometer’s central frequency was set to correspond to the flux-weighted HI systemic velocity. For the ring galaxy’s nucleus and disk the central frequency corresponded to the optical systemic velocity (6750 km s^{-1} ; FMA). The observed positions and beam FWHMs are shown in Figures 5 and 6 superposed on a $\text{H}\alpha$ gray scale image, along with the *robust* weighted HI contours. The 115 and 230 GHz spectra were reduced and analyzed in an identical manner using the CLASS software package.⁷ Scans showing curved baselines or ripples were discarded. The remaining scans

⁷The CLASS analysis package is part of the GILDAS collection of software produced and maintained by IRAM. See www.iram.fr/IRAMFR/GILDAS for further information.

at each of the 14 observed positions were then coadded, smoothed to a resolution of 30 km s^{-1} and rebinned to a 10 km s^{-1} channel separation. Linear baselines were then subtracted. The final $^{12}\text{CO}(1-0)$ and $^{12}\text{CO}(2-1)$ spectra are shown in Figures 5 and 6. Typical *rms* for the final 115 and 230 GHz spectra are $\approx 1.5 \text{ mK}$ and $\approx 1.0 \text{ mK}$ respectively. Integrated line intensities are defined as

$$I_{1-0} = \int T_{\text{A}}^*(J = 1 - 0) dv \quad \text{and} \quad I_{2-1} = \int T_{\text{A}}^*(J = 2 - 1) dv \quad (2)$$

for the 115 and 230 GHz lines. Where a single narrow line component was apparent, line intensities and uncertainties were derived by fitting single Gaussian profiles using routines in CLASS. Otherwise, intensities were derived by summing the spectra over the full range of channels showing emission. Uncertainties in this case were estimated using $\sigma = \sigma_{\text{base}} \sqrt{\Delta v_{\text{res}} \Delta v_{\text{CO}}}$, where σ_{base} is the *rms* in the channels not showing line emission, Δv_{res} is the velocity resolution and Δv_{CO} is the line FWHM, both in km s^{-1} . Derived line intensities and uncertainties, peak T_{A}^* , central velocities and widths (FWHM), and *rms* are listed in Table 4.

Because of the higher sensitivity and smaller beam diameter, we calculate H_2 masses with the 230 GHz spectra using

$$M_{\text{H}_2} = \frac{2m_{\text{p}} I_{2-1} R(\frac{1-0}{2-1}) X_{\text{CO}} \Delta\Omega_{230}}{\epsilon_{\text{mb}} \epsilon_{\text{source}}}, \quad (3)$$

where m_{p} is the proton mass, $R(\frac{1-0}{2-1})$ is the locally determined I_{1-0}/I_{2-1} ratio, ϵ_{mb} is the SEST main-beam efficiency ($\epsilon_{\text{mb}} = 0.70/0.50$ at 115/230 GHz, 2002 *SEST Handbook*), X_{CO} is the $I_{\text{CO}} - N_{\text{H}_2}$ conversion factor, and $\Delta\Omega_{230}$ is the beam area at 230 GHz. We further correct the main-beam efficiency by the source-coupling factor (ϵ_{source}) as well as the effect of overlapping beams. Both were calculated by numerically simulating the observations under the assumption that the molecular gas is distributed to first order like the $\text{H}\alpha$ ring. This should be a reasonable approximation given the strong orbit crowding evident in the multiwavelength images.⁸ The H_2 surface density is defined $\Sigma_{\text{H}_2} = M_{\text{H}_2}/\Delta\Omega_{\text{ring}}$, where $\Delta\Omega_{\text{ring}}$ is the ring's solid angle, i.e., a $\approx 9'' \times 22''$ rectangle, ignoring the slight curvature of the ring within a beam. Unless otherwise noted, we will quote HI and H_2 masses and surface densities without a correction for helium, which entails scaling by a factor of 1.36 (Kennicutt 1989). This correction will be necessary when we consider the ring's gravitational stability and pressure.

⁸The assumed source geometry affects the value of $R(\frac{1-0}{2-1})$. For sources small with respect to both the 115 and 230 GHz beams $R(\frac{1-0}{2-1})$ is $(\frac{I_{1-0}}{I_{2-1}})(\frac{\Delta\Omega_{115}}{\Delta\Omega_{230}}) = 4 (\frac{I_{1-0}}{I_{2-1}})$. To account for the fact that the size of the CO

3. Results

3.1. Metal Abundances in the Ring and the CO-H₂ Conversion Factor

Using ¹²CO intensity as a proxy for H₂ requires the correct X_{CO} . Empirical calibrations for molecular clouds in the Galactic plane using a variety of techniques find $X_{\text{CO}} \approx 2 \times 10^{20}$ mol cm⁻² (K km s⁻¹)⁻¹ (e.g., Dickman 1978; Solomon et al. 1987; Dame et al. 2001), implying that physical conditions in the ISM (e.g., temperature, density, and ambient radiation field) average out to a great extent when integrated over a large number of clouds, i.e., for large beam sizes. One property that does not average out is the ISM’s metal abundance. Low metallicity reduces CO emission directly by decreasing the available C and O needed to form CO, and indirectly by reducing the dust columns required to shield the more fragile CO molecule from photodissociation within individual clouds. Since the formation and survival of H₂ is much less sensitive to metallicity, X_{CO} is expected to depend on abundance (Maloney & Black 1988). The precise nature of the dependence is a matter of contention. Determinations of X_{CO} in other galaxies that assume molecular clouds are in virial equilibrium find fairly weak metallicity dependence (e.g., Wilson 1995), while studies using infrared dust emission to estimate the total gas mass find strong metallicity dependence (e.g., Israel 1997; Leroy et al. 2009), and in particular, X_{CO} that are ≈ 3 –10 times larger than the Galactic value. It is thus important to determine the metallicity in order to at least constrain the allowed range in derived H₂ masses and surface densities.

We use H α , [N II] λ 6584 and [S II] λ 6717, 6731 emission line fluxes extracted from the red EFOSC2 spectra in Figure 3 to determine oxygen abundances along the western half of AM0644-741’s ring. This is done following the empirical calibration given in Table 6 of Nagao et al. (2006),

$$\log(F_{[\text{N II}]\lambda 6584}/F_{\text{H}\alpha}) = 96.64 - 39.94y + 5.22y^2 - 0.22y^3 \quad (4)$$

and

$$\log(F_{[\text{N II}]\lambda 6584}/F_{[\text{S II}]}) = -80.62 + 31.32y - 4.10y^2 + 0.18y^3 \quad (5)$$

where $y \equiv 12 + \log(\text{O}/\text{H})$ and where $F_{[\text{S II}]}$ is the sum of the 6717 and 6731 Å [S II] lines. These relations were established using spectra of extra-galactic HII regions spanning $7.0 \lesssim 12 + \log(\text{O}/\text{H}) \lesssim 9.4$ taken from the literature and the Sloan Digital Sky Survey database. In each instance accurate oxygen abundances were determined either directly using the temperature sensitive [O III] λ 4363 line or through detailed photoionization modeling. The

emitting region (i.e., the ring) is larger in the 115 GHz beam, $R(\frac{1-0}{2-1})$ becomes $(\frac{I_{1-0}}{I_{2-1}})(\frac{\Delta\Omega_{115}}{\Delta\Omega_{230}})(\frac{\Delta\Omega_{\text{source}}}{\Delta\Omega_{115}}) \approx 2 (\frac{I_{1-0}}{I_{2-1}})$.

[N II] $\lambda 6584/\text{H}\alpha$ and [N II] $\lambda 6584/[\text{S II}]$ ratios have the added advantage of being insensitive to extinction. We find $F_{[\text{N II}]\lambda 6584}/F_{\text{H}\alpha} = 0.36 \pm 0.02$, 0.38 ± 0.01 , and 0.38 ± 0.02 at the three positions, which yields $12+\log(\text{O}/\text{H})=9.04 \pm 0.15$, 9.09 ± 0.14 , and 9.09 ± 0.14 , respectively, using Equation (4), with the uncertainty dominated by the dispersion in Nagao et al.’s graph (see their Figure 6). For the same three regions we measure $F_{[\text{N II}]\lambda 6584}/F_{[\text{S II}]} = 1.05 \pm 0.18$, 1.51 ± 0.07 , and 1.51 ± 0.12 , respectively, which gives using Equation (5) $12+\log(\text{O}/\text{H})=8.96 \pm 0.10$, 9.11 ± 0.06 , and 9.10 ± 0.08 . The two sets of oxygen abundances are in good agreement (imperfect night-sky line subtraction may be partially responsible for the lower abundance at P5 using $F_{[\text{N II}]\lambda 6584}/F_{[\text{S II}]}$). Both line ratios give $12+ \log(\text{O}/\text{H}) \approx 9.09$, which significantly exceed recent determinations of the Sun’s oxygen abundance, e.g., $12+\log(\text{O}/\text{H})_{\odot} = 8.73 - 8.79$ (Caffau & Ludwig 2008). The western half of AM0644-741’s ring thus exceeds solar metallicity and shows no significant azimuthal variation despite (as we show below) large changes in Σ_{HI} , $\Sigma_{\text{H}\alpha}$, and molecular fraction. We therefore adopt the Galactic $I_{\text{CO}} - N_{\text{H}_2}$ determined by Strong et al. (1988, $X_{\text{CO}} = (2.3 \pm 0.3) \times 10^{20} \text{ mol cm}^{-2} (\text{K km s}^{-1})^{-1}$) for AM0644-741’s ring.

3.2. Star Formation in AM0644-741 Revisited

For a distance of 96.9 Mpc the ring galaxy’s $\text{H}\alpha$ luminosity is $(6.13 \pm 0.06) \times 10^{41} \text{ erg s}^{-1}$ (HW97) after correcting for Galactic extinction ($A_V = 0.5$; Corwin, Buta & de Vaucouleurs 1994). This corresponds to $\text{SFR} = 4.9 \pm 0.1 M_{\odot} \text{ yr}^{-1}$ (Kennicutt 1998a), giving AM0644-741 one of the highest SFRs among ring galaxies.⁹ Internal extinction may cause the SFR to be significantly underestimated, especially if the ISM is highly concentrated in the ring (e.g., $A_V \approx 2$ in the Cartwheel’s ring, Fosbury & Hawarden 1977), representing a ≈ 4 -fold increase in $L_{\text{H}\alpha}$). We therefore consider three independent methods to determine internal $A_{\text{H}\alpha}$ in the ring.

3.2.1. Optical-Infrared Estimates of the SFR

Emission at 24 and 70 μm from galaxies originates in dust illuminated either by an active nucleus or young stars. The $\text{H}\alpha$ and MIPS images clearly show that AM0644-741’s mid- and far-infrared (*FIR*) emission originates in the star-forming ring; the unresolved nuclear component makes a negligible contribution. This permits two independent approaches to

⁹Excluding systems with obvious AGN, the median SFR in Marston & Appleton’s sample of ring galaxies is $2.8 M_{\odot} \text{ yr}^{-1}$ after correcting for foreground extinction.

determine the extinction free SFR - calculating SFR directly from the ring galaxy’s infrared luminosity and by combining $L_{\text{H}\alpha}$ and $L_{24\mu\text{m}}$ to derive $A_{\text{H}\alpha}$.

Kennicutt (1998b) found $\text{SFR} = 1.72 \times 10^{-10} L_{\text{IR}} M_{\odot} \text{ yr}^{-1}$, where L_{IR} is the $8 - 1000 \mu\text{m}$ luminosity, which in units of L_{\odot} is $L_{\text{IR}} = 1.8 \times 10^{12} (13.48 L'_{12} + 5.16 L'_{25} + 2.58 L'_{60} + L'_{100})$ for *IRAS* luminosity densities $L'_i = 4\pi D_L^2 F_i$ (Sanders & Mirabel 1996). Here F_i is the *IRAS* flux density in Janskys and D_L is the source’s luminosity distance. Infrared flux densities for AM0644-741 were taken from the *IRAS Faint Source Catalog* (Moshir et al. 1990) and are listed in Table 1. We find $L_{\text{IR}} = (4.9 \pm 0.2) \times 10^{10} L_{\odot}$, giving $\text{SFR} = 7.7 \pm 0.3 M_{\odot} \text{ yr}^{-1}$. For the above $L_{\text{H}\alpha}$, $A_{\text{H}\alpha} \approx 1$ is implied.

We next use the tight correlation between $24 \mu\text{m}$ flux densities and Pa α line fluxes in M51a’s star-forming regions (Kennicutt et al. 2007, hereafter K07) to derive $A_{\text{H}\alpha}$. We first measure the $24 \mu\text{m}$ and $\text{H}\alpha$ luminosities ($L_{24\mu\text{m}}$ and $L'_{\text{H}\alpha}$) within $22''$ FWHM apertures centered on the ring positions observed with the SEST. These are shown (after normalizing by beam area) as a function of ring position angle in Figure 7. $L'_{\text{H}\alpha}$ are first corrected for 0.33 magnitudes of Galactic foreground extinction. Internal extinction (assuming a foreground screen geometry) is calculated using

$$A_{\text{H}\alpha} = 2.5 \log \left(1 + \frac{a \nu L_{24\mu\text{m}}}{L'_{\text{H}\alpha}} \right), \quad (6)$$

with $a = 0.038 \pm 0.005$. Calzetti et al. (2007) confirm this relation using 33 nearby galaxies from the SINGS sample (Kennicutt et al. 2003) covering a wide range in Hubble type and metallicity, though they find a slightly smaller a (0.031 ± 0.006). We will adopt the a in K07 to allow a direct comparison with M51a’s star formation law in Section 3.6.

Derived internal $A_{\text{H}\alpha}$ are listed in Table 5, along with corrected $\text{H}\alpha$ luminosities. $A_{\text{H}\alpha} \approx 0.9$ at all 14 ring positions, which agrees with the $A_{\text{H}\alpha}$ estimated with L_{IR} above. We calculate a flux-weighted mean $A_{\text{H}\alpha}$ of 0.92 ± 0.05 for the entire ring, and an extinction corrected $L_{\text{H}\alpha} = (1.43 \pm 0.06) \times 10^{42} \text{ erg s}^{-1}$, giving $\text{SFR} = 11.2 \pm 0.4 M_{\odot} \text{ yr}^{-1}$ (Kennicutt 1998a). This is in reasonable accord with the SFR based on the galaxy’s $8 - 1000 \mu\text{m}$ luminosity, given the scatter in the $L_{\text{IR}} - \text{SFR}$ relation.

3.2.2. Radio Continuum Estimates of SFR

20 cm continuum emission in star-forming galaxies is dominated by synchrotron emission from relativistic electrons spiraling around magnetic field lines. These electrons originate in supernovae, which provide the connecting link between star formation and radio emission. Radio continuum emission from the ring dominates the weak ($\approx 2\%$) nuclear source and

enclosed disk, and resembles the galaxy’s morphology at $H\alpha$ and the infrared.¹⁰ The galaxy’s radio luminosity provides a second extinction free measure of the SFR, though the physics connecting massive star formation and the ensuing radio emission is complex (e.g., particle confinement, magnetic field strength, and even the radiative lifetime of radio supernova remnants) and still only partially understood.

We calculate the ring’s radio continuum density ($L_{20\text{cm}}$, in W Hz^{-1}) with

$$L_{20\text{cm}} = 4\pi D_L^2 (1+z)^{\alpha-1} F_\nu(20\text{cm}), \quad (7)$$

where $F_\nu(20\text{cm})$ is the 20 cm flux density in Janskys, D_L is the luminosity distance, and α is the source’s radio spectral index ($F_\nu \propto \nu^{-\alpha}$) taken to be 0.7, a value appropriate for galaxies dominated by star formation. We find $L_{20\text{cm}} = (3.2 \pm 0.2) \times 10^{22} \text{ W Hz}^{-1}$, implying $\text{SFR} = 17.6 \pm 0.9 M_\odot \text{ yr}^{-1}$ (Hopkins et al. 2003). While significantly higher than the $H\alpha$ and infrared SFRs, this estimate is consistent with the $H\alpha$ and IR SFRs given the factor of ≈ 1.6 scatter in the $\text{SFR}_{20\text{cm}} - \text{SFR}_{H\alpha}$ relation in Hopkins et al.

We note that the connection between 20 cm emission and the SFR appears less direct than for other tracers, and indeed Kennicutt et al. (2009) find that the relation between 20 cm and the Balmer-corrected $L_{H\alpha}$ in the SINGS sample is more nonlinear than for the IR-based tracers. We therefore adopt $A_{H\alpha} \approx 0.9$ and $\text{SFR} = 11 M_\odot \text{ yr}^{-1}$ throughout the remainder of this paper.

3.3. The Stellar Ring

In the collisional picture, the stellar ring plays a role similar to that of a spiral density wave. Regions of high stellar mass surface density (Σ_* , in $M_\odot \text{ pc}^{-2}$) will correspond to regions of strongest orbit crowding, which is where the molecular cloud collision frequency and relative speed is expected to peak. The stellar component may also contribute significantly to the ring’s gravitational stability and pressure.

We derive Σ_* in the ring by first calculating $M_*/L_{I,\odot}$, the I -band stellar mass to luminosity ratio. This is done by fitting integrated FUV, optical, and $4.5 \mu\text{m}$ luminosity densities from each $22''$ diameter SEST aperture to Starburst99 spectral energy distributions (SEDs; Leitherer et al. 1999; Vazquez & Leitherer 2005). In modeling the ring we

¹⁰The elliptical intruder galaxy to the southeast is not detected in radio continuum ($S_{20\text{cm}} < 0.14 \text{ mJy}$, 3σ), though we do detect ($S_\nu = 0.45 \pm 0.05 \text{ mJy}$) emission from the nucleus of the face-on barred spiral companion $\approx 1.5'$ north of AM0644-741’s nucleus.

assume a constant SFR of $1 M_{\odot} \text{ yr}^{-1}$ over a 120 Myr lifetime and a Salpeter initial mass function ($M_{\text{up}} = 100 M_{\odot}$). The stellar tracks incorporate thermally pulsing asymptotic giant branch stars. The FUV-4.5 μm luminosity densities are corrected for both internal and Galactic foreground extinction ($R_V = 3.1$). The stellar mass within a given aperture was determined by scaling the SED by an amount h until they matched the observed data points (i.e., $M_*/M_{\odot} = h \times \text{Age} \times \text{SFR}$). We find a small range in stellar masses among the apertures, with $M_* = (1.2 - 2.2) \times 10^9 M_{\odot}$. The I -band mass to light ratio at each position follows after dividing M_* by the corresponding I -band luminosity in solar units, defined

$$L_I = 4\pi D_L^2 F_I \Delta\nu_I L_{I,\odot}^{-1}, \quad (8)$$

where F_I is the I -band flux density in Janskys, $\Delta\nu_I = 7.55 \times 10^{13} \text{ Hz}$ is the filter passband, and $L_{I,\odot}$ is the Sun’s I -band luminosity ($3.71 \times 10^{25} \text{ W}$; Bessel 1979). We find $M_*/L_{I,\odot} \approx 0.22$, with only small variations around the ring. No dependence on either $\Sigma_{\text{H}\alpha}$ or optical color is evident. Σ_* follows by multiplying $M_*/L_{I,\odot}$ by the ring’s average I -band surface brightness (Σ_I , in $L_{\odot} \text{ pc}^{-2}$) at each position. The result is shown in Figure 7 and listed in Table 6. Σ_* ranges from $21 - 51 M_{\odot} \text{ pc}^{-2}$, peaking in the ring’s southwest quadrant. $\Sigma_{24\mu\text{m}}$, $\Sigma_{\text{H}\alpha}$, and Σ_* show similar azimuthal variations.

3.4. AM0644-741’s Neutral ISM

3.4.1. The Distribution of Atomic and Molecular Gas

The *robust* and *natural* weighted map cubes yield nearly identical HI masses, and we use the higher angular resolution data throughout this paper. We find $M_{\text{HI}} = (2.01 \pm 0.06) \times 10^{10} M_{\odot}$ for AM0644-741 using the *robust* moment-0 map. We obtain a $\approx 50\%$ higher HI mass ($2.94 \pm 0.07 \times 10^{10} M_{\odot}$) using integrated HI profile in Figure 11. This wide discrepancy may arise from the ring galaxy’s large total velocity width coupled with (as we show) often wide and complicated HI line profiles which may be left out in the moment analysis. We will adopt the larger M_{HI} for the determination of global quantities.

The distribution of HI is shown in gray scale and as logarithmic contours of Σ_{HI} in Figure 4. Atomic hydrogen is distributed non-uniformly around the ring, as expected from an off-centered collision. Roughly half of the galaxy’s HI is concentrated in a 20 kpc long arc coincident with the optical ring’s southwest quadrant, where the highest HI surface density ($\Sigma_{\text{HI}} = 110 M_{\odot} \text{ pc}^{-2}$) is found. Another 1/3 of the total M_{HI} is distributed along the optical ring’s southeastern quadrant, where the gas is clumpier, lower in Σ_{HI} ($\approx 20 - 35 M_{\odot} \text{ pc}^{-2}$), and more broadly distributed. The northern half of AM0644-741’s ring is HI deficient by comparison. Note that HI is detected only from the innermost of the twin $\text{H}\alpha$ rings in the

northern quadrant using the *robust* data. Patchy HI with $\Sigma_{\text{HI}} = 3 - 4 M_{\odot} \text{ pc}^{-2}$ is visible at the position of the outermost ring using the *natural* weighted data.

Molecular gas is detected at 9 of 14 ring positions observed with the SEST at 230 GHz, as shown in Figure 5: five overlapping beams in the northern quadrant (P3-P7; P.A. = $78^{\circ} - 142^{\circ}$) and four in the southwest (P9-P12; P.A. = $217^{\circ} - 266^{\circ}$). $^{12}\text{CO}(1-0)$ was also detected at these positions (Figure 6). Line intensities and limits are listed in Table 4. The latter are estimated assuming $\Delta v_{\text{HI}} = \Delta v_{\text{CO}}$. Using Equation (3), we find $\Sigma_{\text{H}_2} = 5.0 - 24.1 M_{\odot} \text{ pc}^{-2}$ around the ring, peaking at P7 in the northern quadrant (Figure 7). We derive integrated line intensities of $I_{2-1} = 9.50 \pm 0.29 \text{ K km s}^{-1}$ and $I_{1-0} = 3.08 \pm 0.12 \text{ K km s}^{-1}$ in the northern quadrant, and $I_{2-1} = 4.02 \pm 0.24 \text{ K km s}^{-1}$ and $I_{1-0} = 0.94 \pm 0.09 \text{ K km s}^{-1}$ in the southwest.¹¹ The two regions show similar excitation, with $R(\frac{1-0}{2-1}) = 0.65 \pm 0.01$ in the northern and 0.47 ± 0.01 in the southwest quadrants. Much larger values are typically found in the centers of spirals (e.g., $R(\frac{1-0}{2-1}) = 1.12 \pm 0.08$; Braine et al. 1993), implying that CO in AM0644-741’s ring is warm and possibly optically thin. We infer H_2 masses in the two ring quadrants of $(1.76 \pm 0.10) \times 10^9 M_{\odot}$ (north) and $(7.70 \pm 0.08) \times 10^8 M_{\odot}$ (southwest), for a total $M_{\text{H}_2} = (2.52 \pm 0.12) \times 10^9 M_{\odot}$. The ring’s *global* molecular fraction ($f_{\text{mol}} \equiv \frac{M_{\text{H}_2}}{M_{\text{HI}} + M_{\text{H}_2}}$) is 0.079 ± 0.005 . As a whole, AM0644-741’s star-forming ring is poor in molecular gas.

Atomic and molecular gas follow very different distributions in the ring (Figure 7). HI is strongly peaked in the southwest quadrant ($\Sigma_{\text{HI}} = 60 - 90 M_{\odot} \text{ pc}^{-2}$). While H_2 shows more point to point variation, Σ_{H_2} is on average $\approx 50\%$ higher in the northern ring quadrant ($\bar{\Sigma}_{\text{H}_2} = 15 M_{\odot} \text{ pc}^{-2}$ vs. $11 M_{\odot} \text{ pc}^{-2}$). The northern quadrant is in fact the only part of AM0644-741 where Σ_{H_2} and Σ_{HI} are comparable. Note that there are *two* $\text{H}\alpha$ rings within most of the 230 GHz SEST beams in the northern quadrant (see Figure 5), and we may be overestimating Σ_{H_2} at P4-P7 by assuming all the CO to be confined to a single $9'' \times 22''$ ring segment, possibly by as much as 50%. This caveat should be kept in mind in the following discussion.

Figure 8 shows the azimuthal variations in f_{mol} around the ring. Large systematic variations are evident. Perhaps the most surprising result is that $f_{\text{mol}} \gtrsim 0.5$ in only three ring positions, all in the northern quadrant. Elsewhere, and notably throughout the southwest quadrant, $f_{\text{mol}} \approx 0.1 - 0.3$. The ring’s ISM appears to be overwhelmingly *atomic* rather than molecular where star formation is most intense.

HI is not detected from AM0644-741’s nucleus ($\Sigma_{\text{HI}} < 0.2 M_{\odot} \text{ pc}^{-2}, 3\sigma$) or from most

¹¹To account for beam overlap, the summed 115 GHz line intensities have been divided by factors of 2.16 and 1.95 in the northern and southwest quadrants, while at 230 GHz the summed line intensities have been divided by 1.25 and 1.30 for the same two regions.

of the region interior to the ring ($\Sigma_{\text{HI}} < 0.1 M_{\odot} \text{ pc}^{-2}, 3\sigma$) assuming $\Delta v = 90 \text{ km s}^{-1}$. Note that HI is considerably more abundant throughout the Cartwheel’s interior, where a patchy $\Sigma_{\text{HI}} \approx 2 - 6 M_{\odot} \text{ pc}^{-2}$ disk component exists (Higdon 1996). Similarly, no molecular gas was detected from AM0644-741’s nucleus ($\Sigma_{\text{H}_2} < 2.1 M_{\odot} \text{ pc}^{-2}, 3\sigma$) or disk ($\Sigma_{\text{H}_2} < 1.8 M_{\odot} \text{ pc}^{-2}, 3\sigma$) assuming $\Delta v = 90 \text{ km s}^{-1}$ and $R(\frac{1-0}{2-1}) = 1.6$ (Braine et al. 1993). The confinement of AM0644-741’s neutral atomic ISM to the 42 kpc ring applies equally well to its molecular component.

There is a sharp drop in Σ_{HI} at the optical ring’s edge. Like the Cartwheel, either AM0644-741’s ring has reached (or exceeded) the original extent of the pre-collision HI disk, or beyond the optical ring the system possesses extremely low HI surface densities (Higdon 1996). No HI is detected from the elliptical intruder ($v_{\text{sys}} = 6700 \text{ km s}^{-1}$; FMA) or the faint optical bridge to AM0644-741, even after extra spatial and velocity smoothing. Likewise, HI was not detected from the face-on barred spiral to the north of AM0644-741 (galaxy “C” in Graham 1974, $v_{\text{sys}} = 7000 \text{ km s}^{-1}$).

3.4.2. The Relative Distributions of Gas and Massive Star Formation

Figure 7 shows that HI and star formation tracers $\Sigma_{24\mu\text{m}}$, $\Sigma_{\text{H}\alpha}$, and $\Sigma_{20\text{cm}}$ have very similar distributions, even peaking at the same positions (P9-10). Σ_{H_2} does not appear simply related with massive star formation in the ring. For example, where Σ_{H_2} peaks in the northern quadrant (P7), massive star formation is near its minimum (e.g., the local peak in $\Sigma_{\text{H}\alpha}$ and $\Sigma_{24\mu\text{m}}$ is at P3). This is in marked contrast with studies of nearby galaxies that find $\Sigma_{\text{H}\alpha}$ and Σ_{H_2} to be well correlated (e.g., K07, Rownd & Young 1999). Figure 8 shows that the ring’s molecular fraction is in fact anti-correlated with $\Sigma_{\text{H}\alpha}$. (We will return to this result in Section 3.6.) The neutral ISM in AM0644-741’s ring appears largely atomic precisely where massive star formation is most intense.

The absence of measurable star formation in the interior disk follows from the lack of a significant gas reservoir, either atomic or molecular. We infer a total $M_{\text{HI}+\text{H}_2} \lesssim 6 \times 10^8 M_{\odot}$ and a mean $\Sigma_{\text{HI}+\text{H}_2} \lesssim 2 M_{\odot} \text{ pc}^{-2}$ over AM0644-741’s interior disk and nucleus. Both limits are 3σ and include a mass contribution from helium. The mass limit is not very stringent since giant molecular associations (GMAs) in local spirals have $M_{\text{H}_2} \approx 3 - 7 \times 10^8 M_{\odot}$ (e.g., Rand 1993, 1995). However, regions with such a low mean surface density are not expected to provide adequate shielding from UV photons which retards the formation of molecular cloud complexes.

3.4.3. Kinematics and Velocity Structure of the Ring

Differential rotation is apparent in the flux-weighted isovelocity contours in Figure 4, with non-circular motions evident as kinks in the velocity field. The distribution of HI interior to the ring is not extensive enough to perform a detailed kinematic analysis (e.g., the derivation of a rotation curve or measuring the radial infall of gas predicted by ring galaxy models). The ring is sufficiently HI rich to explore its kinematics by fitting inclined circular ring models, with and without expansion, to the run of HI radial velocity (v_{rad}) versus position angle (ψ , measured counterclockwise from the northeast line of nodes). These velocities are averages over 10° sectors of a $6''$ wide annulus fit to the $\text{H}\alpha$ ring. Systemic (v_{sys}), circular (v_{cir}), and expansion (v_{exp}) velocities are derived by minimizing the sums of the squares of the residuals between model and observed v_{rad} ,

$$\chi^2 = \sum_{\psi} w_{\psi}^2 [v_{\text{rad},\psi} - v_{\text{sys}} - (v_{\text{cir}} \sin i \cos \psi + v_{\text{exp}} \tan i \sin \psi) / \rho_{\psi}]^2, \quad (9)$$

where

$$\rho_{\psi} = \sqrt{\sec^2 i - \tan^2 i \cos^2 \psi}. \quad (10)$$

In the above, w_{ψ} is the weight assigned to each measurement and i is the inclination, which is $56.^\circ 5 \pm 0.^\circ 7$ from ellipse fitting to the (assumed) inclined circular $\text{H}\alpha$ ring. For the non-expanding ring model, v_{exp} is set to zero in Equation (9). Formal uncertainties in the velocities are calculated with

$$\sigma^2(v_x) = \sum_{\psi} w_{\psi} \left(\frac{\partial v_x}{\partial v_{\psi}} \right)^2 \delta v^2, \quad (11)$$

where $\partial v_{\psi} = v_{\text{model}} - v_{\text{rad}}$ at ring position angle ψ , δv is the velocity resolution in the HI data, taken to be the channel separation (27.5 km s^{-1}), and where v_x can be either v_{sys} , v_{cir} , or v_{exp} . These should be considered lower-limits, since systematic errors (e.g., the assumption of a circular ring) may contribute significantly.

Figure 9 shows the resulting $v_{\text{rad}} - \psi$ diagram fits for inclined circular ring models with (*solid line*) and without (*dashed line*) expansion. The error bars show the local velocity spread within the region used to derive v_{rad} . The expanding circular ring model is clearly the better fit to the data, with derived velocities and formal uncertainties of $v_{\text{sys}} = 6692 \pm 8 \text{ km s}^{-1}$, $v_{\text{cir}} = 357 \pm 13 \text{ km s}^{-1}$, and $v_{\text{exp}} = 154 \pm 10 \text{ km s}^{-1}$. FMA found significantly smaller v_{sys} ($6611 \pm 8 \text{ km s}^{-1}$), v_{cir} ($311 \pm 19 \text{ km s}^{-1}$), and v_{exp} ($128 \pm 14 \text{ km s}^{-1}$) using optical emission lines. These discrepancies do not originate in the analysis routines, since we also derive FMA’s v_{sys} , v_{cir} , and v_{exp} using their “blue” velocities (i.e., calculated using $[\text{O II}] \lambda 3727 \text{ \AA}$, $[\text{O III}] \lambda \lambda 4959, 5007 \text{ \AA}$, $\text{H}\beta$, $\text{H}\gamma$, and $\text{H}\delta$ lines), though with $\approx 20\%$ larger uncertainties.

A comparison of the two data sets show the optical velocities to be systematically smaller by $\approx 80 \text{ km s}^{-1}$ at all position angles, which accounts for the different v_{sys} . The origin of such a large offset is unclear. However, Figure 10 shows that when HI and $^{12}\text{CO}(J = 2 - 1)$ peaks are strong and narrow (e.g., P10 and P11), they agree well with each other, with *both* $\approx 60 - 90 \text{ km s}^{-1}$ *higher* than FMA’s velocities. This suggests that the discrepancy between the optical and radio velocities lies in a calibration issue with FMA’s data. We also note that FMA lack velocity measurements at position angles where expansion is most pronounced (i.e., $120^\circ \leq \psi \leq 180^\circ$ and $260^\circ \leq \psi \leq 330^\circ$), which will lead to v_{exp} being underestimated. For instance, including the measured velocity from knot “k” (not used by FMA) at $\psi = 144^\circ$ increases the derived v_{exp} from 128 ± 14 to $146 \pm 16 \text{ km s}^{-1}$, which is consistent with our result. Both optical and HI kinematic studies agree that the ring rotates counter-clockwise, with the western half being the near side.

HI line profiles in AM0644-741’s ring differ substantially from the Cartwheel’s, which are typically single component and narrow ($< 50 \text{ km s}^{-1}$ FWHM; Higdon 1996). Figures 5 and 10 show that both $^{12}\text{CO}(2-1)$ and HI can possess surprisingly large velocity widths (e.g., $\Delta v_{\text{CO}} = 558 \text{ km s}^{-1}$ FWHM at P7). Figure 10 reveals a wide variety of profile shapes and widths, from narrow single components (e.g., P2, $\Delta v_{\text{HI}} = 104 \text{ km s}^{-1}$ FWHM) to wider and more complicated spectra (e.g., P13, with $\Delta v_{\text{HI}} = 261 \text{ km s}^{-1}$ FWHM and at least two $\approx 100 \text{ km s}^{-1}$ FWHM components). The former are more characteristic of profiles in the southwest ring quadrant. Where both HI and $^{12}\text{CO}(2-1)$ are detected the line profiles are similar in shape and velocity, at least for the main component (e.g., P10 and P11). It may be significant that the widest HI and CO line-widths (P7) occur at the intersection of the two $\text{H}\alpha$ rings. In terms of kinematics AM0644-741 is as rich as the Cartwheel. Whether this complicated velocity structure results from caustics in the gas or strong out-of-plane motions is not known.

The $^{12}\text{CO}(J = 2 - 1)$ lines may be broadened significantly by rotation and expansion across the $22''$ SEST beam. To estimate this effect, we modeled the 230 GHz emission as a uniform annulus with inner and outer radii of $36''$ and $48''$, respectively, with inclination, rotation and expansion speeds as derived from the above kinematic analysis. We then convolved the model to the angular and spectral resolution of our SEST observations and derived corrections to Δv_{CO} (e.g., $\approx 200 \text{ km s}^{-1}$ near the minor axis from rotation, decreasing to $\approx 50 \text{ km s}^{-1}$ near the major axis), which we subtract in quadrature to derive Δv_{corr} (Table 4). We find that the smearing of the velocity field is significant but not dominant. In particular, it is not responsible for the large $^{12}\text{CO}(J = 2 - 1)$ line widths at P7 ($\Delta v_{\text{CO,corr}} = 542 \text{ km s}^{-1}$) or P6 ($\Delta v_{\text{CO,corr}} = 213 \text{ km s}^{-1}$). Our model predicts wider $^{12}\text{CO}(J = 2 - 1)$ line-widths than we observe for P10, $\Delta v_{\text{CO,model}} = 90 \text{ km s}^{-1}$ FWHM versus the observed $\Delta v_{\text{CO}} = 55 \text{ km s}^{-1}$ FWHM. This may be due to an underestimation of the width in the relatively weak

230 GHz line at this position or a breakdown in our assumption of a uniform molecular ring. The broadening of the HI lines, estimated by the same method, is smaller because of the smaller beam size, e.g., $\approx 100 \text{ km s}^{-1}$ near the major axis to about the channel width near the major axis.

For a roughly constant v_{exp} , the collision responsible for AM0644-741’s ring occurred $\approx rv_{\text{exp}}^{-1} = 133 \text{ Myr}$ in the past. Under the same assumption, the Cartwheel and its intruder collided $\approx 400 \text{ Myr}$ ago. We derive a dynamical mass $M_{\text{ind}} = (rv_{\text{circ}}^2/G) \approx 6 \times 10^{11} M_{\odot}$, which is comparable to the Cartwheel’s (Higdon 1996). This is an approximate value since the ring is not likely to be in dynamical equilibrium. AM0644-741 appears to be a considerably younger system than the Cartwheel despite comparable linear diameter and total mass.

As another illustration of AM0644-741’s unusually large velocity range, we show its total HI spectrum in Figure 11, obtained by integrating the *robust* weighted data cube over the optical extent of the galaxy. We measure a FWZI velocity width of $743 \pm 28 \text{ km s}^{-1}$, with no correction for inclination. This range is extremely large, and is nearly twice the Cartwheel’s (Higdon 1996; Mebold et al. 1977). The profile itself is noticeably asymmetric, reflecting the concentration of HI in the southwest and southeastern ring quadrants, with at least three peaks. By comparison, the Cartwheel’s integrated HI spectrum shows a symmetric two-horned profile.

3.5. The Efficiency of Star Formation in the Ring

We follow Young et al. (1996) in parameterizing star formation efficiency, the yield of massive stars per unit H_2 mass, as $\text{SFE} = \log(L_{\text{H}\alpha}/M_{\text{H}_2})$, with $L_{\text{H}\alpha}$ and M_{H_2} in solar units. citetrownd derive global and spatially resolved SFEs for 122 normal and interacting disk galaxies, and find little variation in mean SFE from Hubble types S0 to Scd, with $\text{SFE} \approx -1.8 \pm 0.2$. Later Hubble types showed progressively higher efficiencies, with mean $\text{SFE} = -1.3 \pm 0.2$ and -0.8 ± 0.4 for Sd-Sm and Irr respectively. SFE in strongly interacting and merging systems was ≈ 4 times larger than in isolated spirals, a result in agreement with earlier estimates using CO and *FIR* data (e.g., Solomon & Sage 1988). To draw a direct comparison with their large galaxy sample, AM0644-741’s $L_{\text{H}\alpha}$ was only corrected for Galactic extinction, and we scaled M_{H_2} upward by 20% to match their larger X_{CO} (Bloemen et al. 1986). Likewise, we did not factor in a helium contribution to the molecular mass (J. Young, private communication). We find AM0644-741’s global $\text{SFE} = -1.53 \pm 0.07$, i.e., comparable to an Sd-Sm spiral. If the galaxy was originally an early spiral, as suggested by its prominent bulge, this implies an increase in SFE by a factor of ≈ 2.5 as a result of the collision, which is quite modest.

The 14 individual SFE measurements in the ring are compared with the ensemble of spatially resolved SFEs from Rownd & Young’s galaxy sample in Figure 12. The overall distribution reflects the modest increase in SFE. The total range in measured SFEs around the ring, $\Delta\text{SFE} = 1.49$, is exceptional. Most of the galaxies in Rownd & Young’s sample possess $\Delta\text{SFE} < 0.48$, i.e., a factor of ≈ 3 , and only two galaxies in their sample show a SFE dispersion wider than AM0644-741’s. Rownd & Young’s data show an abrupt decrease in the ΔSFE within individual galaxies once the *FCRAO* beam exceeds 6 kpc in linear resolution ($\Delta\text{SFE} < 0.8$ or a factor of 6) with little change in SFE, consistent with the smoothing out of SFE variations for larger areas. The large ΔSFE in AM0644-741’s ring is therefore even more notable given the ≈ 10 kpc linear resolution of the 230 GHz SEST beam.

SFE shows considerable point to point variation within the two ring quadrants where ^{12}CO is detected (Figure 13). Still, SFE is on average 4 times higher in the starburst southwest quadrant (mean $\text{SFE}_{\text{north}} = -1.72$ vs. $\text{SFE}_{\text{southwest}} = -1.07$). SFE in AM0644-741 peaks at P10, where Σ_{HI} and $\Sigma_{\text{H}\alpha}$ also reach maximum values. High SFEs limits are also indicated at P1, P2, P8, P9, P13 and P14.

Star formation efficiency might be expected to depend on the surface density of atomic plus molecular gas or stars if either provide a measure of orbit crowding in the ring, analogous to the density wave amplitude in a spiral arm. We find no correlation between $\log(L_{\text{H}\alpha}/M_{\text{H}_2})$ and $\Sigma_{\text{HI}+\text{H}_2}$ or Σ_* ; the Pearson correlation coefficient r is ≈ 0.1 in both cases).

3.6. The Star Formation Law in AM0644-741’s Ring

The strong correlation between SFR density (Σ_{SFR}) and gas surface density in spiral galaxies is well established, and is observed to hold for disks and nuclear starburst regions as a whole, as well as in spatially resolved star-forming complexes in nearby galaxies (e.g., Kennicutt 1998b, K07). This corresponds to a range of scale sizes from $\sim 0.5 - 10$ ’s of kiloparsecs and gas surface densities from $\lesssim 10$ to $10^5 M_{\odot} \text{ pc}^{-2}$. This correlation, usually referred to as the Schmidt law (Schmidt 1959), can be expressed $\Sigma_{\text{SFR}} = A \Sigma_{\text{gas}}^N$. For Σ_{SFR} in units of $M_{\odot} \text{ yr}^{-1} \text{ kpc}^{-2}$ and Σ_{gas} (atomic, molecular, or both) in $M_{\odot} \text{ pc}^{-2}$, $N \approx 1.4$.¹² The physical processes underlying the Schmidt law are of considerable interest, as is its utility as a recipe for star formation in numerical models of galaxy evolution (e.g., Richard et al. 2010) and interacting systems, including ring galaxies (e.g., Weil & Hernquist 1993; Antunes & Wallin 2007).

¹²Note that a Schmidt law with $N \approx 1.5$ is to be expected from a disk of self-gravitating clouds with volume density n_{gas} that collapse and form stars on a free-fall timescale, i.e., $\Sigma_{\text{SFR}} \sim n_{\text{gas}}/t_{\text{ff}} \sim n_{\text{gas}}/n_{\text{gas}}^{-0.5} \sim n_{\text{gas}}^{1.5}$.

The star formation law in the grand design spiral M51a was studied in detail by K07 using extinction corrected $H\alpha$ luminosities and interferometrically derived HI and H_2 surface densities (≈ 500 pc linear resolution). They find Σ_{SFR} and $\Sigma_{\text{HI}+\text{H}_2}$ to be well correlated ($r = 0.74$), obeying

$$\log \Sigma_{\text{SFR}} = (1.56 \pm 0.04) \log \Sigma_{\text{HI}+\text{H}_2} - (4.32 \pm 0.09). \quad (12)$$

M51a has large amplitude spiral arms that are especially rich in molecular gas, which follows a similar Schmidt law by itself ($r = 0.73$), though with a significantly smaller exponent,

$$\log \Sigma_{\text{SFR}} = (1.37 \pm 0.05) \log \Sigma_{\text{H}_2} - (4.36 \pm 0.09). \quad (13)$$

The scatter in both star formation laws (≈ 0.4 dex) is substantially larger than the individual measurement errors and the quoted uncertainties refer to the fit. The physical origin of this dispersion has yet to be firmly identified, though candidates include local variations in SFE, X_{CO} , and age distribution of the individual star-forming regions. Given the similarities in Schmidt law parameters calculated for different linear resolutions (including M51a), K07 conclude that the power-law exponent and zero-point are relatively insensitive to resolution. We will use these results as a benchmark for AM0644-741.

The top panel of Figure 14 shows $\log \Sigma_{\text{SFR}}$ plotted against $\log \Sigma_{\text{HI}+\text{H}_2}$ for the 14 SEST ring positions. To be consistent with K07, SFR density is calculated using the extinction corrected $H\alpha$ luminosities with no helium correction for the neutral gas. While we find Σ_{SFR} and total hydrogen surface density to be well correlated ($r = 0.63$), a bivariate least-squares fit (York et al. 2004) yields significantly different Schmidt law coefficients,

$$\log \Sigma_{\text{SFR}} = (1.29 \pm 0.06) \log \Sigma_{\text{HI}+\text{H}_2} - (3.67 \pm 0.16). \quad (14)$$

This fit is shown as a solid line in the figure, with M51a’s Schmidt law from Equation (12) shown as a dashed line for comparison. Again, the scatter is substantially larger than the individual measurement uncertainties, though formally smaller (≈ 0.2 dex) than that in M51a (K07).

The star formation laws for atomic and molecular hydrogen are shown separately in the bottom panel of Figure 14. AM0644-741’s Σ_{SFR} is also well correlated with Σ_{HI} ($r = 0.63$), but the relationship is essentially linear,

$$\log \Sigma_{\text{SFR}} = (0.96 \pm 0.04) \log \Sigma_{\text{HI}} - (3.06 \pm 0.28). \quad (15)$$

The real surprise is that Σ_{SFR} and Σ_{H_2} appear completely uncorrelated (ignoring the H_2 limits, they are actually weakly *anti-correlated*: $r = -0.5$). This figure should be compared with Figure 5 in K07 where the situation is completely reversed: in M51a Σ_{H_2} correlates

strongly with the Σ_{SFR} while it is Σ_{HI} that is uncorrelated. Given the distributions of gas and massive stars in Figures 7 and 8, this result probably should not have been unexpected. Nevertheless, it is striking to see cold molecular gas, the star-forming component of the ISM, appear so disconnected from the process in the ring.

3.7. Gravitational Stability and Star Formation

Groups of regularly spaced HII complexes are visible in the H α ring in Figure 1, with typical separations of 5 – 6 kpc. This morphology, reminiscent of “beads on a string”, is also frequently observed in spiral arms, tidal tails, nuclear starburst rings, and other ring galaxies (e.g., Elmegreen & Elmegreen 1983; Higdon 1996; Mullan et al. 2011), and is generally taken to indicate star formation triggered through the action of large scale gravitational instabilities. In this section we use the kinematics and distribution of stellar, HI, and H₂ mass to estimate the stability of AM0644-741’s ring.

A thin gaseous disk becomes gravitationally unstable wherever the Q parameter, defined

$$Q = \frac{\sigma_{\text{gas}} \kappa}{\pi G \Sigma_{\text{gas}}} \quad (16)$$

is less than unity (Safronov 1960; Toomre 1964). Here σ_{gas} and Σ_{gas} are the gas disk’s velocity dispersion and (atomic plus molecular) surface density, respectively, and κ is the disk’s epicyclic frequency, defined

$$\kappa = \sqrt{2} \frac{v_{\text{circ}}}{r} \left(1 + \frac{d \ln v_{\text{circ}}}{d \ln r} \right)^{1/2}. \quad (17)$$

For flat rotation curves the epicyclic frequency simplifies to $\kappa \approx \sqrt{2} v_{\text{circ}} r^{-1}$. Since κ , σ_{gas} , and Σ_{gas} can vary substantially over a galaxy’s disk, Q will as well. When the above local condition is satisfied, i.e., $Q < 1$, regions of the gas disk with scale size $\lambda_J \approx \sigma_{\text{gas}}^2 / (\pi G \Sigma_{\text{gas}})$ become susceptible to gravitational collapse, and proceed to form molecular cloud complexes with typical $M \approx \pi \sigma_{\text{gas}}^4 / (G^2 \Sigma_{\text{gas}})$.¹³ These in turn become the sites of star formation. Observationally, $Q \approx 1 - 2$ throughout the disks of spiral galaxies, which is attributed to negative feedback from star formation acting to both increase σ_{gas} and decrease Σ_{gas} .

Kennicutt (1989) applied these ideas to a sample of spiral galaxies and showed that the radial distribution of massive star formation, as traced by H α emission, could be understood

¹³At the Sun’s position in the Galaxy, $\sigma_{\text{gas}} \approx 5 \text{ km s}^{-1}$, $\Sigma_{\text{gas}} \approx 10 M_{\odot} \text{ pc}^{-2}$, and $\kappa \approx 1.2 \times 10^{-15} \text{ Hz}$ (Sanders et al. 1984; Kerr & Lynden-Bell 1986), giving local values of $\lambda_J \approx 200 \text{ pc}$ and $M \approx 10^7 M_{\odot}$.

in terms of a gravitational stability condition in the gas disks through a critical gas surface density Σ_{crit} defined as

$$\Sigma_{\text{crit}} = \frac{\beta \sigma_{\text{gas}} \kappa}{3.36G}, \quad (18)$$

where β was determined empirically to be 0.7 ± 0.2 . These two formulations are equivalent since $\Sigma_{\text{crit}} \propto Q \Sigma_{\text{gas}}$. Sub-critical regions (i.e., $Q < 1$) experience robust massive star formation and obey a classic (i.e., $N \approx 1.4$) Schmidt law. Conversely, star formation is greatly suppressed in regions where Q substantially exceeds unity, even if the local gas surface density is high. $Q \approx 1$ identifies a critical state where additional factors like SNe shocks, magnetic field strength, and cloud-cloud collisions can tip the scales one way or the other.

We calculate Q for gas only (Q_{gas}) at the 14 ring positions observed with the SEST using the above equations. σ_{gas} is approximated by the observed line FWHM (corrected for velocity smearing within the 230 GHz beam) divided by 2.35, even though the line profiles are typically non-gaussian, and regardless of the presence of multiple velocity components. Both HI and H₂ are included in Q_{gas} and are scaled by 1.36 to account for helium. We assume a flat rotation curve and calculate κ using the ring’s radius and v_{cir} . The derived Q_{gas} are listed in Table 6 and plotted as a function of position angle in Figure 15. AM0644-741’s gas ring is decidedly *stable* gravitationally ($Q_{\text{gas}} \approx 2 - 7$), apart from P9-11 in the starburst southwest quadrant where $Q_{\text{gas}} = 0.3 - 0.5$. This is primarily due to the ring’s typically large σ_{gas} . However, this ignores the contribution of stars to the ring’s gravitational stability. Wang & Silk (1994) find that for a stellar component with surface density Σ_* and velocity dispersion σ_* , a combined Q parameter incorporating stars and gas can be written to good approximation as

$$Q_{\text{tot}} = \frac{\kappa}{\pi G} \left(\frac{\Sigma_{\text{gas}}}{\sigma_{\text{gas}}} + \frac{\Sigma_*}{\sigma_*} \right)^{-1}. \quad (19)$$

Leroy et al. (2008) find that the additional self-gravity provided by stars can transform otherwise stable disks ($Q_{\text{gas}} > 2$) into critical or marginally stable ones ($Q_{\text{tot}} \approx 1-2$). Locally, $Q_{\text{gas}} \approx 2$ for the Σ_{gas} and σ_{gas} given in McKee (1990) and Sanders et al. (1984). When the local stellar component ($\Sigma_* \approx 35 M_{\odot} \text{ pc}^{-2}$ and $\sigma_* \approx 45 \text{ km s}^{-1}$; Kuijken & Gilmore (1989) and Wielen (1977) respectively) is included, Equation (19) gives $Q_{\text{tot}} = 1.3$. The stellar component can thus significantly affect gravitational stability.

We calculate Q_{tot} for AM0644-741’s ring using the Σ_* derived in Section 3.2. We have, unfortunately, no direct measure of σ_* , the ring’s stellar velocity dispersion. A constraint on the radial component σ_* can be inferred from the narrow width of the H α ring, since B5 stars, the longest lived massive star capable of powering luminous HII regions, will travel $d \approx \sigma_* \times \tau_{\text{B5}}$. For the observed width of the H α ring ($5'' - 8'' = 2 - 3.5 \text{ kpc}$) and the main-sequence lifetime of a B5 star (40 Myr), $\sigma_* \approx 50 \text{ km s}^{-1}$. Comparable values are found in

spiral disks (e.g., Beltran et al. 2001) as well as the solar neighborhood (Wielen 1977). At the same time, it is difficult to reconcile such σ_* with the significantly larger σ_{gas} implied by the HI and CO line profiles and the heating of the stellar disk that must have taken place during the collision. Given this inherent uncertainty, we evaluate Q_{tot} using $\sigma_* = 50 \text{ km s}^{-1}$ and $\sigma_* = \sigma_{\text{gas}}$ to bracket the correct value. The resulting azimuthal dependence of Q_{tot} is shown in Figure 15, with the hatched region reflecting σ_* ’s expected range. The stellar component has significantly lowered Q , but still not to the point that the entire ring is sub-critical. $Q_{\text{tot}} < 1$ for only four positions, P9-12, which encompass the ring’s starburst southwest quadrant. However, over the remainder of the ring $Q_{\text{tot}} \approx 1.5 - 3$, including locations where Σ_{SFR} is high, such as P1, P3, and P5. We are thus led to the unexpected conclusion that unless $\sigma_* < 50 \text{ km s}^{-1}$, AM0644-741’s star-forming ring is mostly stable against the growth of large scale density perturbations, despite indications that gravitational instabilities play a primary role in triggering star formation.

4. Discussion

4.1. Why is the Ring Rich in HI yet So Poor in H₂?

Given AM0644-741’s prominent bulge, both in terms of linear size and fraction of the galaxy’s 4.5 μm emission, and the Hubble types of its companions, it was likely an early-type spiral prior to the collision. This makes the low molecular content of its ring that more surprising, since the global f_{mol} for Sa-Sb spirals is ≈ 0.6 (Young et al. 1996). Just as striking, the inferred H₂ mass for this large galaxy is only ≈ 7 times larger than a Magellanic dwarf (Leroy et al. 2005). In trying to account for the ring’s relatively small M_{H_2} and f_{mol} we discount the possibility that we are viewing AM0644-741 at a special time, e.g., when star formation has exhausted the ring’s molecular reservoir. The ring is rich in atomic gas, and the timescale to convert HI into H₂ can be as short as $\approx 2 \text{ Myr}$ in spiral arms (e.g., Hidaka & Sofue 2002). Given the ring’s large Σ_{gas} and \gtrsim solar metallicity, HI should be quickly (and continuously) transformed into H₂. Likewise, metallicity variations cannot be the cause, since the spectra in Figure 3 indicate essentially constant abundances throughout the ring’s western half, over which f_{mol} varies by nearly an order of magnitude. Clearly, other factors are at work. We consider below the likelihood that insufficient ISM pressure, possibly in concert with high FUV radiation fields, are responsible for the observed global f_{mol} and its variations.

4.1.1. *Insufficient ISM Pressure*

The gas phase pressure (P_{ISM}) strongly influences the rate at which HI is converted to H_2 , since this process scales with the gas volume density as n_{gas}^2 , and $n_{\text{gas}} \approx P_{\text{ISM}} \sigma_{\text{gas}}^{-2}$. In a spiral disk, the mid-plane gas pressure depends on both the mass density of stars and gas as well as the respective velocity dispersions,

$$P_{\text{ISM}} \approx (\pi G / 2k_B) (\Sigma_{\text{gas}}^2 + \frac{\sigma_{\text{gas}}}{\sigma_*} \Sigma_{\text{gas}} \Sigma_*), \quad (20)$$

where k_B is the Boltzmann constant, giving units of K cm^{-3} (Elmegreen 1993). The ISM pressure may in fact be the single most important parameter determining whether molecular or atomic gas dominates the ISM in the disks of spiral galaxies (Blitz & Rosolowsky 2006). Elmegreen (1993) argued that the molecular fraction is a function of both P_{ISM} and the ambient FUV radiation field (χ_{UV}). We call this parameter ϕ_{mol} , which for solar abundances is

$$\phi_{\text{mol}} \approx (P_{\text{ISM}} / P_{\odot})^{2.2} (\chi_{\text{UV}} / \chi_{\odot})^{-1}, \quad (21)$$

where the local ISM pressure (P_{\odot}) is 10^4 K cm^{-3} and the local interstellar UV radiation field intensity (χ_{\odot}) is $2.0 \times 10^{-4} \text{ erg s}^{-1} \text{ cm}^{-2} \text{ sr}^{-1}$ (Madden et al. 1997). When ϕ_{mol} approaches or exceeds unity, $f_{\text{mol}} = 1$. Hidaka & Sofue (2002) successfully modeled the abrupt HI to H_2 transition in M51a’s disk and spiral arms using this criterion. To test the hypothesis that AM0644-741’s molecular content is primarily determined by the ISM pressure, we calculate P_{ISM} using Σ_{HI} , Σ_{H_2} , Σ_* , and velocity data in Tables 5 and 6, and compare it with the observed f_{mol} . In doing so we implicitly assume that the relationships expressed in the above two equations are valid in AM0644-741’s ring.

We use Equation (20) to calculate the ISM pressure in each of the 14 ring positions observed with the SEST. As we did for Q_{tot} , we bracket σ_* with 50 km s^{-1} and σ_{gas} . The top panel in Figure 16 shows that $P_{\text{ISM}} \approx 6 - 80 P_{\odot}$ everywhere in the outer ring regardless of σ_* . P_{ISM} is high where f_{mol} is small, and actually peaks in the southwest quadrant where the measured f_{mol} reaches a minimum. The lack of correspondence between azimuthal variations of P_{ISM} and f_{mol} is compelling evidence that pressure is not the primary factor determining the ring’s molecular content. If it were, the entire ring, and in particular, the southwest quadrant, would be dominated by H_2 .

4.1.2. *Photodissociation of Molecular Gas*

Whether the ISM is largely atomic or molecular depends on the eventual equilibrium between the formation of H_2 out of HI on dust grains and its destruction by ultraviolet

photons with wavelengths between 0.05 and 0.22 μm . Can the ambient FUV radiation field intensity (and variations) explain the relatively H_2 poor ring, or for that matter, the H_2 dominated northern quadrant? We estimate χ_{UV} in a two step process. First, we calculate the ring’s integrated 40 – 500 μm luminosity, $L_{\text{FIR,tot}} = 2.02 \times 10^{12}(2.58L'_{60\mu\text{m}} + L'_{100\mu\text{m}})$, using data tabulated in the *IRAS* Point Source Catalog (Moshir et al. 1990). At 24 and 70 μm the nucleus contributes $< 5\%$ of the total emission (Figure 2), so we assign all of the *IRAS* flux to the ring. Second, we assume that L_{FIR} is traced reasonably well by the 70 μm image, such that within each of the 14 SEST positions, $L_{\text{FIR}}(i) = (L_{\text{FIR,tot}}/F_{70\mu\text{m,tot}})F_{70\mu\text{m}}(i)$. We then follow Stacey et al. (1991) and calculate the ambient FUV radiation field at each position in units of χ_{\odot} with

$$\chi_{\text{UV}}(i) = \frac{L_{\text{FIR}}(i)}{4\pi D_{\text{L}}^2 \Delta\Omega (2.0 \times 10^{-4})}, \quad (22)$$

where D_{L} is the luminosity distance (96.9 Mpc), $\Delta\Omega$ is the source solid angle, (4.66×10^{-9} sr). These are listed in Table 7. The ring’s FUV radiation field is moderate in strength ($\chi_{\text{UV}}/\chi_{\odot} \approx 7 - 25$, peaking in the southwest quadrant) and much less extreme than a typical nuclear starburst, where $\chi_{\text{UV}}/\chi_{\odot} \approx 10^2 - 10^4$ is typical (Stacey et al. 1991).

Values of ϕ_{mol} derived using Equation (21) are shown in the bottom panel of Figure 16. We find $\phi_{\text{mol}} \gg 1$ everywhere in AM0644-741’s ring (σ_* again has a relatively small effect). This is especially true in the starburst southwest quadrant, where $\phi_{\text{mol}} \approx 25 - 1200$. Clearly, by this criterion the ring should be primarily molecular in composition. Only if $\chi_{\text{UV}}/\chi_{\odot}$ were 50 – 1000 larger would we recover the observed f_{mol} (Figure 8). Again, other factors must ultimately be determining f_{mol} .

As an alternative to the semi-analytic approach of Elmegreen, we consider the photodissociation region (PDR) models in Kaufman et al. (1999). These take a simple 1-dimensional semi-infinite slab of gas with constant volume density of hydrogen ($n = n_{\text{HI}} + 2n_{\text{H}_2}$) and gas to dust ratio, and irradiate one side with a constant (one-dimensional) flux of FUV photons ($h\nu = 6 - 13.6$ eV). Depending on n and ambient FUV radiation field G_{\odot} ($\equiv 1.71\chi_{\text{UV}}/\chi_{\odot}$), the models yield HI column density (N_{HI}) and $^{12}\text{CO}(J = 1 - 0)$ intensity (I_{CO}). For high n and weak G_{\odot} , HI is produced via photodissociation in relatively small amounts as a thin layer on the molecular cloud surface, giving low N_{HI} and high I_{CO} . At lower volume densities and higher G_{\odot} , the FUV photons penetrate deeper into the cloud, destroying CO molecules and producing more HI by photodissociation, which gives rise to higher N_{HI} and lower I_{CO} . Given G_{\odot} and N_{HI} , n can be inferred to constrain the ISM’s state.

We compare the ring’s N_{HI} and G_{\odot} with the PDR model grid shown in Figure 3 of Allen et al. (2004). Throughout the northern ring quadrant (P2-7) where $G_{\odot} \approx 10$ and $N_{\text{HI}} \approx 10^{21} \text{ cm}^{-2}$, the models give $n \approx 100 - 300 \text{ cm}^{-3}$. This is characteristic of the

cold neutral medium (CNM; $T \approx 50 - 100$ K), which makes up a large fraction of the ISM in ordinary spirals (Madden et al. 1997). The CNM is generally considered to be the precursor of cold molecular clouds and cloud complexes. In M33, for example, this component comprises roughly 50% of the neutral atomic ISM (Braun & Thilker 2004). The situation is very different in the southwest quadrant, where the higher FUV radiation field ($G_o = 15 - 25$) and HI column densities ($N_{\text{HI}} \gtrsim 10^{22} \text{ cm}^{-2}$) imply $n \approx 1 - 5 \text{ cm}^{-3}$. This density range is characteristic of the warm neutral medium (WNM; $T = 5000 - 10,000$ K). Intermediate n are found outside the northern and southwest ring quadrants (Table 7). While the implied n are ensemble averages, it nevertheless appears that the ISM in the southwest ring quadrant is highly deficient in cold dense gas, even compared with the ring’s northern half.

This raises the obvious question of how can AM0644-741’s ring sustain the observed high Σ_{SFR} in an ISM dominated by the WNM? One possibility is that most of the HI in the southwest quadrant is not directly participating in star formation, and for all practical purposes, *is* the WNM. Suppose 75% of the HI is a photodissociation product that simply “hangs around” because it is confined to the ring. If only $\approx 25\%$ of the N_{HI} is really appropriate for the PDR models, then the same range of G_o gives $n \approx 20 - 80 \text{ cm}^{-3}$, which is still low for the CNM. If 90% of the observed HI in the ring’s southwest quadrant is a photodissociated *background* component, then $n \gtrsim 100 \text{ cm}^{-3}$, and the star-forming ISM begins to more closely resemble the CNM. If so, this leaves the highly unusual situation where most of the ISM in AM0644-741’s ring *traces* rather than *sustains* star formation. How is this possible?

4.2. The Star-forming Environment in AM0644-741’s Ring

AM0644-741 presents a number of puzzles. Despite physical conditions that clearly favor the dominance of molecular over atomic gas (e.g., \gtrsim solar metallicity, large P_{ISM} , and only moderate χ_{UV}), three-quarters of the ring is characterized by low f_{mol} . Only in the northern quadrant does atomic and molecular gas appear on equal footing. Σ_{HI} in the starburst southwest quadrant, moreover, is far in excess of what is observed in spiral arms and dwarf galaxies, and is in fact WNM-like in terms of n . How can such an ISM support efficient and robust star formation? The galaxy’s star formation law, in which Σ_{SFR} appears coupled with HI but not H_2 , is highly peculiar. And finally, despite indications of gravitational instabilities operating on large scales, we find the ring to be largely stable (or at best critical) even after including the stellar mass (i.e., $Q_{\text{tot}} \approx 1.3 - 5$ for plausible values of σ_*). We propose that all of these peculiarities are a direct consequence of the ISM’s unusually long confinement time in the star-forming ring, which greatly increases its exposure to the destructive effects

of massive stars.

We illustrate schematically in Figure 17 the differences between the “over-cooked” ISM within the ring of a large and evolved ring galaxy like AM0644-741 and a spiral arm. Unlike the situation in a spiral galaxy, where a giant molecular cloud (GMC) may spend ≈ 15 Myr passing through an arm, and not encountering another arm for ≈ 100 Myr (e.g., Kim et al. 2010), GMCs in AM0644-741 and the Cartwheel are confined to the dense star-forming rings for $\gtrsim 100 - 300$ Myr. GMCs in both environments are disrupted after ≈ 10 Myr, primarily due to expanding HII regions powered by the young massive stars embedded within them (Bally & Scoville 1980; Maddalena & Morris 1987), since recent work implies that most of the damage occurs before the first supernovae (e.g., Murray et al. 2010). Unlike their spiral arm counterparts, GMCs confined within the star-forming rings accrue still further damage from the moderately high χ_{UV} as well as shocks as the OB stars proceed to supernova and deposit still more energy into the ISM. Enhanced cloud-cloud collisions in the crowded rings are an additional source of damage (e.g., Appleton & Struck 1987). With $\gtrsim 90\%$ of AM0644-741’s atomic and molecular ISM collected in the ring (Figure 4 and 5), molecular cloud fragments do not coalesce to re-form GMCs in a low χ_{UV} environment: the Oort cycle (Oort 1954) has been essentially short-circuited. As these destructive effects accumulate, the ring ISM evolves into a mixture dominated by GMC-fragments and photodissociated HI, with embedded massive stars and SNe remnants. An equilibrium is eventually reached where GMC growth in the gas rich ring is balanced by their destruction. The balance will depend on the ring’s χ_{UV} , Σ_{gas} , metallicity, and age (i.e., the confinement time).

For the moderate χ_{UV} we infer in AM0644-741’s ring, CO is expected to survive only in the innermost cloud cores where dust columns are the highest (e.g., Maloney & Black 1988). In an “over-cooked” ISM that is dominated by small H_2 clouds and GMC fragments, little CO may exist at all. As a result, ^{12}CO emission will substantially underestimate H_2 in the ring, particularly where Σ_{SFR} is high. This provides a simple explanation for the ring’s apparent low f_{mol} and M_{H_2} , as well as the anti-correlation between f_{mol} and $\Sigma_{\text{H}\alpha}$ in Figure 8. Similarly, if the ^{12}CO lines are significantly underestimating the H_2 mass, then $\log(L_{\text{H}\alpha}/M_{\text{H}_2})$ will *overestimate* SFE, particularly where Σ_{SFR} is high, accounting for the observed wide SFE range. If the underlying $I_{\text{CO}} - N_{\text{H}_2}$ relation is a function of the local Σ_{SFR} , the correlation between Σ_{H_2} and Σ_{SFR} would be expected to break down as well, giving rise to the peculiar star formation law in Figure 14.

In the Oort cycle, molecular clouds are photodissociated by embedded OB stars downstream from the arm (Figure 17 upper panel). Such offsets between ^{12}CO and HI emission are observed in galaxies with large amplitude spiral arms like M51 (e.g., Vogel et al. 1988). For AM0644-741’s “over-cooked” ring, moderately high χ_{UV} combined with fragmented clouds

will produce a large photodissociated HI component, giving rise to unusually high Σ_{HI} . This process should scale with the local Σ_{SFR} , accounting for the observed linear relation between Σ_{HI} and $\Sigma_{\text{H}\alpha}$ in Figure 14. Photodissociation of cloud fragments would be expected to produce low volume density HI, and account for the dominant WNM-like ISM in the ring’s southwest quadrant. The low volume density of photodissociated HI will retard the conversion back to H_2 and contribute to the large Σ_{HI} and low f_{mol} despite the high P_{ISM} . This provides a simple explanation for the observed variations in f_{mol} around the ring in Figure 8. In the southwest quadrant, ^{12}CO emission is suppressed due to small cloud sizes and peak χ_{UV} , while photodissociated HI is produced in abundance. f_{mol} will appear small as a result. The opposite situation exists in the northern ring quadrant (P3-7), where Σ_{SFR} and χ_{UV} are lower and fragmentation should be less severe. Consequently, ^{12}CO emission will better trace H_2 and photodissociated HI will exist in smaller proportions, accounting for the observed $f_{\text{mol}} \approx 0.5$.

We have argued that ^{12}CO emission will substantially underestimate the ring’s molecular mass. But by how much? Suppose that the molecular ISM obeyed M51’s Schmidt law (K07). We can rewrite Equation (13) to estimate Σ_{H_2} directly from the observed Σ_{SFR} , i.e., $\Sigma_{\text{H}_2} = 1522 \Sigma_{\text{SFR}}^{0.72}$. The predicted Σ_{H_2} are $\approx 3 - 20\times$ higher than what we infer from ^{12}CO in the northern quadrant. In the southwest quadrant however the discrepancy is much greater, with the predicted $\Sigma_{\text{H}_2} \approx 150 - 250 M_{\odot} \text{ pc}^{-2}$, implying that H_2 is underestimated by factors of $\approx 10 - 20$. The overall effect on the ring’s molecular fraction is dramatic: $f_{\text{mol}} \approx 0.7 - 0.9$ around the ring. The resulting Q from such a modification is shown in Figure 18, where the ring becomes mostly sub-critical, even when gas alone is considered. $Q_{\text{tot}} < 1$ everywhere except for P7 and P14, where little star formation occurs. Regions of high Σ_{SFR} that are not detected in ^{12}CO emission are now sub-critical. We emphasize that while this thought experiment is not intended as an accurate measure of the ring’s molecular mass, it does suggest large amounts of unseen H_2 are present in AM0644-741’s ring, sufficient to render most of the ring gravitationally unstable. Alternate assays of the ring’s molecular content are clearly needed.

The above effects will be heightened in low metallicity environments such as the Cartwheel’s ring, as CO will be further hard pressed to survive the lowered dust columns, even less so in cloud fragments. However, not every ring galaxy’s ISM is expected to be “over-cooked”. Systems that are either young (i.e., $\text{Age} \approx R/v_{\text{exp}} \lesssim 30 \text{ Myr}$) or which possess low Σ_{SFR} should possess more typical n , SFE, f_{mol} , and star formation laws. Arp 147, with a $\approx 33 \text{ Myr}$ old ring ($\text{Age} = 4.5 \text{ kpc}/136 \text{ km s}^{-1}$; Jeske 1986) is an example of the former. It possesses a robustly star-forming ring, with a globally averaged Σ_{SFR} ($0.06 M_{\odot} \text{ yr}^{-1} \text{ kpc}^{-2}$) nearly identical to the Cartwheel’s and AM0644-741’s. The ring is also gas rich, with $M_{\text{HI}} = (3.80 \pm 0.05) \times 10^9 M_{\odot}$ and $M_{\text{H}_2} = 2.5 \times 10^9 M_{\odot}$ with X_{Gal} (Jeske 1986; Horellou et al. 1995), giving a more normal

average $f_{\text{mol}} = 0.4$. Other examples include NGC 2793 ($\text{SFR} \approx 0.3 M_{\odot} \text{ yr}^{-1}$; Higdon et al. 2001) and the “Sacred Mushroom” ($\text{SFR} < 0.05 M_{\odot} \text{ yr}^{-1}$ (3σ); Higdon et al. 2001). High angular resolution CO, infrared and submillimeter wave observations will be needed to test this prediction.

Are the rings of AM0644-741 and the Cartwheel unique star-forming environments, or do analogs exist in other systems? Nuclear starburst rings, resulting from bar induced resonances, would at first glance appear to be good candidates. Gas is confined to the rings for ≈ 100 Myr timescales, and they are often sites of intense star formation. Examples include NGC 1097 (Gerin et al. 1988) and NGC 4314 (Benedict et al. 1992). One might therefore expect large amounts of photodissociated HI and low n and f_{mol} . Not so. The ISM of nuclear rings appear dominated by molecular rather than atomic gas (e.g., Gerin et al. 1991; Benedict et al. 1996; Curran et al. 2008; Hsieh et al. 2008). This is likely a consequence of both the high metallicity and large Σ_{*} and Σ_{gas} in the ring and nuclear regions promoting rapid conversion of HI to H_2 , and keeping $f_{\text{mol}} \approx 1$. Polar ring galaxies, such as NGC 4650 A and NGC 660, where a close passage has apparently transferred gas and dust into a polar orbit around an S0 galaxy may be the closest analogs to ring galaxies. Polar rings appear to persist for > 100 Myr timescales, and several show high Σ_{SFR} and Σ_{HI} (e.g., Gottesman & Mahon 1990; Arnaboldi et al. 1997). These objects are still relatively unexplored observationally, and would be good targets for comparison studies at radio, millimeter, and infrared wavelengths. The rings in evolved starburst ring galaxies like AM0644-741 and the Cartwheel appear to represent rather unique star-forming environments. They also further demonstrate the hazards of trying to infer basic properties of the molecular ISM using rotational transitions of ^{12}CO where the physical conditions differ markedly from the Milky Way’s disk.

4.3. Follow-up Observations

Current and next-generation infrared and sub/millimeter wave facilities will allow the ideas outlined in the previous sections to be explored observationally.

Herschel makes available a suite of infrared emission lines that provide important diagnostics of PDR regions (e.g., [C II] $\lambda 157.7 \mu\text{m}$ and [O I] $\lambda\lambda 63.2, 145.5 \mu\text{m}$ with PACS, and [C I] $\lambda\lambda 369.9, 609.1 \mu\text{m}$ with SPIRE), which should be prominent in the rings of AM0644-741 and the Cartwheel. Just as important, an independent estimate of Σ_{H_2} can be obtained by combining MIPS $24\mu\text{m}$ and $70\mu\text{m}$ with PACS 100 and $160 \mu\text{m}$ images to estimate the optical depth of dust (τ_{dust}). When multiplied by the gas-to-dust ratio (δ), the H_2 surface density can be estimated with $\Sigma_{\text{H}_2} = \frac{1}{2}(\frac{\tau_{\text{dust}}}{\delta} - \Sigma_{\text{HI}})$ (e.g., Israel 1997; Leroy et al. 2009). δ cannot be

measured directly, but can be reasonably constrained using measured obscuration and metal abundances.

The Atacama Large Milimeter Array (ALMA) will revolutionize astronomy in the 84 – 950 GHz range due to its high angular resolution ($\lesssim 1''$), wide range of spectral resolution, and superb sensitivity. These gains are the result of the large number of array elements (> 60 12 m telescopes), state of the art receivers and correlator, and a very dry site. ALMA observations of AM0644-741 and the Cartwheel would immediately impact the question of their gravitational stability and star formation law by spatially resolving the $^{12}\text{CO}(J = 1 - 0)$ and $^{12}\text{CO}(J = 2 - 1)$ emission in the rings. This will allow the precise determination of the molecular ISM’s surface density, kinematics, and velocity dispersion, which are quantities we can only estimate with our single-dish data (particularly so in AM0644-741’s double-ringed northern quadrant).

We have invoked an “over-cooked” ISM to explain AM0644-741’s (and by inference, the Cartwheel’s) peculiar star formation law, n , SFE, and f_{mol} . The dramatically improved sensitivity and angular resolution provided by ALMA will permit the detection of individual molecular cloud complexes, allowing us to constrain their size and mass distributions. Interferometric $^{12}\text{CO}(J = 1 - 0)$ observations of spiral arms in nearby galaxies have identified discrete objects termed giant molecular associations (GMAs), with $M_{\text{H}_2} \approx 3 - 7 \times 10^7 M_{\odot}$, velocity widths of $\approx 10 \text{ km s}^{-1}$, and 300 – 450 pc diameters (e.g., Rand 1993, 1995). For a Galactic X_{CO} we would expect the H_2 mass equivalent of $\approx 100 - 5 \times 10^7 M_{\odot}$ GMAs throughout AM0644-741’s ring. Each would subtend $\approx 1''$ if similar to those in M51, and emit a 115 GHz line flux of $0.36 \text{ Jy km s}^{-1}$. This would be detected at the 5σ level in $^{12}\text{CO}(J = 1 - 0)$ in 2.5 hr per array pointing ($\approx 55''$ primary beam) with angular and velocity resolution of $0.5''$ and 2 km s^{-1} for the sensitivity estimates in Wootten & Thompson (2009). An obvious first question would be whether the molecular ISM in AM0644-741’s ring is dominated by a small number of GMAs, or by many smaller lower mass complexes. Resolved studies of molecular cloud associations in the rings of AM0644-741 and the Cartwheel will allow us to test the expectation of smaller or less massive GMAs, and make important comparisons with the size and mass distributions of GMAs in other systems (e.g., spiral arms with similar Σ_{SFR}), and how their properties vary with local conditions. Observations in higher ^{12}CO transitions will help constrain the excitation dependence of X_{CO} . Additionally, observations of other molecules that may serve as more reliable tracers of the dense star-forming ISM (e.g., ammonia or CS) can be carried out to see if the densest gas correlates with local Σ_{SFR} . In other words, can a standard Schmidt law be recovered by using CS instead of ^{12}CO ?

Recent advances in implementing a multi-phase ISM in galaxy evolution codes (e.g., Saitoh et al. 2009) additionally open the prospect of modeling the effects of confining an

otherwise normal molecular ISM to a dense star-forming ring for long timescales. Ring galaxy models with more realistic star formation recipes would be important adjuncts to observational studies, and we encourage such studies to be done.

4.4. Density Wave or “Forest Fire”?

Korchagin et al. (1998, 1999, 2001) account for radial color gradients interior to the ring and slight offsets between the $H\alpha$ and continuum rings by invoking a self-sustaining radially propagating starburst. This model dispenses with the orbit crowded ring altogether and is reminiscent of the explanation of flocculent spiral arms by Gerola & Seiden (1978). The central passage of a companion galaxy through a spiral disk is still required, but now acts as a “detonator” that initiates a nuclear starburst. Once started, the nuclear starburst self-propagates radially through the disk in a ring shaped distribution of HII complexes. The orbits of stars are left largely undisturbed, while the ISM experiences local accelerations from SNe shocks, stellar winds, and ionization fronts that trigger new star formation at larger radii. Post-starburst populations left in the wake of this rampaging “forest fire” give rise to radial color and abundance gradients on galaxy-wide scales. Korchagin et al. (1998) successfully accounted for the color gradients in the Cartwheel’s disk (Marcum et al. 1993). Such a novel (and radical) interpretation bears consideration in light of published studies of the gaseous (Higdon 1996; Higdon et al. 1997) and stellar (Appleton & Marston 1997; Higdon 1995, HW97) components of ring galaxies, including this one. Does the “forest fire” hypothesis hold up to observational scrutiny? There are in fact major problems with this interpretation.

First, a Gerola & Seiden-esque “forest fire” cannot produce the HI distributions of ring galaxies. Σ_{HI} in rings of AM0644-741 and Cartwheel greatly exceed that found in outer spiral disks. Gas must have traveled from their interiors. However, shocks and winds from star-forming regions are ill suited to produce such coherent and large scale gas outflows, even ignoring inhomogeneities in the disk (e.g., spiral arms and HI holes) that would work against the formation of narrow HI rings. The low Σ_{gas} encircled disks present another problem: where did all the gas go? Conversion into stars would require essentially 100% SFE on $\approx 100 - 300$ Myr timescales, which is clearly unfeasible. Second, analysis of the Cartwheel’s HI kinematics found large-scale gas inflows plus an \approx solid-body rotation curve (Higdon 1996). While the forest fire interpretation makes no clear kinematic predictions, it is not obvious how a propagating starburst would result in these bulk motions. Third, differential rotation will distort and eventually destroy the symmetry of a self-propagating starburst unless it was perfectly centered, i.e., unless the intruder passed through the exact center of the target

disk. An analogy can be made with the evolution of HI holes in spiral disks, created by expanding superbubbles of hot gas from SNe blasts (e.g., Deul & den Hartog 1990). As the holes grow they are invariably distorted by shear. One would therefore predict that large off-centered ring galaxies would have highly distorted rings. The opposite is true: the three largest ring galaxies - AM0644-741, the Cartwheel, and the “Sacred Mushroom” - all have highly symmetric rings, even the two formed in a markedly off-centered collision. If the rings are just propagating HII region fronts, one would expect that preexisting stellar structures like spiral arms and bars to survive, and in fact, made more obvious in optical images. On the contrary, apart from the Cartwheel’s spokes, no other ring galaxy shows obvious spiral arms. Finally, roughly 10% of spirals in the local universe with $9.7 \leq \log(L_{\text{FIR}}/L_{\odot}) \leq 10.7$ possess starburst nuclei, representing a space density $\rho_{\text{SB}} \approx 10^{-4} \text{ Mpc}^{-3}$ (e.g., Weedman 1983; De Robertis & Shaw 1988). This is 50-times larger than the estimated space density of ring galaxies, $\rho_{\text{RG}} \approx 2 \times 10^{-6} \text{ Mpc}^{-3}$ (Few & Madore 1986). If ring galaxies are a consequence of a nuclear starburst, then they would be expected to be much more common, even considering the transient nature of both the rings and nuclear starbursts.

The collisional interpretation has no such problems. Numerical models since the classic work of Lynds & Toomre (1976) reproduce the narrow and high Σ_{gas} rings and gas poor interiors through orbit crowding. SPH models by Struck & Higdon (1993) successfully accounted for the Cartwheel’s large-scale kinematics. Stellar structures in the disk (e.g., pre-collision spiral arms) are effectively erased as their orbits are crowded and phase mixed in the expanding ring. Ring galaxies are rare simply because they require a low probability event - a low impact-parameter collision with a companion. Stochastic effects undoubtedly play a role in these systems. However, the weight of evidence argues that they must be secondary to the ability of the ring density wave to concentrate a disk’s stellar and gaseous components into a dense environment for the action of gravitational instabilities.

5. Conclusions

Ring galaxies are unique systems in which to study the triggering and regulation of massive star formation on large scales. In this paper we examine one of the best examples, AM0644-741, which is notable for its large diameter ring (42 kpc), inferred age (133 Myr), and global SFR. From the analysis of H α , FUV, infrared, and radio continuum images we conclude that $\text{SFR} = 11 M_{\odot} \text{ yr}^{-1}$, with relatively low internal extinction ($A_{\text{H}\alpha} \approx 1$), and no significant star formation within the encircled disk or nucleus. Analysis of optical spectra show that AM0644-741’s ring possesses \gtrsim solar metal abundances (in marked contrast with its “twin” the Cartwheel), opening the possibility of characterizing its molecular ISM using

rotational transitions of ^{12}CO . The distribution of HII complexes gives the appearance of the classic “beads on a string” morphology, which is a hallmark of star formation triggered by the action of large scale gravitational instabilities. One therefore expects $Q < 1$ throughout the ring.

Observations using ATCA and SEST show that essentially all of AM0644-741’s neutral ISM is concentrated in the expanding 42 kpc diameter ring, which agrees both with collisional models and high resolution observations of other ring galaxies (e.g., Arp 143 and the Cartwheel). Contrary to our expectations, we find the ring’s global molecular fraction to be surprisingly small ($f_{\text{mol}} = 0.078 \pm 0.003$), particularly given that Sa-Sb galaxies, the likely progenitor of AM0644-741, normally possess comparable amounts of HI and H_2 . It is this apparent deficiency of H_2 that is responsible for the ring’s other peculiar properties: elevated SFE, a star formation law where atomic gas - but not molecular gas - correlates with star formation, and typically $Q_{\text{tot}} \gtrsim 1$. The concentration of the disk’s ISM into the dense ring appears to have not generated a molecular rich environment. Quite to the contrary, applying PDR models to the observed Σ_{HI} , Σ_{H_2} , and χ_{UV} yield WNM-like total hydrogen volume densities ($n \approx 2 \text{ cm}^{-3}$) throughout the ring quadrant experiencing peak SFR.

Our data allow us to reject the possibility that the ring’s apparently small molecular component is the result of low and/or variable metallicity, unusually high χ_{UV} , or insufficient pressure (which regulates the conversion of HI to H_2). We find the opposite to be true: AM0644-741’s ring would have been expected to be dominated by molecular gas given our estimates of its P_{ISM} and χ_{UV} . To explain how AM0644-741 can form stars in a WNM dominated ISM, we propose that the rings in evolved and robustly star-forming ring galaxies like AM0644-741 and the Cartwheel possess an “over-cooked” ISM, where GMCs are fragmented and photodissociated by prolonged exposure to SNe shocks, expanding HII regions, and moderately high χ_{UV} ($\approx 7 - 25\chi_{\odot}$) during their > 100 Myr confinement to the ring. Consequently, CO survives only in the small innermost cloud cores due to reduced shielding available in the cloud fragments, and traces H_2 differently than for a Galactic cloud. In particular, ^{12}CO transitions will significantly *underestimate* the amount of H_2 in the ring in a way that depends on the local SFR density. An “over-cooked” ISM can thus account for the unusually high SFE, the small f_{mol} and its variations around the ring, as well as the peculiar star formation law, where CO appears to be decoupled from local star formation. This also explains the observed linear relationship between Σ_{SFR} and Σ_{HI} : the abundant atomic gas we detect with the ATCA is primarily a photodissociation product, which traces rather than fuels star formation. It is no longer surprising, then, that this component will resemble the WNM. For all practical purposes, it is the WNM.

If, as we suspect, ^{12}CO significantly underestimates the ring’s molecular component,

then Q_{tot} may be significantly overestimated. If the H_2 obeys an M51-like Schmidt Law (e.g., K07), then we find that $Q_{\text{tot}} < 1$ is satisfied for nearly all of the ring, and in particular, where massive star formation is observed to be robust. Gravitational instabilities then become the dominant star formation trigger. Independent estimates of the ring’s molecular component, as well as better constraints on the stellar velocity dispersion, are clearly needed to conclusively settle this point.

Another peculiar aspect of AM0644-741’s ISM, and one not evident in the Cartwheel, is the wide and multi-component line profiles, both in the atomic and molecular gas. It is not clear at present if this reflects caustics in the gas flow or out-of-plane motions, though preliminary N -body simulations appear to favor the former interpretation (J. Wallin, private communication).

Our results imply that the rings of systems like AM0644-741 and the Cartwheel represent substantially different star-forming environments than that typically found in spiral arms due to the sustained accumulation of damage to the ISM from concentrated populations of OB stars. At the same time, the modest FUV radiation fields mean that they are still different from intense nuclear starbursts and ULIRGs. Ring galaxies remain interesting and valuable systems to study the interaction between the ISM and intense star formation, and follow-up observations with *Herschel* and ALMA, in addition to models incorporating more sophisticated treatments of the ISM, are clearly warranted.

Finally, we examined the “forest fire” interpretation of ring galaxies in light of these (and previous) observational results. We argue that a propagating starburst (e.g., Gerola & Seiden 1978) cannot reproduce the observed gas distribution or large-scale kinematics of ring galaxies. Likewise, the space density of nuclear starburst galaxies, i.e., systems possessing the forest fire “detonator”, is ≈ 50 times larger than that of ring galaxies, implying that if ring galaxies arise this way, they should be much more common. The collisional interpretation has no such problems.

We thank the staff of the SEST, in particular Philippe McAuliffe, for their hospitality and assistance with the observations. We also thank Michael Nord for his assistance with the CO observations. Discussions with Mark Hancock were helpful in our estimates of the ring’s stellar mass. J.L.H. also thanks the Kapteyn Astronomical Institute, especially Thijs van der Hulst, for supporting this and related research, and David McConnell of the *ATNF* for the generous allotment of telescope time. We acknowledge the anonymous referee for valuable comments and suggestions, and Jonathan Braine for alerting us to an error in our H_2 mass estimation. This research has made use of the NASA/IPAC Extra-galactic Database (NED), which is operated by the Jet Propulsion Laboratory, California Institute

of Technology, under contract with the National Aeronautics and Space Administration. J.L.H. and S.J.U.H. acknowledge support from NASA/*Spitzer* grant 1346930.

REFERENCES

- Allen, R. J., Heaton, H. I., & Kaufman, M. J. 2004, *ApJ*, 608, 314
- Antunes, A. & Wallin, J. 2007, *ApJ*, 670, 261
- Appleton, P. & Marston, A. 1997, *AJ*, 113, 201
- Appleton, P. & Struck-Marcell, C. 1987, *ApJ*, 318, 103
- Arnaboldi, M., Oosterloo, T., Combes, F., Freeman, K. C., & Koribalski, B. 1997, *AJ*, 113, 585
- Arp, H. J. & Madore, B. F. 1987, *A Catalog of Southern Peculiar Galaxies and Associations* (Cambridge: Cambridge Univ. Press)
- Bally, J. & Scoville, N. 1980, *ApJ*, 239, 121
- Bell, E. F., Phelps, S., Somerville, R., et al. 2006, *ApJ*, 652, 270
- Beltran, J. C., Pizzella, A., Corsini, E. M., et al. 2001, *A&A*, 374, 394
- Benedict, G. F., Higdon, J. L., Tollestrup, E., Hahn, J., & Harvey, P. 1992, *AJ*, 103, 757
- Benedict, G. F., Smith, B. J., & Kenney, J. 1996, *AJ*, 112, 1318
- Bessel, M. S. 1979, *PASP*, 91, 589
- Blitz, L. & Rosolowsky, E. 2006, *ApJ*, 650, 933
- Bloemen, J. G., Strong, A. W., Mayer-Hasselwander, H. A. et al. 1986, *A&A*, 154, 25
- Braine, J., Combes, F., Casoli, F. et al. 1993, *A&AS*, 97, 887
- Braun, R., & Thilker, D. A. 2004, *A&A*, 417, 421
- Caffau, E., & Ludwig, H.-G. 2008, in *IAU Symposium*, 252, *The Art of Modeling Stars in the 21st Century* (Cambridge: Cambridge Univ. Press), 35
- Calzetti, D., Kennicutt, R. C., Engelbracht, C. W., et al. 2007, *ApJ*, 666, 870

- Conselice, C. J., Bershad, M., Dickinson, M., & Papovich, C. 2003, *AJ*, 126, 1183
- Corwin, H. C., Buta, R. J., & de Vaucouleurs, G. 1994, *AJ*, 108, 2128
- Curran, S. J., Koribalski, B. S., & Bains, I. 2008, *MNRAS*, 289, 63
- Dame, T. M., Hartmann, D., & Thaddeus, P. 2001, *ApJ*, 547, 792
- De Robertis, M. M. & Shaw, R. A. 1988, *ApJ*, 329, 629
- Deul, E. R. & den Hartog, R. H. 1990, *A&A*, 229, 362
- Dickman, R. L. 1978, *ApJS*, 37, 407
- Draine, B. T. 1978, *ApJS*, 36, 595
- Dressler, A. 1980, *ApJ*, 236, 531
- Elmegreen, B. G. 1993, *ApJ*, 411, 170
- Elmegreen, B. G., & Elmegreen, D. M. 1983, *MNRAS*, 203, 31
- Engelbracht, C. W., Blaylock, M., Su, K. Y., et al., 2007, *PASP*, 119, 994
- Ferguson, H. C., Dickinson, M. & Williams, R. 2000, *ARA&A*, 38, 667
- Few, J. M. & Madore, B. F. 1986, *MNRAS*, 222, 673
- Few, J. M., Madore, B. F., & Arp, H. J. 1982, *MNRAS*, 199, 633 (FMA)
- Fosbury, R. A. E. & Hawarden, T. G. 1977, *MNRAS*, 178, 473
- Gerin, M., Casoli, F., & Combes F. 1991, *A&A*, 251, 32
- Gerin, M., Combes, F. & Nakai, N. 1988, *A&A*, 203, 44
- Gerola, H. & Seiden, P. E. 1978, *ApJ*, 223, 129
- Gordon, K. D., Rieke, G., Engelbracht, C. W., et al. 2005, *PASP*, 117, 503
- Gottesman, S. T., & Mahon, M. E. 1990, *IAU Colloquium 124, Paired and Interacting Galaxies*, 209
- Graham, J. A. 1974, *Observatory*, 94, 290
- Graham, J. A. 1982, *PASP*, 94, 244

- Heckman, T. M., Smith, E. P., Baum, S. A., et al. 1986, *ApJ*, 311, 526
- Hibbard, J. E., van der Hulst, J., Barnes, J. & Rich, R. 2001, *AJ*, 122, 2969
- Hidaka, M. & Sofue, Y. 2002, *PASJ*, 54, 223
- Higdon, J. L. 1995, *ApJ*, 455, 524
- Higdon, J. L. 1996, *ApJ*, 467, 241
- Higdon, J. L., Rand, R. J., & Lord, S. 1997, *ApJ*, 489, L133
- Higdon, J. L., & Wallin, J. F. 1997, *ApJ*, 474, 686 (HW97)
- Higdon, J. L., Wallin, J. F., Rand, R. J., & Sage, L. 2001, *Gas and Galaxy Evolution*, 240, 860
- Hopkins, A., Miller, C. J., Nichol, R. C., et al. 2003, *ApJ*, 599, 971
- Horellou, C., Casoli, F., Combes, F., & Dupraz, C. 1995, *A&A*, 298, 743
- Horellou, C., Charmandaris, V., Combes, F., et al. 1998, *A&A*, 340, L51
- Hsieh, Pei-Ying, Matsushita, S., Lim, J., Kohno, K., & Sawada-Satoh, S. 2008, *ApJ*, 683, 70
- Israel, F. P. 1997, *A&A*, 328, 471
- Jeske, N. 1986, Ph D thesis, Univ. California, Berkeley
- Jogee, S., Miller, S. H., Penner, K., et al. 2009, *ApJ*, 697, 1971
- Kaufman, M. J., Wolfire, M. G., Hollenbach, D. J. & Luhman, M. L. 1999, *ApJ*, 527, 795
- Kennicutt, R. C. 1989, *ApJ*, 344, 685
- Kennicutt, R. C. 1998a, *ARA&A*, 36, 189
- Kennicutt, R. C. 1998b, *ApJ*, 498, 541
- Kennicutt, R. C., Armus, L., Bendo, G., et al. 2003, *PASP*, 115, 928
- Kennicutt, R. C., Calzetti, D., Walter, F., et al. 2007, *ApJ*, 671, 333 (K07)
- Kennicutt, R. C., Hao, C., Calzetti, D., et al. 2009, *ApJ*, 703, 1672
- Kerr, F. J. & Lynden-Bell, D. 1986, *MNRAS*, 221, 1023

- Kim, C. G., Kim W. T., & Ostriker, E. C. 2010, *ApJ*, 720, 1454
- Komatsu, E., Smith, K. M., Dunkley, J., et al. 2011, *ApJS*, 192, 18
- Korchagin, V., Mayya, Y. & Vorobyov, E. 2001, *ApJ*, 554, 281
- Korchagin, V., Mayya, Y., Vorobyov, E., & Kembhavi, A. 1998, *ApJ*, 495, 757
- Korchagin, V., Vorobyov, E., & Mayya, Y. 1999, *ApJ*, 522, 767
- Kuijken, K. & Gilmore, G. 1989, *MNRAS*, 239, 605
- Leitherer, C., Schaerer, D., Goldader, J., et al. 1999, *ApJS*, 123, 3
- Leroy, A., Bolatto, A., Bot, C., et al. 2009, *ApJ*, 702, 352
- Leroy, A., Bolatto, A. D., Simon, J. D., & Blitz, L. 2005, *ApJ*, 625, 763
- Leroy, A., Walter, F., Brinks, E., et al. 2008, *AJ*, 136, 2782
- Lynds, R. & Toomre, A. 1976, *ApJ*, 209, 382
- Maddalena, R. J. & Morris, M. 1987, *ApJ*, 323, 179
- Madden, S. C., Poglitsch, A., Gies, N., Stacey, G., & Townes, C. 1997, *ApJ*, 483, 200
- Makovoz, D., & Marleau, F. R. 2005, *PASP*, 117, 1113
- Maloney, P. & Black, J. 1988, *ApJ*, 325, 389
- Mapelli, M., Moore, B., Ripamonti, E., et al. 2008, *MNRAS*, 383, 1223
- Marcum, P. M., Appleton, P., & Higdon, J. L. 1993, *ApJ*, 399, 57
- Marston, A. P. & Appleton, P. 1995, *AJ*, 109, 1002
- Martin, D. C., Fanson, J., Schiminovich, D., et al. 2005, *ApJ*, 619, L1
- McKee, C. F. 1990, in *ASP Conf. Ser. 12, The Evolution of the Interstellar Medium* (San Francisco, CA: ASP), 3
- Mebold, U., Goss, W., & Fosbury, R. A. E. 1977, *MNRAS*, 180, 11P
- Moore, B., Katz, N., Lake, G., Dressler, A. & Oemler, A. 1996, *Nature*, 379, 613
- Morrissey, P., Conrow, T., Barlow, T., et al. 2007, *ApJS*, 173, 682

- Morrissey, P., Schiminovich, D., Barlow, T., et al. 2005, *ApJ*, 619, 7
- Moshir, M., Kopan, G., Conrow, T., et al. 1990, *BAAS*, 22, 1325
- Mullan, B., Konstantopoulos, I., Kepley, A., et al. 2011, *ApJ*, 731, 93
- Murray, N., Quataert, E., & Thompson, T. A. 2010, *ApJ*, 709, 191
- Nagao, T., Maiolino, R., & Marconi, A. 2006, *A&A*, 459, 85
- Oort, J. H. 1954, *Bull. Astr. Institute Netherlands*, 12, 177
- Ramos Almeida, C. R., Tadhunter, C. N., Inskip, K. J., et al. 2011, *MNRAS*, 410, 1550
- Rand, R. J. 1993, *ApJ*, 404, 595
- Rand, R. J. 1995, *AJ*, 109, 2444
- Richard, S., Brook, C., Martel, H., et al. 2010, *MNRAS*, 402, 1489
- Richards, E., Fomalont, E., Kellermann, K., et al. 1999, *ApJ*, 526, L73
- Rownd, B. K. & Young, J. S. 1999, *ApJ*, 118, 670
- Safronov, V. S. 1960, *Ann. d’Astrophys.*, 23, 979
- Saitoh, R., Kaisaka, H., Kokubo, E., et al. 2009, *PASJ*, 61, 481
- Sanders, D. B., & Mirabel, I. F. 1996, *ARA&A*, 34, 749
- Sanders, D. B., Solomon, P. M., & Scoville, N. Z. 1984, *ApJ*, 276, 182
- Schmidt, M. 1959, *ApJ*, 129, 243
- Smail, I., Ivison, R. J., & Blain, A. W. 1997, *ApJ*, 490, L5
- Solomon, P. M., Rivolo, A. R., Barrett, J. & Yahil, A. 1987, *ApJ*, 319, 730
- Solomon, P. M. & Sage, L. 1988, *ApJ*, 334, 613
- Stacey, G. J., Geis, N., Genzel, R., et al. 1991, *ApJ*, 373, 423
- Strong, A. W., Bloemen, J., Dame, T., et al., 1988, *A&A*, 207, 1
- Struck, C. J. & Higdon, J. L. 1993, *ApJ*, 411, 108
- Tacconi, L. J., Genzel, R., Smail, I., et al. 2008, *ApJ*, 680, 246

- Toomre, A. 1964, *ApJ*, 139, 1217
- Toomre, A. 1974, in *IAU Symp. 58, The Formation and Dynamics of Galaxies* (Cambridge: Cambridge Univ. Press), 347
- Vazquez, G. A., & Leitherer, C. 2005, *ApJ*, 621, 695
- Vogel, S. N., Kulkarni, S. R., & Scoville, N. Z. 1988, *Nature*, 334, 402
- Wallin, J. F. & Struck, C. 1994, *ApJ*, 433, 631
- Wang, B. & Silk, J. 1994, *ApJ*, 427, 759
- Weedman, D. 1983, *ApJ*, 266, 479
- Weil, M. & Hernquist, L. 1993, *MNRAS*, 261, 804
- Werner, M. W., Roellig, T., Low, F., et al. 2004, *ApJS*, 154, 1
- White, S. D. & Rees, M. J. 1978, *MNRAS*, 183, 341
- Wielen, R. 1977, *A&A*, 60, 263
- Williams, R. E., Blacker, B., Dickinson, M., et al. 1996, *AJ*, 112, 1335
- Wilson, C. D. 1995, *ApJ*, 488, L97
- Wootten, A. & Thompson, R. 2009, *Proc. IEEE*, 99, 1463
- York, D., Evensen, N. M., Lopez Martinez, M., and De Basabe Delgado, J. 2004, *Am. J. Phys.*, 72, 367
- Young, J. S., Allen, L., Kenney, J., Lesser, A., & Rownd, B. 1996, *AJ*, 112, 1903

Table 1: AM0644-741 Global Properties

| | |
|---|---|
| R.A. ^(a) | 06 ^h 43 ^m 06. ^s 18 |
| Dec. ^(a) | -74° 14′ 10. [″] 7 |
| l, b | 285.26, -26.59 |
| v_{sys} ^(b) | $6692 \pm 8 \text{ km s}^{-1}$ |
| Luminosity distance | 96.9 Mpc |
| <i>IRAS</i> flux densities ^(c) | 0.073, 0.152, 1.41, 3.89 Jy |
| Ring diameter | $95'' \times 52''$ ($42 \times 23 \text{ kpc}$) |
| L_{IR} ^(d) | $(4.7 \pm 0.2) \times 10^{10} L_{\odot}$ |
| I_{1-0} ^(e) | $4.02 \pm 0.15 \text{ K km s}^{-1}$ |
| I_{2-1} ^(e) | $13.52 \pm 0.38 \text{ K km s}^{-1}$ |
| $R(\frac{1-0}{2-1})$ ^(f) | 0.59 ± 0.03 |
| $L_{20\text{cm}}$ ^(g) | $(3.2 \pm 0.2) \times 10^{22} \text{ W Hz}^{-1}$ |
| $L_{\text{H}\alpha}$ ^(h) | $1.43 \pm 0.06 \times 10^{42} \text{ erg s}^{-1}$ |
| SFR ⁽ⁱ⁾ | $11.0 \pm 0.4 M_{\odot} \text{ yr}^{-1}$ |
| SFE _{global} ^(j) | -1.53 ± 0.07 |
| M_{HI} ^(k) | $(2.94 \pm 0.07) \times 10^{10} M_{\odot}$ |
| M_{H_2} ^(l) | $(2.52 \pm 0.12) \times 10^9 M_{\odot}$ |
| f_{mol} ^(m) | 0.079 ± 0.005 |

Notes - (a) J2000 coordinates of nucleus. (b) Systemic velocity of ring derived from HI kinematics (optical/heliocentric definition). (c) *IRAS* 12, 25, 60 and 100 μm point source flux densities (Moshir et al. 1990). (d) Integrated 8 – 1000 μm luminosity derived using *IRAS* data (Sanders & Mirabel 1996). (e) Integrated ^{12}CO line fluxes measured in this paper. Corrections for main-beam efficiency, beam-source coupling, and over sampling are described in Section 2.5. (f) The ring’s global I_{1-0}/I_{2-1} ratio. See footnote 8 in Section 2.5. (g) Integrated 20 cm radio continuum luminosity using the *robust* weighted data. (h) Integrated $\text{H}\alpha$ luminosity of the ring corrected for Galactic ($A_{\text{H}\alpha} = 0.33$; Corwin, Buta & de Vaucouleurs 1994) and internal extinction ($A_{\text{H}\alpha} = 0.92$) as described in Section 3.2.1. (i) SFR derived from extinction corrected $L_{\text{H}\alpha}$ after Kennicutt (1998a). (j) Global star formation efficiency (Section 3.5) following Young et al. (1996). We have corrected for Galactic extinction but not for helium mass. (k) Total HI mass using *robust* weighted ATCA data. No helium mass correction. (l) Total H_2 mass assuming X_{Gal} . No helium mass correction. (m) Global molecular mass fraction, defined $f_{\text{mol}} = M_{\text{H}_2}/(M_{\text{HI}} + M_{\text{H}_2})$.

Table 2: ATCA Observations

| | |
|---|---|
| Array configurations: | 6A,6B,6C,6D,1.5A,1.5B,750B,375 |
| Minimum/maximum baseline (m) | 30.6, 5972 |
| R.A. pointing center (J2000) | 06 ^h 43 ^m 06. ^s 66 |
| Dec. pointing center (J2000) | -74° 16′ 16″.0 |
| Integration time (hr) | 114 |
| Primary beam FWHM (arcmin) | 31.5 |
| Correlator configuration | full_8.512-128 |
| Center frequency (MHz) | 1390.0 |
| Number of channels | 44 |
| Channel separation (km s ⁻¹) | 27.3 |
| Primary flux calibrator | 1934-638 |
| Phase calibrator | 0454-801 |
| Bandpass calibrator | 0407-658 |
| Synthesized beam FWHM (arcsec) | 7.9 × 6.7 (<i>robust</i> weight) |
| Continuum bandwidth (MHz) | 128 |
| Channel map rms (mJy beam ⁻¹) | 0.48 (<i>robust</i> weight) |
| Continuum image rms (mJy beam ⁻¹) | 0.08 (<i>robust</i> weight) |

Table 3. Positions Observed with the SEST

| Position | P.A. ^(a) (deg) | R.A. (J2000) | Decl. (J2000) |
|----------|------------------------------|-----------------|------------------|
| P1 | 6 | 06:43:10.79 | -74:14:34.0 |
| P2 | 49 | 06:43:11.00 | -74:14:12.0 |
| P3 | 78 | 06:43:08.94 | -74:13:52.0 |
| P4 | 96 | 06:43:06.19 | -74:13:49.0 |
| P5 | 110 | 06:43:03.55 | -74:13:51.0 |
| P6 | 125 | 06:43:01.67 | -74:13:57.0 |
| P7 | 142 | 06:43:00.25 | -74:14:06.0 |
| P8 | 195 | 06:42:58.62 | -74:14:32.0 |
| P9 | 217 | 06:42:58.45 | -74:14:43.0 |
| P10 | 237 | 06:42:59.31 | -74:14:53.0 |
| P11 | 252 | 06:43:00.34 | -74:15:05.0 |
| P12 | 266 | 06:43:02.20 | -74:15:13.0 |
| P13 | 281 | 06:43:05.00 | -74:15:15.0 |
| P14 | 313 | 06:43:08.57 | -74:14:55.0 |
| Disk | ... | 06:43:04.54 | -74:14:33.0 |
| Nucleus | ... | 06:43:06.32 | -74:14:09.0 |

^aThe SEST beam’s position angle on the ring, measured clockwise in degrees from the western minor axis line of nodes, as illustrated in Figures 4 and 5.

Table 4. Results of the SEST Observations

| Pos. | $I_{1-0}^{(a)}$ (K km s ⁻¹) | Velocity ^(b) (km s ⁻¹) | Δv (km s ⁻¹) | $T_A^*(1-0)$ (mK) | σ_{1-0} (mK) | $I_{2-1}^{(a)}$ (K km s ⁻¹) | Velocity (km s ⁻¹) | $\Delta v^{(b)}$ (km s ⁻¹) | $\Delta v_{\text{cor}}^{(c)}$ (km s ⁻¹) | $T_A^*(2-1)$ (mK) | σ_{2-1} (mK) |
|---------|--|--|-------------------------------------|----------------------|------------------------|--|-----------------------------------|---|--|----------------------|------------------------|
| P1 | <0.22 | ... | ... | ... | 1.8 | <0.21 | ... | 242 (20) | 230 | ... | 0.8 |
| P2 | <0.11 | ... | ... | ... | 0.9 | <0.14 | ... | 140 (11) | 125 | ... | 0.8 |
| P3 | 0.91 (0.05) | 6949 (6) | 107 (3) | 8.3 | 0.9 | 0.48 (0.04) | 6941 (4) | 85 (8) | 130 | 5.3 | 0.8 |
| P4 | 1.57 (0.18) | 6814 (13) | 232 (24) | 9.3 | 1.6 | 1.25 (0.08) | 6903 (12) | 195 (21) | 175 | 7.3 | 0.7 |
| P5 | 1.71 (0.19) | 6887 (19) | 220 (37) | 7.7 | 1.4 | 1.01 (0.10) | 6869 (17) | 208 (18) | 183 | 5.2 | 0.9 |
| P6 | 1.10 (0.19) | 6887 (21) | 264 (40) | 6.6 | 1.8 | 0.74 (0.10) | 6827 (21) | 247 (49) | 213 | 2.9 | 0.9 |
| P7 | 2.02 (0.18) | 6686 (28) | 642 (40) | 4.2 | 1.5 | 1.68 (0.09) | 6771 (18) | 558 (31) | 542 | 4.2 | 0.7 |
| P8 | <0.17 | ... | ... | ... | 1.4 | <0.28 | ... | 193 (14) | 172 | ... | 1.2 |
| P9 | 0.88 (0.14) | 6472 (10) | 100 (21) | 7.3 | 1.2 | 1.20 (0.09) | 6512 (12) | 89 (10) | 89 | 9.6 | 0.9 |
| | | | | | | 0.41 (0.06) | 6201 (16) | 87 (16) | 87 | 4.4 | 0.9 |
| P10 | 1.00 (0.12) | 6445 (6) | 103 (12) | 8.4 | 1.3 | 0.48 (0.08) | 6439 (15) | 55 (11) | 55 | 5.5 | 1.1 |
| P11 | 0.79 (0.17) | 6433 (11) | 98 (22) | 7.8 | 2.8 | 0.93 (0.13) | 6411 (10) | 97 (12) | 66 | 9.6 | 1.5 |
| P12 | 0.70 (0.13) | 6459 (7) | 78 (15) | 8.5 | 1.8 | 1.04 (0.09) | 6525 (20) | 247 (40) | 230 | 6.2 | 1.0 |
| P13 | <0.25 | ... | ... | ... | 2.1 | <0.27 | ... | 240 (20) | 233 | ... | 1.0 |
| P14 | <0.25 | ... | ... | ... | 2.1 | <0.23 | ... | 420 (30) | 410 | ... | 0.8 |
| Disk | <0.25 | ... | ... | ... | 2.2 | <0.16 | ... | ... | ... | ... | 1.0 |
| Nucleus | <0.29 | ... | ... | ... | 2.4 | <0.14 | ... | ... | ... | ... | 0.9 |

^(a)Integrated CO line fluxes as defined in Section 2.2. The upper-limits are 3σ and assume $\Delta v_{\text{CO}} = \Delta v_{\text{HI}}$.

^(b)For ring positions with no CO detections (P1, P2, P8, P13, and P14) we list the corresponding HI linewidths (FWHM) in km s⁻¹.

^(c)inewidths after correcting for effects of rotation and expansion within the 22'' beam. The corrected widths are calculated with $\Delta v_{\text{cor}}^2 = \Delta v_{\text{CO}}^2 - \Delta v_{\text{rot}}^2 - \Delta v_{\text{exp}}^2$, as described in Section 3.4.3. Where ¹²CO($J = 2 - 1$) emission is not detected we list the corrected HI widths.

Table 5. Derived Mean Surface Densities, Masses, and Luminosities

| Position | $\Sigma_{\text{H}_2}^{(a)}$ ($\text{M}_{\odot} \text{ pc}^{-2}$) | $\Sigma_{\text{HI}}^{(b)}$ ($\text{M}_{\odot} \text{ pc}^{-2}$) | $\Sigma_{\text{H}\alpha}^{(c)}$ ($L_{\odot} \text{ pc}^{-2}$) | $\Sigma_{24\mu\text{m}}^{(d)}$ ($L_{\odot} \text{ pc}^{-2}$) | $A_{\text{H}\alpha}^{(e)}$ (mag) | $M_{\text{H}_2}^{(f)}$ ($10^8 M_{\odot}$) | $M_{\text{HI}}^{(f)}$ ($10^8 M_{\odot}$) | $L_{\text{H}\alpha}^{(g)}$ ($10^7 L_{\odot}$) | SFE ^(h) |
|----------|---|--|--|---|-------------------------------------|--|---|--|--------------------|
| P1 | <3.0 | 37.7 (3.2) | 0.33 (.01) | 11.5 (0.1) | 0.80 (0.14) | <1.2 | 15.2 (1.1) | 3.72 (.05) | >-0.91 |
| P2 | <2.0 | 21.6 (1.8) | 0.19 (.01) | 5.4 (0.1) | 0.98 (0.14) | <0.8 | 8.7 (0.8) | 2.54 (.04) | >-0.97 |
| P3 | 6.9 (0.6) | 13.4 (1.4) | 0.26 (.01) | 13.7 (0.1) | 1.03 (0.14) | 2.8 (0.3) | 5.4 (0.6) | 3.73 (.06) | -1.37 (0.08) |
| P4 | 18.0 (1.2) | 12.7 (2.8) | 0.23 (.01) | 5.7 (0.1) | 0.97 (0.14) | 7.3 (0.4) | 5.1 (0.8) | 3.06 (.05) | -1.84 (0.05) |
| P5 | 14.6 (1.5) | 13.0 (2.6) | 0.20 (.01) | 4.3 (0.1) | 0.92 (0.14) | 5.9 (0.6) | 5.2 (0.7) | 2.49 (.04) | -1.82 (0.09) |
| P6 | 10.7 (0.3) | 12.7 (0.8) | 0.15 (.01) | 3.6 (0.1) | 0.90 (0.14) | 4.3 (0.1) | 5.1 (0.3) | 1.98 (.04) | -1.78 (0.03) |
| P7 | 24.1 (1.3) | 14.4 (1.9) | 0.13 (.01) | 2.8 (0.1) | 0.86 (0.14) | 9.7 (0.6) | 5.8 (0.2) | 1.59 (.03) | -2.21 (0.04) |
| P8 | <4.0 | 34.5 (0.8) | 0.52 (.01) | 19.3 (0.1) | 0.83 (0.14) | <1.6 | 13.9 (0.5) | 6.06 (.06) | >-0.84 |
| P9 | 16.7 (1.2) | 65.6 (4.1) | 0.94 (.01) | 35.2 (0.2) | 0.84 (0.14) | 6.7 (0.5) | 26.3 (0.8) | 11.09 (.09) | -1.20 (0.04) |
| P10 | 5.0 (0.9) | 84.8 (5.9) | 0.83 (.01) | 36.3 (0.2) | 0.92 (0.14) | 2.0 (0.4) | 34.1 (1.3) | 10.62 (.09) | -0.72 (0.12) |
| P11 | 9.7 (1.4) | 89.9 (1.9) | 0.45 (.01) | 20.8 (0.2) | 0.96 (0.14) | 3.9 (0.6) | 35.6 (0.6) | 5.96 (.07) | -1.28 (0.11) |
| P12 | 10.8 (1.0) | 77.8 (3.1) | 0.30 (.01) | 11.6 (0.1) | 0.85 (0.14) | 4.4 (0.4) | 31.9 (1.1) | 3.56 (.05) | -1.51 (0.08) |
| P13 | <2.8 | 57.0 (2.1) | 0.16 (.01) | 6.8 (0.1) | 0.92 (0.14) | <1.2 | 22.9 (0.8) | 1.99 (.04) | >-1.23 |
| P14 | <2.4 | 25.2 (2.4) | 0.12 (.01) | 4.7 (0.1) | 0.84 (0.14) | <1.0 | 20.4 (0.8) | 1.49 (.03) | >-1.24 |
| Nucleus | <2.1 | <0.2 | 0.03 (.01) | 10.4 (0.1) | 2.17 (0.15) | <2.2 | <0.93 | 1.73 (.06) | ... |
| Disk | <1.8 | <0.1 | <0.02 | 3.5 (0.1) | 1.74 (0.14) | <2.0 | <0.52 | <0.78 | ... |

^aH₂ surface density, defined $\Sigma_{\text{H}_2} = M_{\text{H}_2}/\Delta\Omega_{\text{ring}}$. No helium correction applied.

^bHI surface density, defined $\Sigma_{\text{HI}} = M_{\text{HI}}/\Delta\Omega_{\text{ring}}$. No helium correction applied.

^cThe H α luminosity density derived by dividing $L_{\text{H}\alpha}$ by $\Delta\Omega_{\text{ring}}$. No extinction correction applied.

^dAverage 24 μm luminosity density, defined $\Sigma_{24\mu\text{m}} = \nu L_{\nu}(24\mu\text{m})/\Delta\Omega_{\text{ring}}$.

^eExtinction correction for the H α line calculated after Kennicutt et al. (2007). See discussion in Section 3.1.1.

^fTotal H₂ mass within each SEST beam using Equation (3) in Section 2.5. No helium correction applied.

^gIntegrated H α luminosity within each SEST beam after correcting for both internal and foreground extinction. See Section 3.2.1.

^hStar formation efficiency, defined $\text{SFE} = \log(L_{\text{H}\alpha}/M_{\text{H}_2})$ following Young et al. (1996), with $L_{\text{H}\alpha}$ and M_{H_2} in units of L_{\odot} and M_{\odot} respectively. See Section 3.5.

Table 6. Gravitational Stability in AM0644-74’s Ring

| Position | Σ_* ^(a) ($M_\odot \text{ pc}^{-2}$) | Σ_{gas} ^(b) ($M_\odot \text{ pc}^{-2}$) | Q_{gas} ^(c) | Q_* ^(d) | Q_{tot} ^(e) |
|----------|--|---|---------------------------------|----------------------|---------------------------------|
| P1 | 37.1 | 55.4 (4.4) | 2.9 (0.5) | 1.7– 4.3 | 1.1–1.7 |
| P2 | 29.7 | 32.1 (2.4) | 2.7 (0.5) | 2.2– 2.9 | 1.2–1.4 |
| P3 | 37.9 | 27.6 (2.1) | 3.3 (0.6) | 1.7– 2.4 | 1.1–1.4 |
| P4 | 32.6 | 41.8 (4.1) | 2.9 (0.6) | 2.0– 3.7 | 1.2–1.6 |
| P5 | 29.5 | 37.5 (4.1) | 3.4 (0.7) | 2.2– 4.3 | 1.3–1.9 |
| P6 | 23.5 | 31.8 (1.2) | 4.6 (0.8) | 2.8– 6.3 | 1.7–2.7 |
| P7 | 22.4 | 52.4 (3.1) | 7.1 (1.3) | 2.9–16.7 | 2.1–5.0 |
| P8 | 39.4 | 52.4 (1.1) | 2.4 (0.4) | 1.6– 3.1 | 1.0–1.3 |
| P9 | 49.6 | 111.93 (5.8) | 0.6 (0.1) | 1.1– 1.3 | 0.4 |
| P10 | 50.2 | 122.1 (8.1) | 0.3 (0.1) | 0.8– 1.3 | 0.3 |
| P11 | 45.6 | 135.5 (3.2) | 0.3 (0.1) | 1.0– 1.4 | 0.2–0.3 |
| P12 | 37.0 | 120.5 (4.4) | 1.3 (0.2) | 1.8– 4.3 | 0.8–1.0 |
| P13 | 29.7 | 81.3 (2.9) | 2.0 (0.3) | 2.2– 5.4 | 1.0–1.4 |
| P14 | 21.1 | 37.5 (3.3) | 7.5 (1.4) | 3.1–13.4 | 2.2–4.8 |

^(a)Stellar mass surface density estimated by multiplying the *I*-band luminosity density (L_I) by stellar $M_*/L_{I,\odot}$ derived by fitting the FUV-4.5 μm flux densities to Starburst99 SED. Uncertainties are $\approx 10\%$ (Section 3.3).

^(b)Gas surface density, $\Sigma_{\text{gas}} = (\Sigma_{\text{HI}} + \Sigma_{\text{H}_2})$. A helium mass correction is included.

^(c)Toomre Q parameter for HI+H₂. A correction for helium mass is included. Quoted uncertainties assume a flat rotation curve and Galactic X_{CO} .

^(d)Toomre Q parameter for the stellar ring. The two values correspond to different stellar velocity dispersions: $\sigma_* = \sigma_{\text{gas}}$ (larger) and $\sigma_* = d_{\text{ring}}/\tau_{\text{B5}}$ (smaller), where d_{ring} is the thickness of the H α ring and τ_{B5} is the main-sequence lifetime of a B5 star.

^(e)The combined stellar and gaseous Toomre Q_{tot} parameter, defined $Q_{\text{tot}} = \frac{\kappa}{\pi G} (\frac{\Sigma_{\text{gas}}}{\sigma_{\text{gas}}} + \frac{\Sigma_*}{\sigma_*})^{-1}$ (Wang & Silk 1994). The two values listed again correspond to $\sigma_* = \sigma_{\text{gas}}$ and $\sigma_* = d_{\text{ring}}/\tau_{\text{B5}}$, with formal uncertainties in the range 0.1 – 0.4.

Table 7. Derived Physical Conditions in AM0644-741’s ISM

| Position | $P_{\text{ISM}}/P_{\odot}^{(a)}$ | $\phi_{\text{mol}}^{(b)}$ | $f_{\text{mol}}^{(c)}$ | $\chi_{\text{UV}}/\chi_{\odot}^{(d)}$ | $\chi_{\text{FUV}}/\chi_{\odot}^{(e)}$ | $\Phi_{\text{UV}}^{(f)}$ | $n^{(g)}$ (cm^{-3}) |
|----------|----------------------------------|---------------------------|------------------------|---------------------------------------|--|--------------------------|-----------------------------------|
| P1 | 17.0– 26.8 | 47.9– 131.2 | <0.07 | 10.6 (0.5) | 1.16 (0.02) | 9.1 (0.6) | 20 |
| P2 | 6.6– 7.6 | 7.1– 9.8 | <0.09 | 8.9 (0.3) | 0.59 (0.02) | 15.1 (0.9) | 125 |
| P3 | 6.0– 7.3 | 5.1– 8.0 | 0.34 (0.05) | 10.0 (0.5) | 0.70 (0.02) | 14.3 (1.0) | 320 |
| P4 | 10.3– 14.2 | 17.2– 34.9 | 0.59 (0.08) | 9.8 (0.4) | 0.69 (0.03) | 14.2 (1.0) | 100 |
| P5 | 8.3– 11.8 | 12.5– 26.9 | 0.53 (0.10) | 8.5 (0.4) | 0.53 (0.01) | 16.0 (0.9) | 170 |
| P6 | 5.8– 9.0 | 6.1– 15.8 | 0.46 (0.02) | 7.9 (0.3) | 0.36 (0.02) | 21.9 (1.4) | 275 |
| P7 | 13.0– 31.5 | 34.3– 241.5 | 0.63 (0.06) | 8.2 (0.3) | 0.27 (0.02) | 30.4 (1.9) | 125 |
| P8 | 15.9– 22.1 | 25.2– 51.9 | <0.10 | 17.5 (0.5) | 0.42 (0.02) | 41.7 (1.8) | 175 |
| P9 | 59.9– 76.8 | 352.7– 608.1 | 0.20 (0.02) | 23.1 (0.5) | 0.69 (0.01) | 33.5 (1.0) | 2 |
| P10 | 69.1– 69.8 | 446.0– 455.3 | 0.06 (0.01) | 25.0 (0.5) | 0.89 (0.01) | 28.1 (0.8) | 1 |
| P11 | 75.2– 81.3 | 710.2– 843.2 | 0.10 (0.02) | 18.9 (0.4) | 0.81 (0.02) | 23.3 (0.9) | 2 |
| P12 | 62.9– 84.3 | 633.9–1206.7 | 0.12 (0.01) | 14.3 (0.5) | 0.76 (0.03) | 18.8 (1.1) | 5 |
| P13 | 29.9– 41.8 | 192.3– 400.3 | <0.05 | 9.2 (0.4) | 0.62 (0.02) | 14.8 (0.9) | 20 |
| P14 | 7.3– 16.1 | 11.3– 64.8 | <0.09 | 7.0 (0.4) | 0.67 (0.02) | 10.4 (0.8) | 30 |

^(a)ISM pressure from $P_{\text{ISM}} = (\pi G/2k_{\text{B}}) (\Sigma_{\text{gas}}^2 + \frac{\sigma_{\text{gas}}}{\sigma_*} \Sigma_{\text{gas}} \Sigma_*)$ expressed in units of the local ISM pressure ($P_{\odot} = 10^4 \text{ K cm}^{-3}$, Elmegreen 1993). The range of values follows from the uncertainty in the stellar velocity dispersion: $\sigma_* = d_{\text{ring}}/\tau_{\text{B5}} \approx 50 \text{ km s}^{-1}$ to $\sigma_* = \sigma_{\text{gas}}$.

^(b)Molecular fraction parameter, defined $\phi_{\text{mol}} = (P_{\text{ISM}}/P_{\odot})^{2.2}(\chi_{\text{UV}}/\chi_{\odot})^{-1}$ (Elmegreen 1993). The ISM is primarily molecular when $\phi_{\text{mol}} \gtrsim 1$.

^(c)The molecular gas fraction at each SEST beam position, defined $f_{\text{mol}} = M_{\text{H}_2}/(M_{\text{HI}} + M_{\text{H}_2})$.

^(d)UV radiation field intensity in the ring in units of the local value ($\chi_{\odot} = 2.0 \times 10^{-4} \text{ erg s}^{-1} \text{ cm}^{-2} \text{ sr}^{-1}$; Draine 1978), defined $\chi_{\text{UV}} = L_{\text{FIR}}/4\pi D_{\text{L}}^2 \Delta\Omega_{\text{ring}}(2.0 \times 10^{-4})$, L_{FIR} has been estimated by scaling the *IRAS* 40 – 500 μm luminosity by the fraction of the total *Spitzer* 70 μm emission contained in the 22'' beam. $\Delta\Omega_{\text{ring}}$ is the ring’s solid angle.

^(e)Normalized FUV radiation field intensity in the ring, defined $\chi_{\text{FUV}}/\chi_{\odot} = F_{\text{FUV}}/\Delta\Omega_{\text{ring}}(2.0 \times 10^{-4})$, with F_{FUV} derived from the *GALEX FUV* image.

^(f)Average cloud filling factor, defined $\Phi = \chi_{\text{UV}}/\chi_{\text{FUV}}$.

^(g)Total gas volume density ($n = n_{\text{HI}} + 2n_{\text{H}_2} \text{ cm}^{-3}$) inferred from PDF model of Allen et al. (2004).

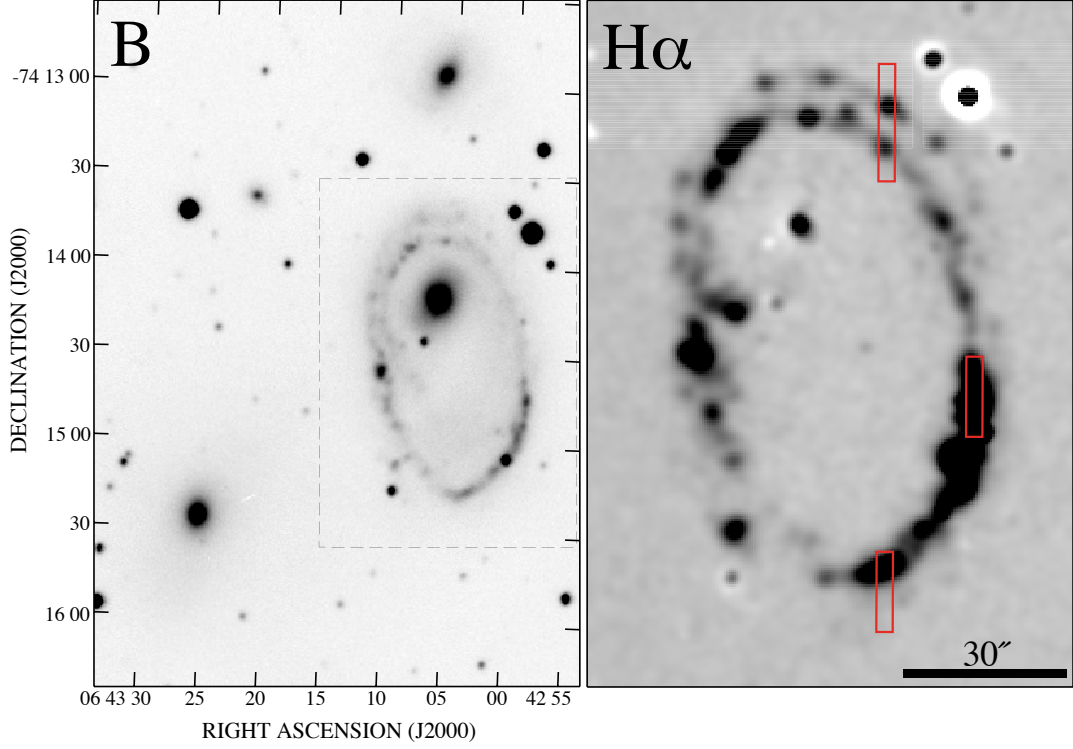


Fig. 1.— Left: optical B -band image of AM0644-741 and its two closest companion galaxies. Right: continuum subtracted $H\alpha$ image of the ring galaxy corresponding to the dashed region at left. A linear stretch is used in both. The rectangles (red in the online version) mark the slitlets used for the EFOSC2 spectra shown in Figure 3. Both images were obtained at CTIO. The star-forming complexes visible in the $H\alpha$ ring show a pronounced “beads on a string” morphology, which is indicative of large scale gravitational instabilities providing the triggering mechanism. The elliptical galaxy $1.8'$ to the southeast of the ring’s nucleus is the “intruder”. A faint stellar bridge connects it to the ring’s center (see Figure 1 in HW97).

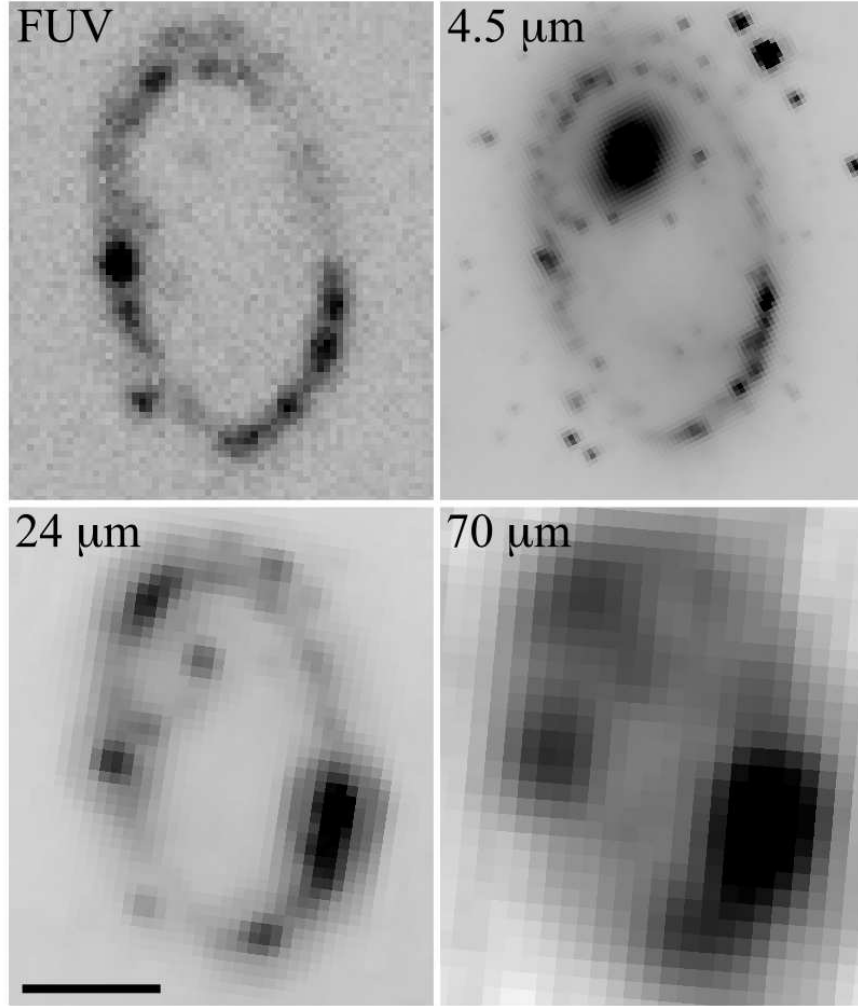


Fig. 2.— Emission from AM0644-741 spanning far-ultraviolet to far-infrared wavelengths. Upper left: FUV obtained with *GALEX* ($\lambda_{\text{eff}} = 0.153 \mu\text{m}$); upper right: $4.5 \mu\text{m}$ obtained with *IRAC*; lower left: $24 \mu\text{m}$ with *MIPS*; lower right: $70 \mu\text{m}$ with *MIPS*. All are shown using a logarithmic stretch. Emission in the FUV, $24 \mu\text{m}$ and $70 \mu\text{m}$ wavebands is dominated by the 42 kpc diameter ring, with only a negligible contribution from the nucleus and enclosed disk, in agreement with the $\text{H}\alpha$ image. Emission from evolved stars dominates the *IRAC* $4.5 \mu\text{m}$ image. A $30''$ scale bar is shown in the bottom left panel.

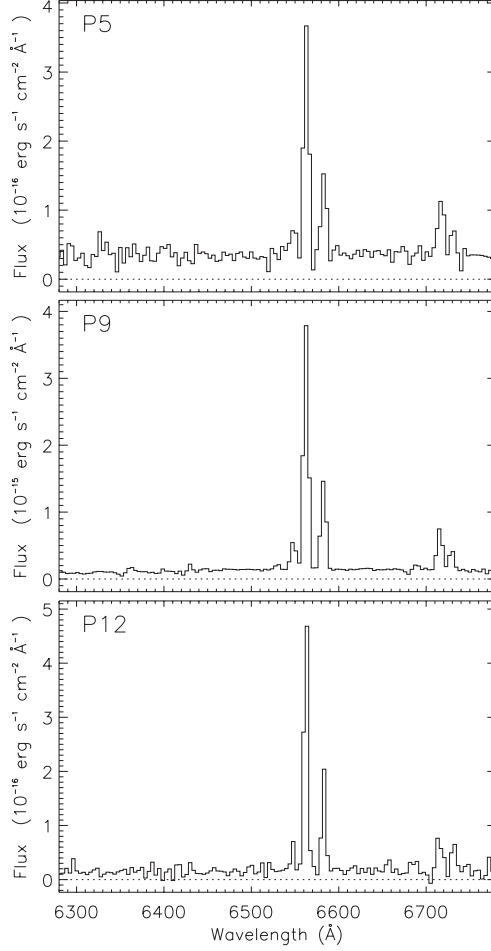


Fig. 3.— EFOSC2 red spectra for three HII complexes in AM0644-741’s ring. The slitlet positions are shown in Figure 1, and correspond closely to the centers of SEST positions P5, P9, and P12 in Figures 5 and 6. Emission lines of $H\alpha$, $[N\ II]\ \lambda\lambda 6548, 6584$, and $[S\ II]\ \lambda\lambda 6716, 6731$ are evident. The $F_{[NII]6584}/F_{H\alpha}$ and $F_{[N\ II]6584}/F_{[S\ II]6716+6731}$ emission line ratios yield $12+\log(O/H)\approx 9.1$ using the empirical calibration of Nagao et al. (2006), with no significant azimuthal variations. This is substantially in excess of solar metallicity ($12+\log(O/H)_{\odot} = 8.73 - 8.79$; Caffau & Ludwig 2008).

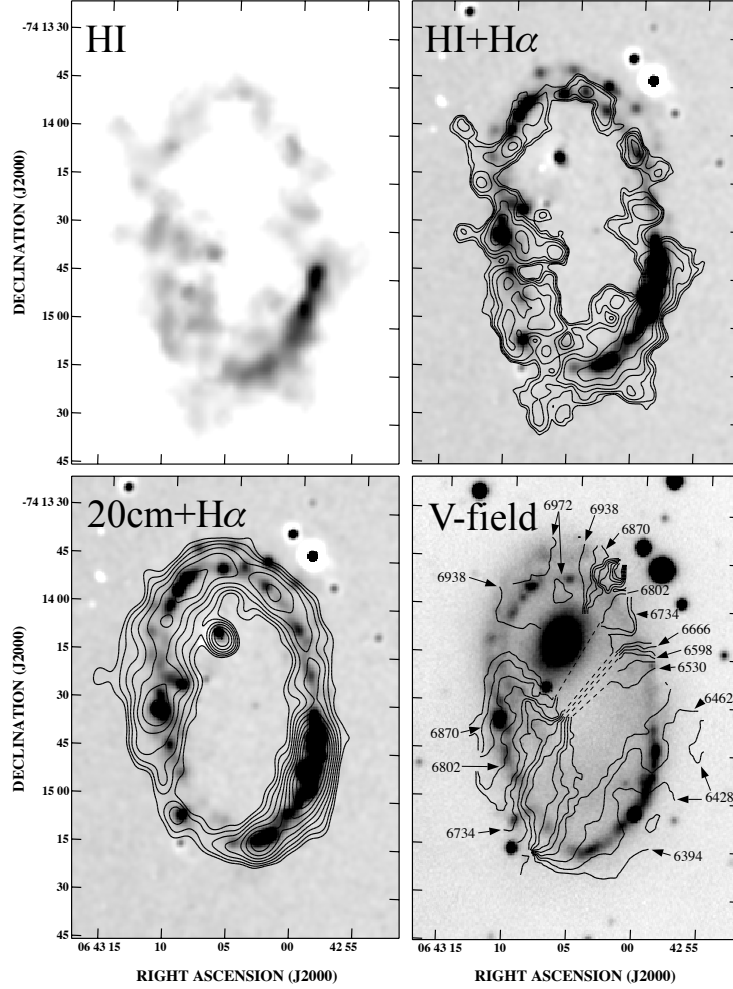


Fig. 4.— ATCA observations of AM0644-741. Upper left: *robust* weighted total HI distribution in gray scale with a linear stretch. The synthesized beam is $7.''9 \times 6.''7$ FWHM. Upper right: *robust* weighted HI surface density contours (Σ_{HI}) on the $\text{H}\alpha$ image. The logarithmic contours correspond to Σ_{HI} of 5.0, 7.7, 12.0, 18.6, 28.8, 44.6, 69.0, 103.0 $M_{\odot} \text{ pc}^{-2}$. Lower left: Contours of 20 cm radio continuum using *robust* weighting on the $\text{H}\alpha$ image. The contours correspond to flux densities of 0.11, 0.15, 0.20, 0.27, 0.36, 0.49, 0.66, 0.89, 1.20, 1.60 mJy beam^{-1} . Lower right: HI isovelocity contours (km s^{-1}) superposed on the B -band gray scale image.

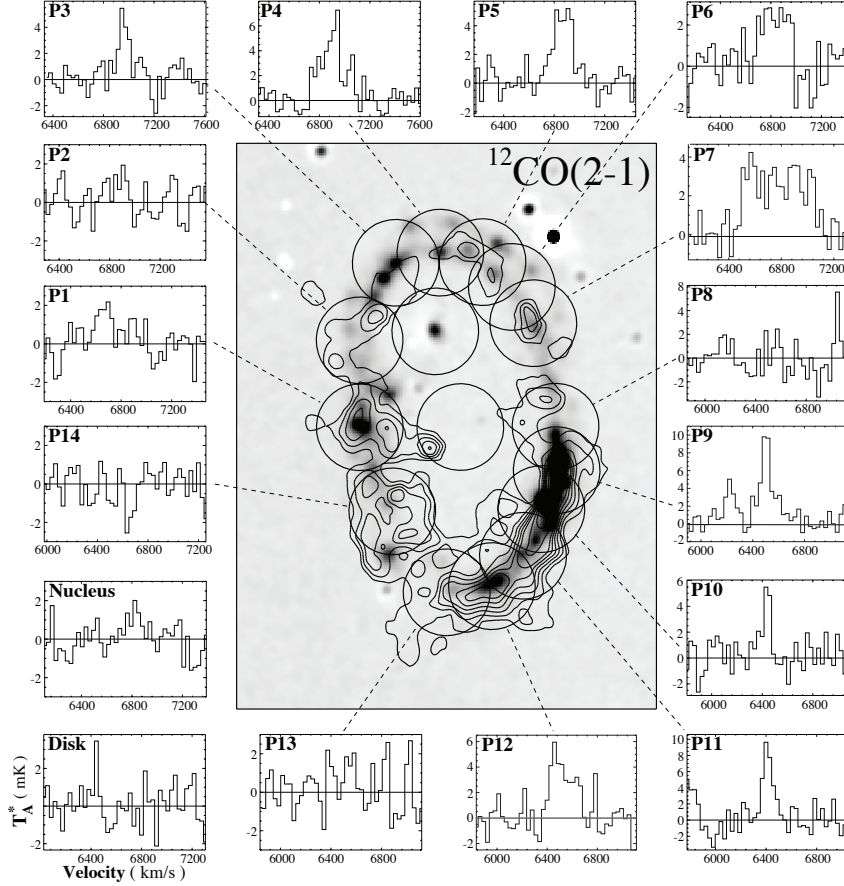


Fig. 5.— Individual $^{12}\text{CO}(J=2-1)$ spectra measured for AM0644-741’s ring, disk and nucleus. The circles represent the SEST 230 GHz beam ($22''$ FWHM) positions, and are shown superposed on a composite H α (gray scale) and HI (contours) image. Molecular gas is detected in two sections of the ring, the northern arc (P3-7) and the southwest quadrant (P9-12). A variety of profile shapes and widths are visible. No line emission is detected from the nucleus or encircled disk.

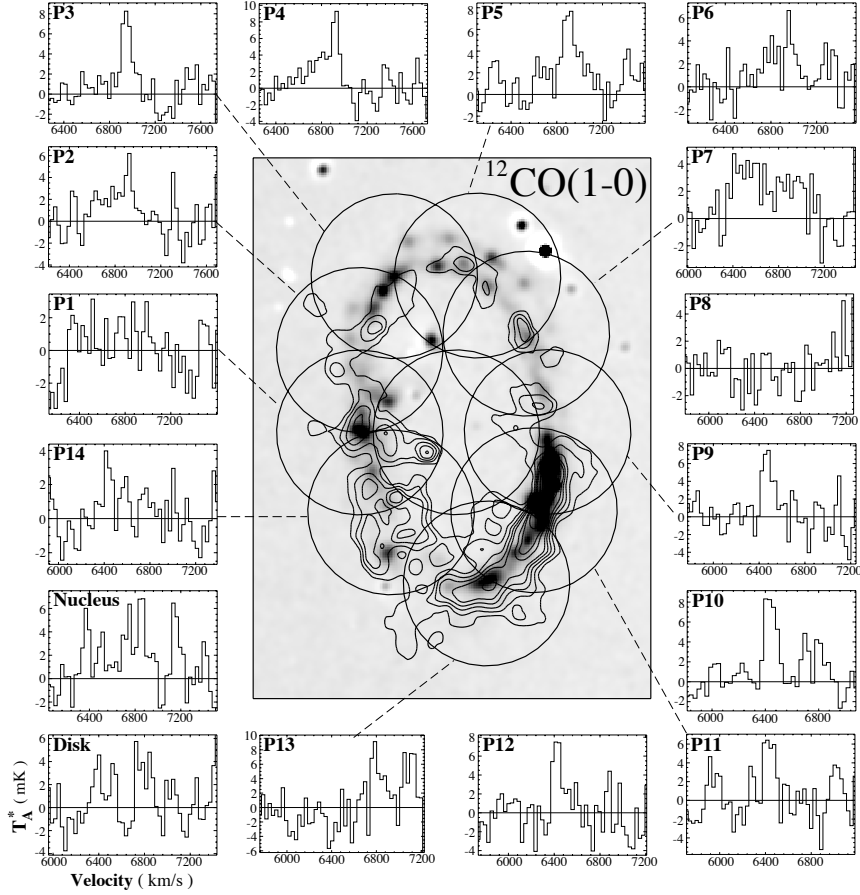


Fig. 6.— Individual $^{12}\text{CO}(J=1-0)$ spectra measured for AM0644-741’s ring, disk and nucleus. The circles represent alternating SEST 115 GHz beam ($44''$ FWHM) positions, and are shown superposed on a composite $\text{H}\alpha$ (gray scale) and HI (contours) image. Only 10 of the 16 observed positions are shown for clarity due to the large and overlapping beams. Note that $^{12}\text{CO}(J=1-0)$ and $^{12}\text{CO}(J=2-1)$ emission is detected at the same positions (P3-7 and P9-12) and show similar profiles, despite the very different beam widths.

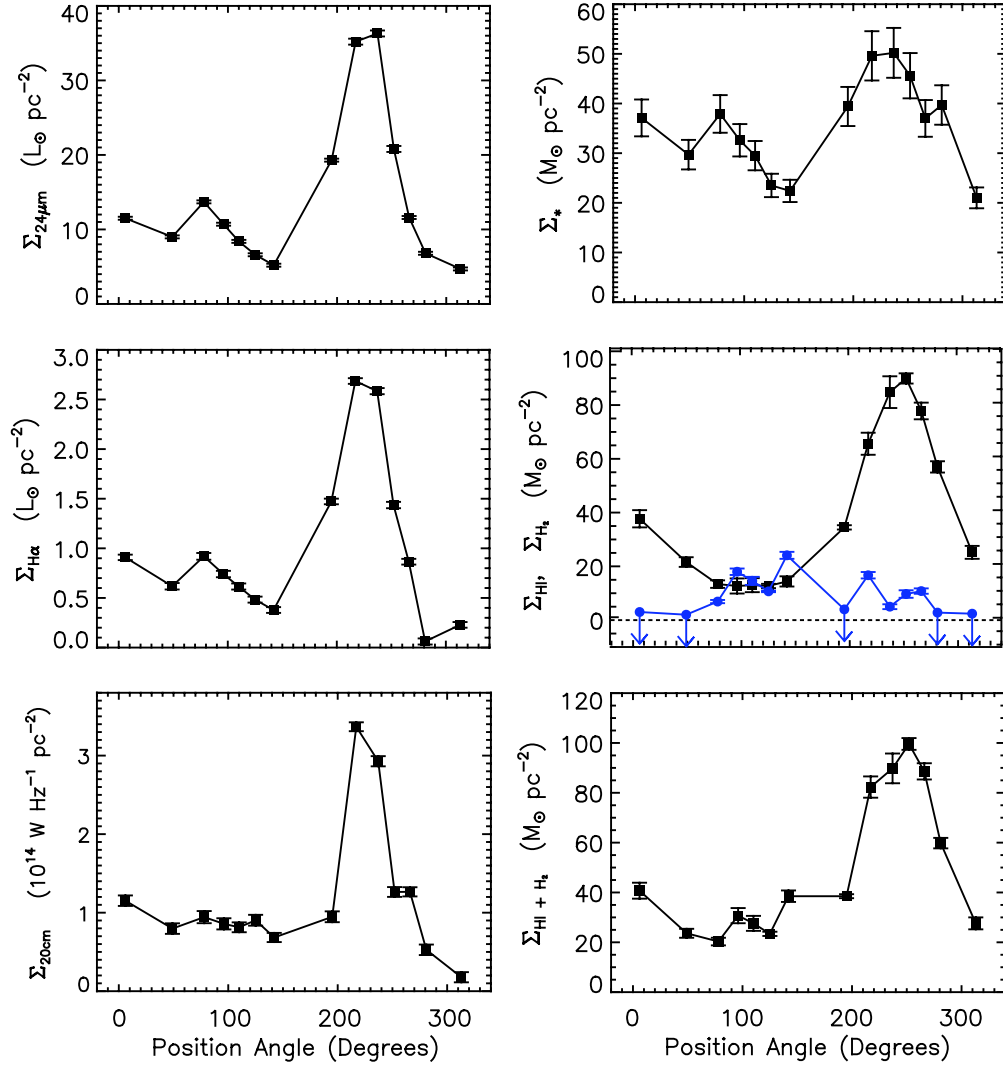


Fig. 7.— Azimuthal variations in emission around AM0644-741’s ring. The left column shows star formation indicators – upper left: warm dust as traced by MIPS at $24 \mu\text{m}$; middle left: massive stars as traced by $\text{H}\alpha$ line emission (corrected for internal and foreground extinction); bottom left: non-thermal radio continuum luminosity density as traced by ATCA 1.4 GHz interferometry. The right column shows the distribution of gas and stars – upper right: surface mass density of stars derived by fitting FUV-4.5 μm flux densities with Starburst99 SEDs; middle right: HI (black squares) and H_2 (blue circles) surface density plotted separately. No helium correction has been applied. Σ_{H_2} may be overestimated where two $\text{H}\alpha$ rings exist within the 230 GHz beam (i.e., P4-7); bottom right: the total HI and H_2 surface density. In each panel the positions run from P1 (far left) to P14 (far right).)

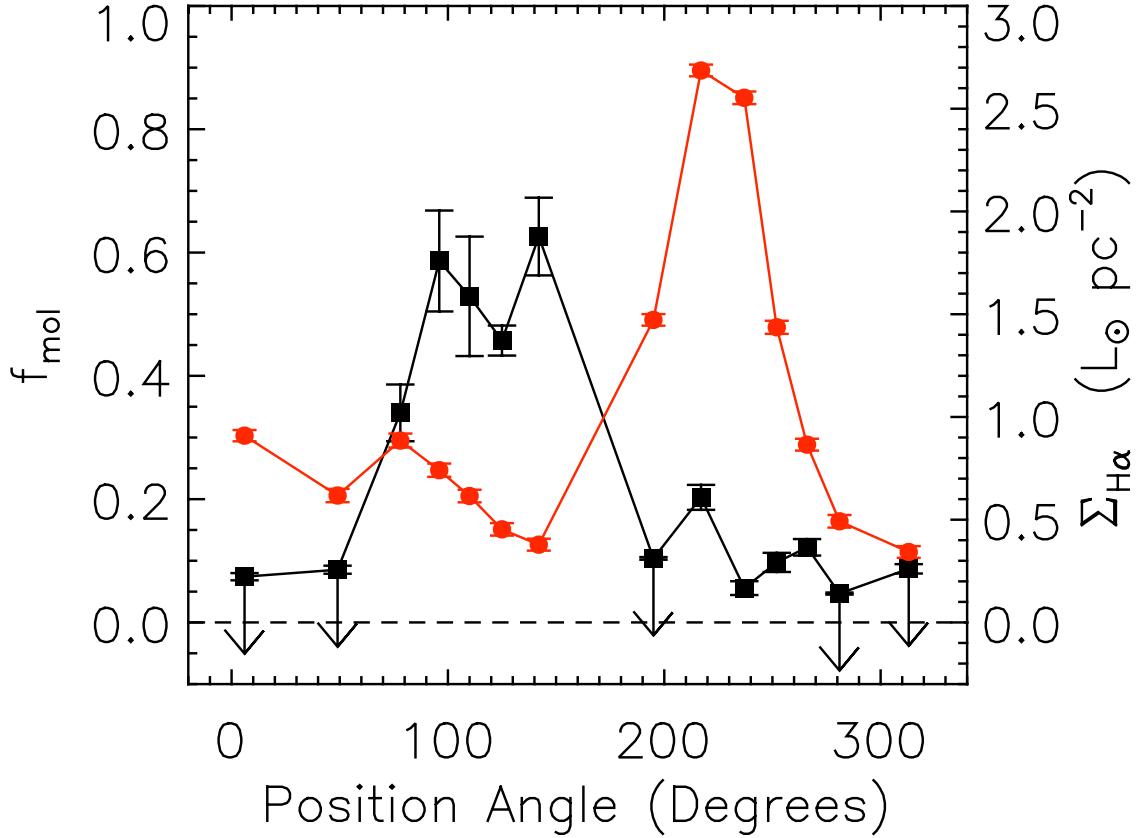


Fig. 8.— Azimuthal variations in the ring’s molecular fraction (black squares) and H α luminosity density (red circles). The molecular fraction (f_{mol}) is defined $f_{\text{mol}} = M_{\text{H}_2}/(M_{\text{HI}} + M_{\text{H}_2})$. The ring is poor in molecular gas ($f_{\text{mol}} \lesssim 0.2$) over $\approx 3/4$ of its circumference. Only in the northern quadrant is $f_{\text{mol}} \approx 0.5$. By comparison, $f_{\text{mol}} \gtrsim 0.75$ for M51’s inner ($r \leq 9$ kpc) spiral arms (Hidaka & Sofue 2002). The figure reveals a clear anti-correlation between massive star formation and the cold molecular component of the ISM. $\Sigma_{\text{H}\alpha}$ has been corrected for internal ($A_{\text{H}\alpha} \approx 1$) and foreground extinction. The data points run from P1 (far left) to P14 (far right).

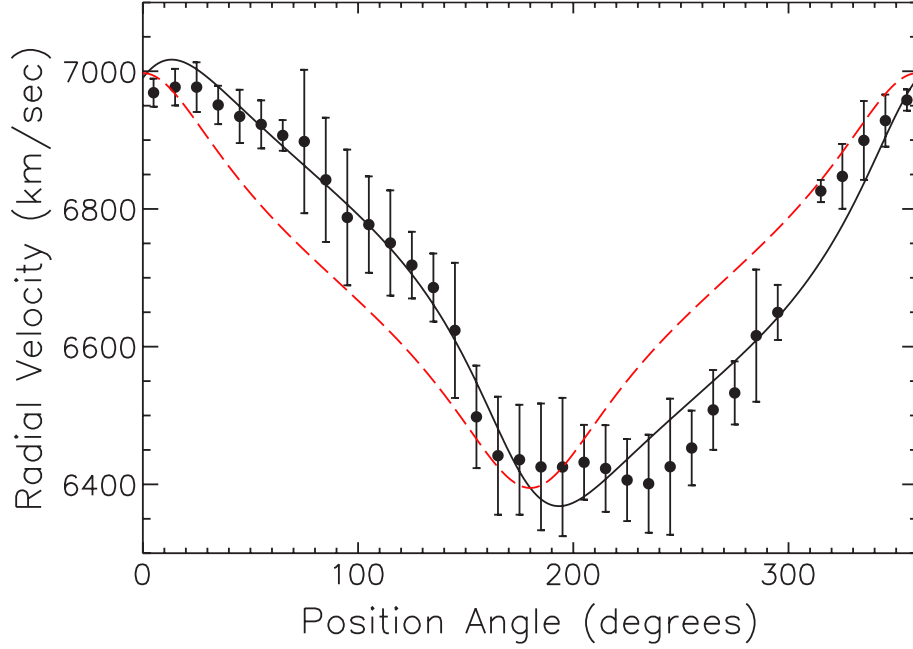


Fig. 9.— Radial velocity-position angle diagram for AM0644-741’s ring using the *robust* weighted HI data in Figure 4. The red dashed line shows the least-squares fit to the data for an inclined ($i = 56.5^\circ$) circular ring that is rotating but not expanding, while the solid line shows the fit when the ring is also allowed to expand. Error bars represent the velocity spread local to where v_{rad} is defined. The rotating/expanding ring model is a significantly better fit to the data, and we find $v_{\text{sys}} = 6692 \pm 8 \text{ km s}^{-1}$, $v_{\text{cir}} = 357 \pm 13 \text{ km s}^{-1}$, and $v_{\text{exp}} = 154 \pm 10 \text{ km s}^{-1}$, with the quoted errors representing formal uncertainties of the fit. Position angle is measured counterclockwise from the northern major-axis line of nodes.

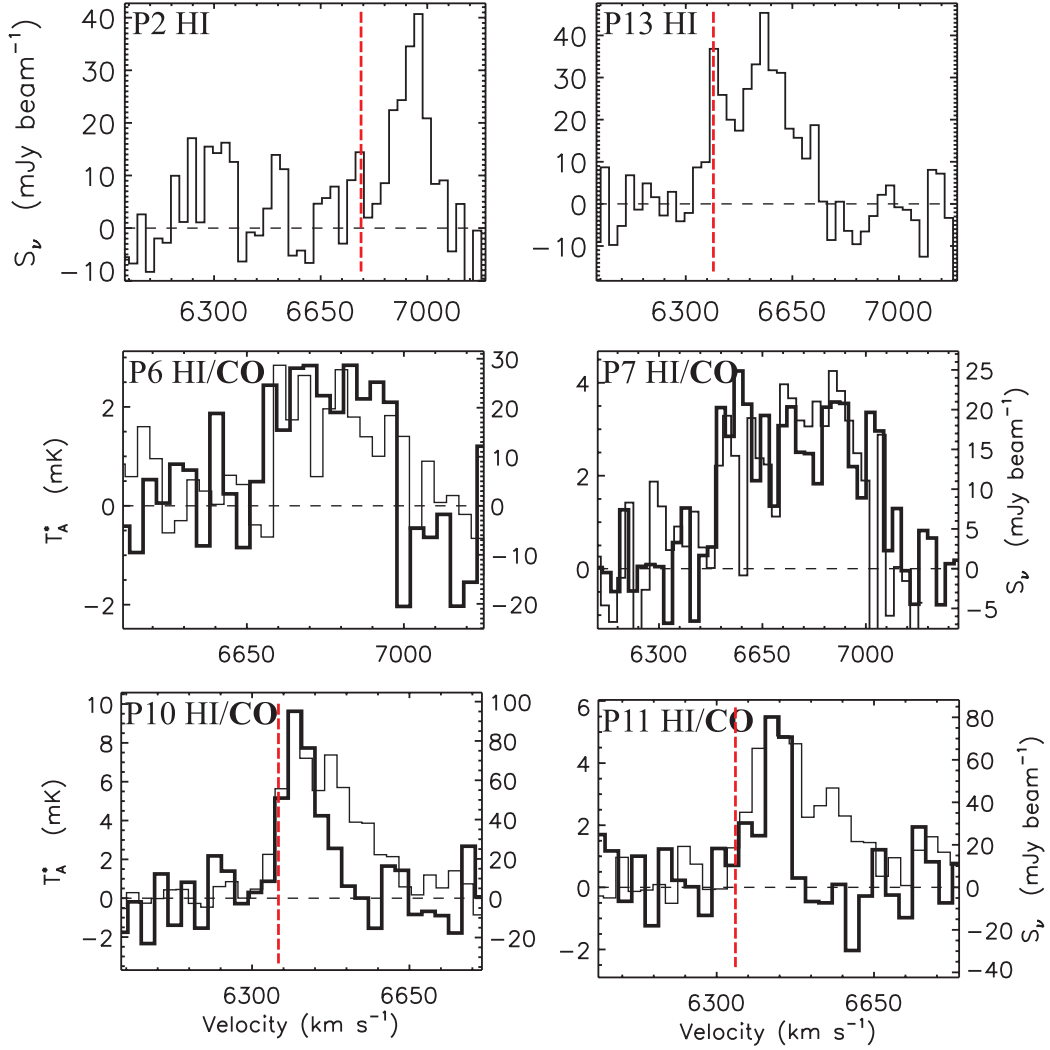


Fig. 10.— HI and $^{12}\text{CO}(J = 2 - 1)$ spectra extracted from identical $22''$ diameter regions in AM0644-741’s ring. Only HI is detected in the upper two panels (P2 & 13). Elsewhere, the CO profiles are shown using thicker lines. Multiple velocity components are sometimes seen in HI (e.g., P13), and both HI and CO lines can be very broad (P7). HI and CO peaks agree well, though HI sometimes shows a broad high-velocity wing not present in CO. The red vertical dashed lines mark the corresponding optical velocities determined by FMA. Where the HI and/or CO lines are sufficiently narrow and strong, the optical velocities are $\approx 60 - 90 \text{ km s}^{-1}$ smaller.

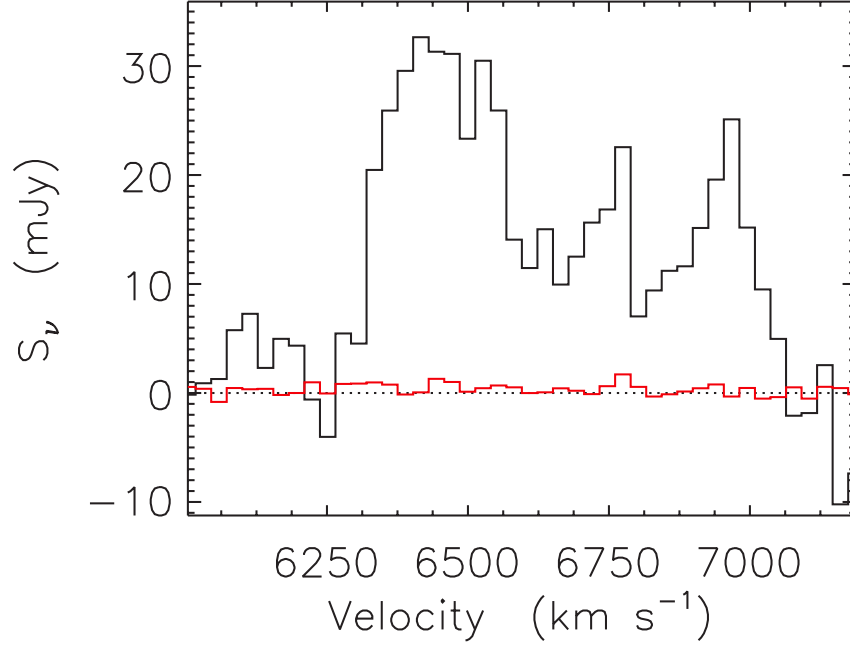


Fig. 11.— Total HI spectrum for AM0644-741 obtained by integrating the *robust* weighted map cube over the optical extent of the ring galaxy. An extremely wide profile ($\Delta v_{\text{FWZI}} = 743 \pm 28 \text{ km s}^{-1}$) with multiple peaks is evident. Also shown in red is the integrated HI spectrum from a 320 arcsec^{-2} (62 kpc^{-2}) region overlapping the gas poor nucleus and interior disk (i.e., the HI “hole” in Figure 4), giving an HI surface density upper limit of $1.9 M_{\odot} \text{ pc}^{-2}$ (3σ).

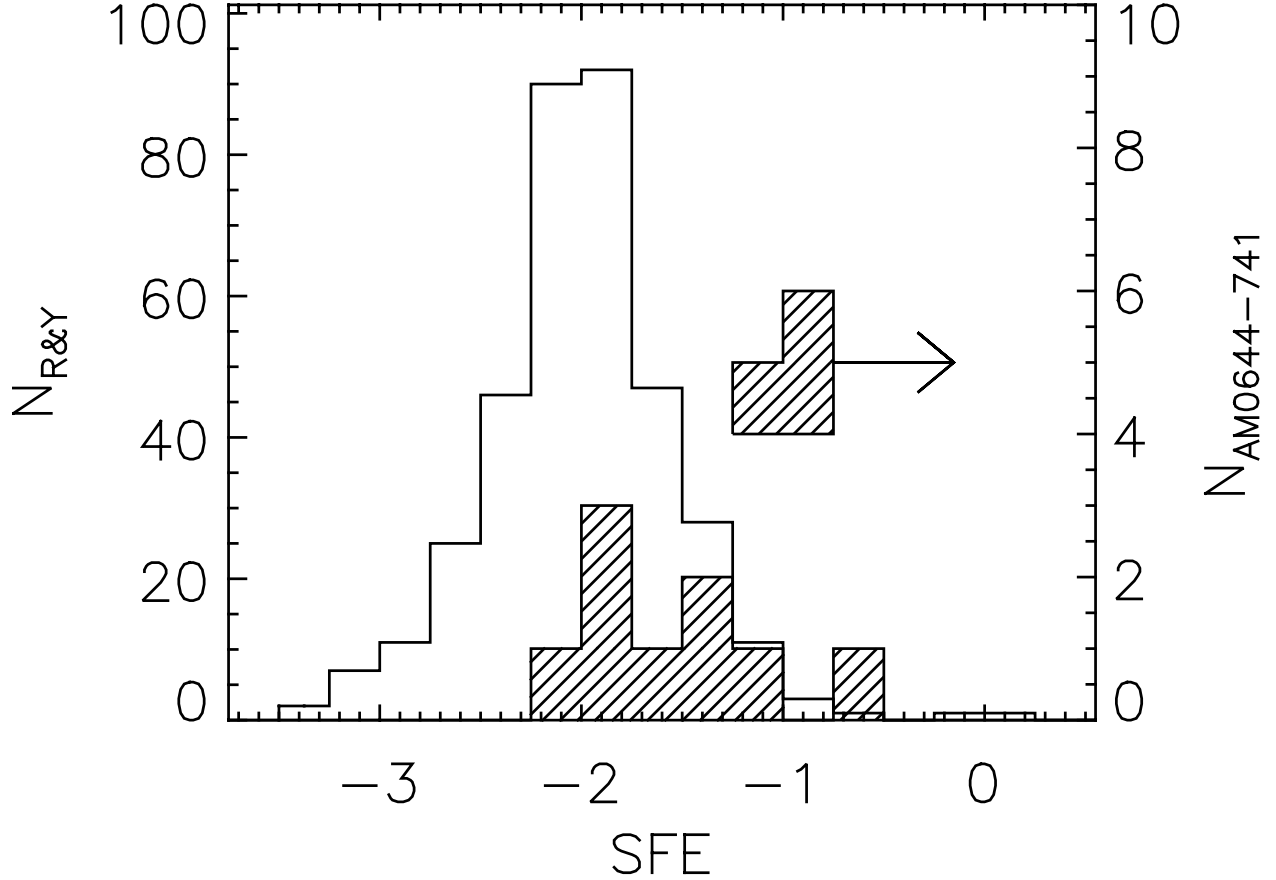


Fig. 12.— Star formation efficiencies, defined $SFE = \log(L_{H\alpha}/M_{H_2})$, in AM0644-741’s ring compared with spatially resolved regions within a sample of 122 normal and interacting disk galaxies from Rownd & Young (1999). The latter are represented by the unfilled histogram. For AM0644-741’s ring, SFE (and upper-limits) are shown using hatched histograms. $L_{H\alpha}$ and M_{H_2} are in solar units in the above equation. To be consistent with Rownd & Young we use their X_{CO} , correct $L_{H\alpha}$ for foreground extinction only, and do not correct M_{H_2} for helium. SFE in the ring appears somewhat elevated relative to the galaxies in Rownd & Young’s sample, though with an exceptionally wide (factor of 31) dispersion.

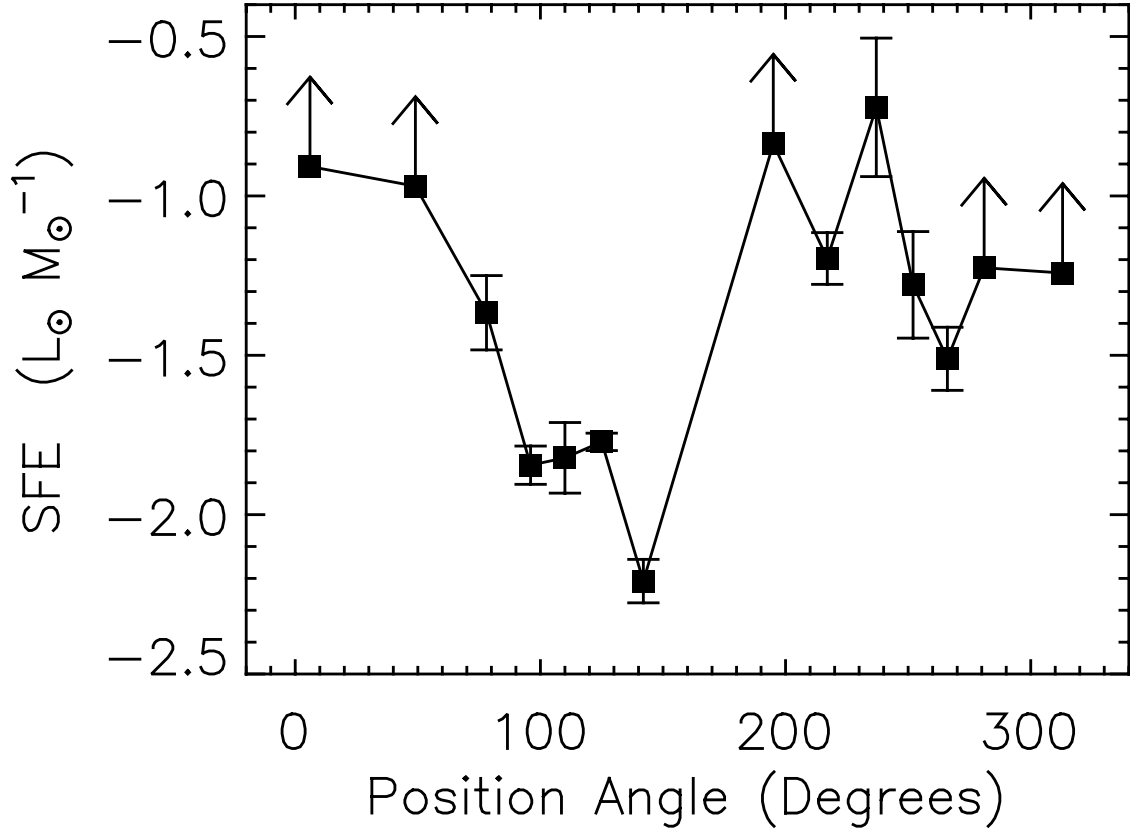


Fig. 13.— Variations in star formation efficiency around AM0644-741’s ring. SFE appears systematically higher in the starburst southwest quadrant relative to the northern quadrant. As in all the azimuthal plots, the plotted points run from P1 (far left) to P14 (far right).

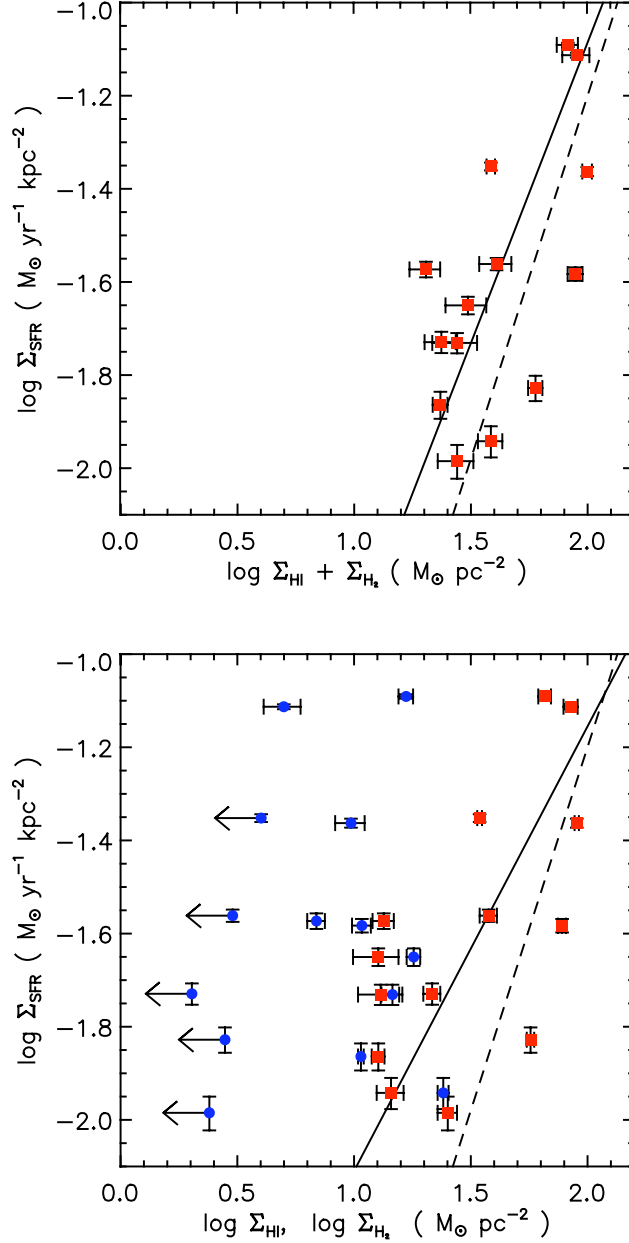


Fig. 14.— The star formation law in AM0644-741’s ring. Top: the correlation between SFR density and atomic plus molecular hydrogen surface densities is shown with red squares. The solid line shows a bivariate least-squares fit to the data for a Schmidt law expressed in power-law form: $\log \Sigma_{\text{SFR}} = (1.29 \pm 0.06) \log \Sigma_{\text{HI}+\text{H}_2} - (3.67 \pm 0.02)$, with a correlation coefficient $r = 0.63$. The dashed line shows the fit for the spatially resolved star-forming regions in the inner 14 kpc of M51a, $\log \Sigma_{\text{SFR}} = (1.56 \pm 0.04) \log \Sigma_{\text{HI}+\text{H}_2} - (4.32 \pm 0.09)$ (K07) for comparison. Bottom: the relation between SFR density and HI (red squares) and H₂ (blue circles) surface densities shown separately. Molecular hydrogen and SFR density are uncorrelated in AM0644-741’s ring (ignoring the limits, actually *anticorrelated*; $r = -0.48$), while Σ_{SFR} scales linearly with HI surface density: $\log \Sigma_{\text{SFR}} = (0.96 \pm 0.04) \log \Sigma_{\text{HI}} - (3.06 \pm 0.01)$, with $r = 0.63$. Σ_{SFR} has been corrected for extinction as described in Section 3.1.1. We have not included a helium contribution to enable direct comparisons with K07.

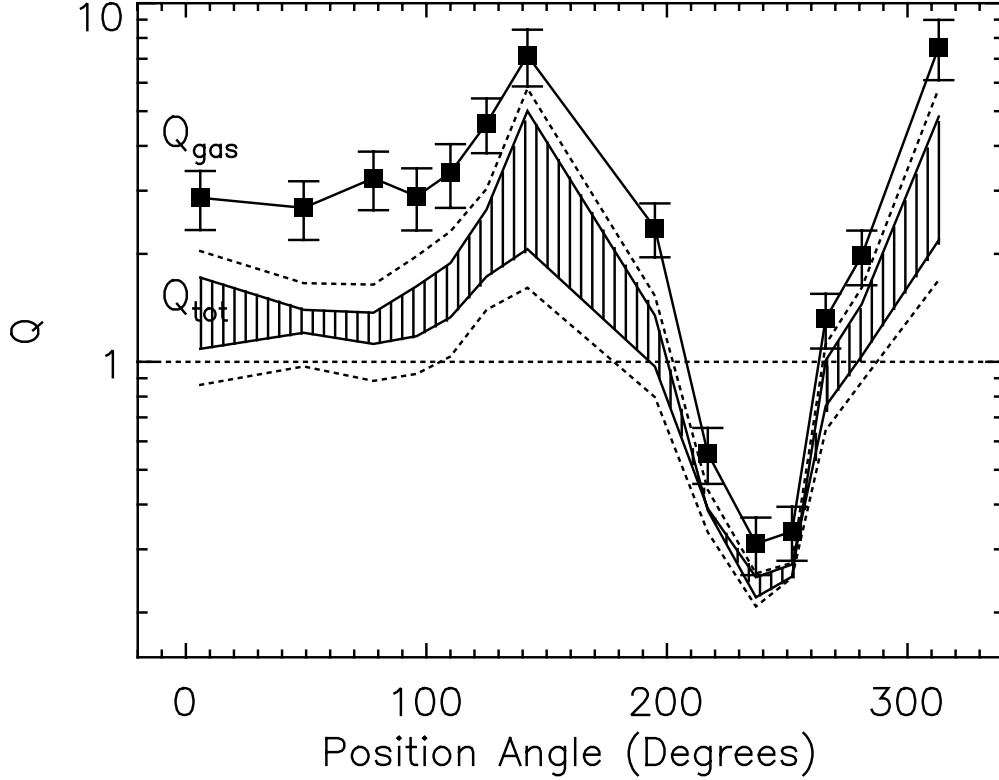


Fig. 15.— Toomre stability parameter Q for AM0644-741’s ring, starting at P1 (far left) and ending at P14 (far right). The ring will be susceptible to the growth of gravitational instabilities wherever $Q < 1$. The filled squares show the Q parameter for gas only (Q_{gas}) using both atomic and molecular components (including helium), and velocity dispersions derived from the line widths after correcting for rotation/expansion smearing within the $22''$ diameter beams. Only three ring positions (P9 - 11) possess $Q_{\text{gas}} \lesssim 1$. Elsewhere the gas ring is stable. The hatched region shows how the ring’s gravitational stability changes when the stellar component is included, using $Q_{\text{tot}} = \frac{\kappa}{\pi G} (\frac{\Sigma_{\text{gas}}}{\sigma_{\text{gas}}} + \frac{\Sigma_{*}}{\sigma_{*}})^{-1}$ (Wang & Silk 1994). Its width reflects the range of likely stellar velocity dispersions: $\sigma_{*} = \sigma_{\text{gas}}$ (upper-range) or $\sigma_{*} \lesssim d_{\text{ring}}/\tau_{\text{B5}} \approx 50 \text{ km s}^{-1}$ (lower-range) as implied by the narrow H α rings, where $\tau_{\text{B5}} = 40 \text{ Myr}$ is the main-sequence lifetime of a B5 star. The dotted lines represent the formal uncertainty in Q_{tot} . The ring remains largely *stable* ($Q_{\text{tot}} \approx 1.5 - 4$) after including stars except for P9-12 in the starburst southwest quadrant, where $Q_{\text{tot}} < 1$. Unless we are underestimating Σ_{H_2} (or overestimating σ_{*}), star formation in the ring is not primarily triggered by large-scale gravitational instabilities.

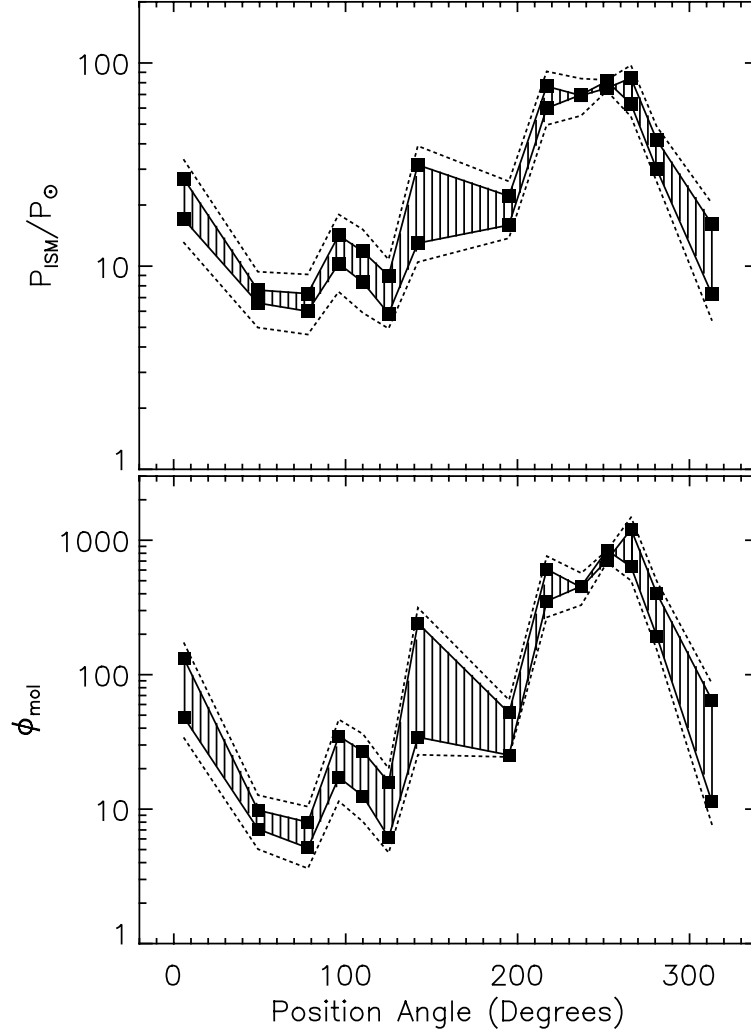


Fig. 16.— Top: azimuthal variations in the ISM pressure in AM0644-741’s ring, defined $P_{\text{ISM}} = \frac{\pi G}{2k_B} (\Sigma_{\text{gas}}^2 + \frac{\sigma_{\text{gas}}}{\sigma_*} \Sigma_{\text{gas}} \Sigma_*)$ (Elmegreen 1993), where we use measured Σ_* , Σ_{gas} , and σ_{gas} . The hatched region reflects the uncertainty in the stellar velocity dispersion, which we bracket with $\sigma_* = \sigma_{\text{gas}}$ and $\sigma_* \lesssim d_{\text{ring}}/\tau_{\text{B5}} \approx 50 \text{ km s}^{-1}$, the latter derived from the narrow width of the $\text{H}\alpha$ rings and the main-sequence lifetime of a B5 star. P_{ISM} is normalized by the local ISM pressure ($P_{\odot} = 10^4 \text{ K cm}^{-3}$). High P_{ISM} promotes the prompt conversion of HI to H_2 . The trends evident in this plot do not match the observed azimuthal variations of f_{mol} in Figure 8, indicating that the ISM pressure is not the dominant factor determining the ratio of atomic to molecular gas mass. Bottom: molecular fraction parameter $\phi_{\text{mol}} \equiv (P_{\text{ISM}}/P_{\odot})^{2.2} (\chi_{\text{UV}}/\chi_{\odot})^{-1}$ (Elmegreen 1993) for the same 14 positions. χ_{UV} is estimated using *IRAS* and *MIPS* $70 \mu\text{m}$ data as described in Section 4.1.2. The hatched region reflects the uncertainty in the stellar velocity dispersion. The ISM will be primarily molecular ($f_{\text{mol}} \approx 1$) wherever $\phi_{\text{mol}} \gtrsim 1$. This condition is satisfied everywhere in AM0644-741’s ring, leading to the expectation of a primarily molecular ISM, not the molecular poor ISM inferred from ^{12}CO measurements. The ring positions run from P1 (far left) to P14 (far right).

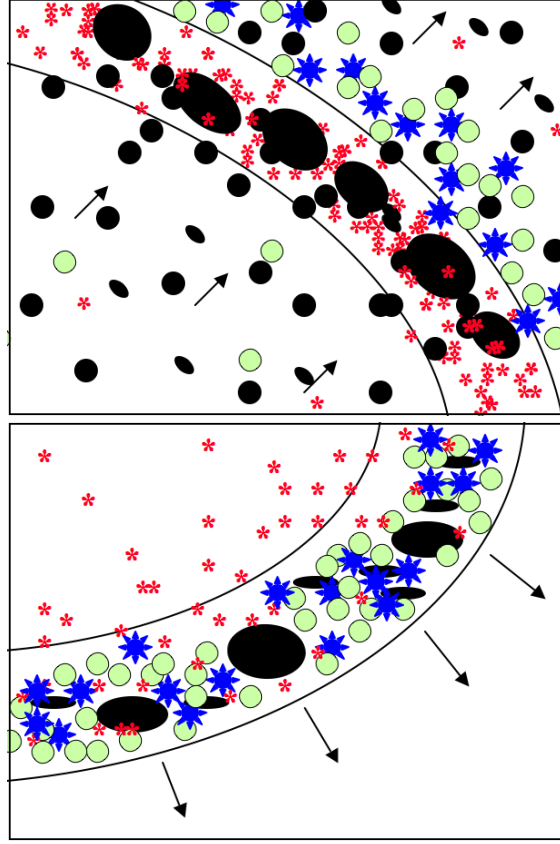


Fig. 17.— Schematic to illustrate differences between the conditions and evolution of the ISM for a grand design spiral arm as in M 51 (top) and the ring of a large and evolved ring galaxy such as AM0644-741 or the Cartwheel (bottom). In a spiral arm molecular (black) and atomic (green) clouds flow into the large-amplitude density wave, where giant molecular cloud complexes (GMCs) are formed and star formation initiated. The GMCs eventually flow out of the spiral density wave after $\tau \approx 15$ Myr but by now feel the effects of the embedded star formation, which results in young blue star clusters, HII complexes, and photodissociated HI being found downstream from the molecular dominated arm (e.g., Vogel et al. 1988). The escaping molecular cloud fragments will not experience such high ISM density, pressure, and FUV fields until an arm is again encountered ≈ 100 Myr later. By contrast, in an evolved and robustly star-forming ring galaxy the molecular clouds are confined to the expanding ring for > 100 Myr, where they are subjected to high FUV radiation fields for much longer periods. The result is a ring dominated by photodissociated HI and (on average) smaller molecular clouds, where CO will only be adequately shielded in the innermost cores (if at all), leading to H_2 being substantially underestimated by ^{12}CO emission even for solar abundances. $\Sigma_{\text{H}\alpha}$ would also be expected to correlate with atomic but not molecular gas, accounting for AM0644-741’s peculiar star formation law. (The arrows in the bottom panel represent the ring’s radial flow only).

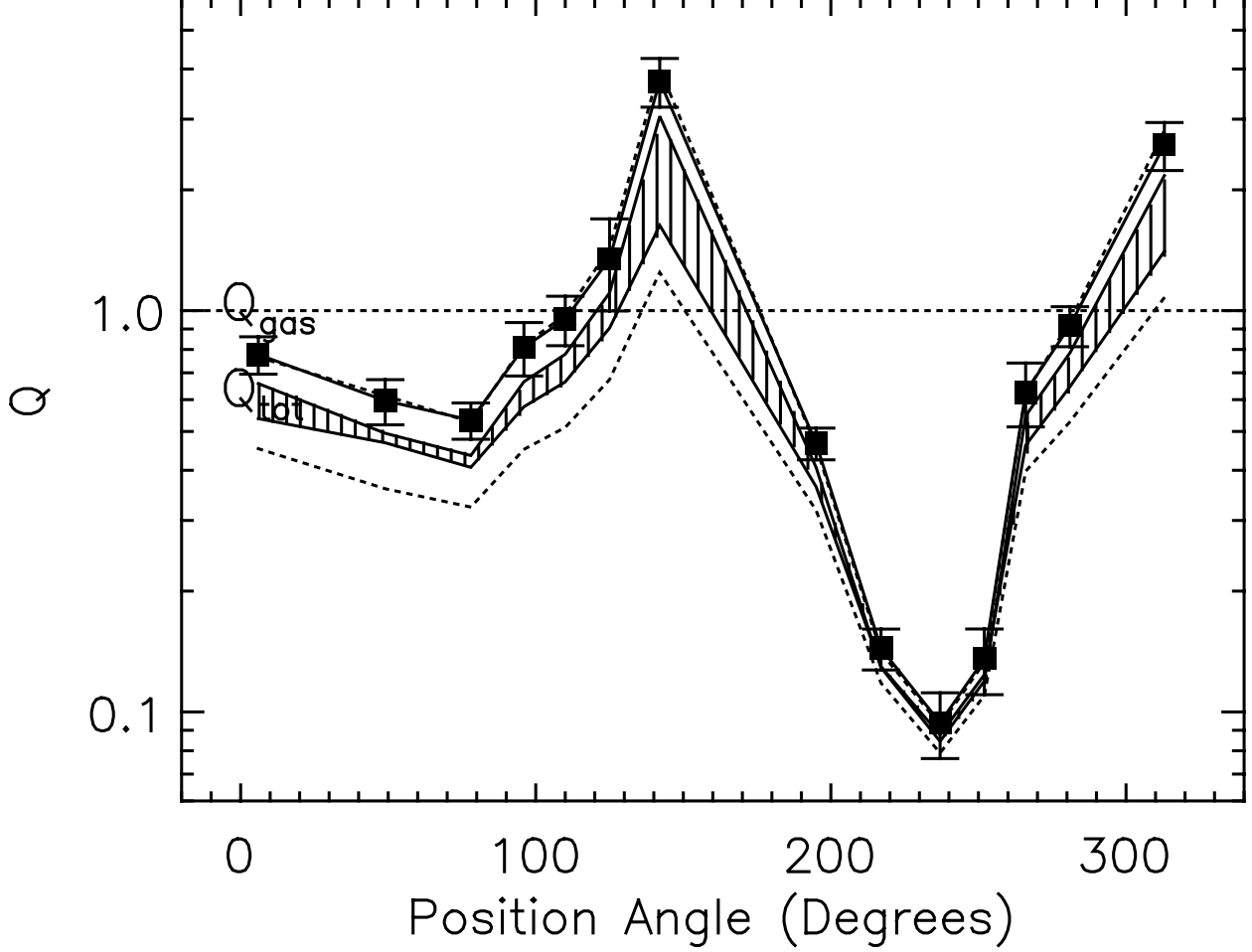


Fig. 18.— The resulting Toomre stability parameter for atomic plus molecular gas (Q_{gas}) and gas plus stars (Q_{tot}) in the ring of AM0644-741 after Σ_{H_2} is made to obey M51a’s molecular Schmidt law (i.e., $\Sigma_{\text{H}_2} = 1522 \Sigma_{\text{SFR}}^{0.73}$). As before, the plotted points run from P1 (far left) to P14 (far right). Compared to Figure 15, there is a much better agreement between Q_{tot} and the location of intense star formation, in particular P1, P3, and P8-12. The point of this exercise is to show that if a Schmidt law holds in AM0644-741’s ring, then large quantities of H_2 not traced by ^{12}CO sufficient to make large stretches gravitationally unstable likely exist.